Application of magnetic resonance imaging to the study of age related changes and gender differences in the human brain

Benjamin Crouch

November 28, 2018

Abstract

Magnetic Resonance Imaging (MRI) is an invaluable tool used in medical research and clinical practice. T1 weighted (T1w) and T2 weighted (T2w) magnetic resonance images are used to detect pathological changes in brain tissue such as demyelination and iron accumulation.

Voxel based statistical analysis (VBSA) is a technique used to identify brain regions that show evidence of abnormality in disease populations or individual patients. While VBSA is used extensively in the analysis of functional magnetic resonance imaging and voxel based morphometry images, its use in T1w and T2w image datasets has been much more limited. In this work, age related changes and gender differences in T1w and T2w images are examined in a dataset of 152 subjects taken from a publicly available dataset of healthy volunteers, demonstrating the utility of VBSA when applied to these mage types.

To investigate the most suitable intensity normalisation method, VBSA results were obtained with three different global intensity normalisation algorithms, the first algorithm was based on the whole brain mean, the second method was the voxel based iterative sensitivity (VBIS) method of (Abbott et al. 2009) and the third was based on the location of the intensity histogram peak. The latter two algorithms showed good agreement.

The most striking and statistically strongest result obtained is a strong negative correlation between T2w signal and age in the putamen, caudate head, para-hippocampal gyrus and amygdala, consistent with iron accumulation in these regions and most likely due to a higher rate of micro-bleeds occurring in these brain regions. Other results include decreased T1w signal and increased T2w signal in the thalamus with advancing age.

Results for Gender differences include a significantly higher T2w signal in the superior longitudinal fasciculus and internal capsule for females and a significantly higher T2w intensity in the medulla for males. T1w intensity was significantly higher in males in parts of the midbrain.

These results demonstrate that VBSA of T1w and T2w images is an effective tool for establishing physiologically meaningful localised patterns of change in cross-sectional neuro-image data-sets.

Signed Statement

I, Benjamin Crouch, certify that this work contains no material which has been accepted for the award of any other degree or diploma in any university or other tertiary institution and, to the best of my knowledge and belief, contains no material previously published or written by another person, except where due reference has been made in the text.

I give consent to this copy of my thesis, when deposited in the University Library, being made available for loan and photocopying, subject to the provisions of the Copyright Act 1968.

I also give permission for the digital version of my thesis to be made available on the web, via the University's digital research repository, the Library catalogue and also through web search engines, unless permission has been granted by the University to restrict access for a period of time.

SIGNED: ... . DATE: 29 November 2018 .....

Acknowledgements

This work would not have been possible without the assistance of my family, friends and colleagues. First and foremost, I would like to expressed my deepest appreciation and gratitude to my principal supervisor Dr Leighton Barnden for his guidance, support and mentorship and for giving me my start in medical physics. I am also grateful to Dr. Judith Pollard, Dr. Alex Santos, Kevin Hickson and Mohammad Mohammadi for their encouragement, advice and supervision, and for providing feedback on various versions of this manuscript. Thanks also to my diagnostic imaging physics colleagues: Dr. Daniel Badger, Chris Boyd, Peter Collins, Kevin Hickson, Dr. Yuri Matyagin, Dr. Donald McRobbie, Dr. Stewart Midgely and Dr. Victoria Sherwood for their support and encouragement and for their generosity in sharing their knowledge and expertise. Thanks also to Dr Wilson Vallat and Dr Richard Kwiatek for valuable discussions; I am also grateful to Dr Dylan Bartholomeusz, Rachael Dobson and all of the staff at the Royal Adelaide Hospital and Queen Elizabeth Hospital nuclear medicine departments for their support and for providing a stimulating friendly environment to work in. I would also like to thank Imperial College London for making the MRI data analysed in this thesis available to me. Special thanks to my parents Philip and Susan Crouch for their love and encouragement. Finally, I would like to thank the most important person in my life, my wife Natasha, for all her love, support and patience.

Contents

List of Abbreviations

ANCOVA	Analysis of covariance
ANTs	Advanced Normalisation Tools (software)
CC	Cross Correlation (image similarity measure)
DARTEL	Diffeomorphic Anatomical Registration Through Exponentiated Lie Algebra (software)
GLM	General Linear Model
GMV	Gray Matter Volume
L	Left
MI	Mutual Information (image similarity measure)
MNI	Montreal Neurological Institute (brain atlas)
MR	Magnetic Resonance
MRI	Magnetic Resonance Imaging
NMI	Normalised Mutual Information (image similarity measure)
R	Right
RF	Radio Frequency (electromagnetic radiation)
SPM	Statistical Parametric Mapping (software)
SSD	Sum of Square Differences
T1	longitudional relaxation time

T1w	T1 weighted (MR signal/image)
T2	transverse relaxation time
T2w	T2 weighted (MR signal/image)
TE	Echo time
TGMV	Total Gray Matter Volume
TIV	Total Intercranial Volume
TR	Repetition time
TWMV	Total White Matter Volume
VBIS	Voxel based Iterative Sensitivity Analysis (intensity normalisation algorithm)
VBM	Voxel Based Morphometry
VBSA	Voxel Based Statistical Analysis
WMV	White Matter Volume

Chapter 1

Introduction

1.1 Magnetic Resonance Imaging and Voxel Based Statistical Analysis

Since the discovery of the phenomena of nuclear magnetic resonance (NMR) in the 1930's, magnetic resonance imaging (MRI) has emerged to become an invaluable tool used extensively in clinical and research medicine. MRI has the ability to provide detailed high resolution images of the human body *in vivo* without exposing the patient to ionising radiation.

In MRI, the patient or sample is placed in a strong magnetic field which induces a small splitting between the energies of the nuclei depending on whether their spins are oriented parallel or anti-parallel with respect to the applied magnetic field. To acquire information about the sample, the nuclear spin ensemble is first excited by radio frequency electro-magnetic radiation into a higher energy non-equilibrium state. Following excitation, the sample magnetisation gradually returns to its equilibrium value through dissipative interactions between nuclei and surrounding molecules. This process is referred to as 'relaxation'. In general the transverse and longitudinal components of the magnetisation vector return to equilibrium at differing rates characterised by two independent time constants: the longitudinal relaxation time T1 and the transverse relaxation time T2. These two parameters provide complementary information about the cellular environment of the sample. By adjusting the timing and magnitude of the radio-frequency excitation pulses, one can produce images with contrast dominated by one of these two decay processes referred to as T1-weighted (T1w) and T2-weighted (T2w) images respectively. T1w and T2w images are especially useful for clinical imaging of the brain because they provide excellent contrast between gray and white matter brain tissue and are sensitive to a range of pathologies including demyelination, tumour and

infection.[1] T1w and T2w MR brain images are the main objects of study in this work.

1.2 Voxel Based Statistical Analysis

Voxel Based Statistical Analysis (VBSA)[2] is a framework for the systematic comparison of multi-dimensional brain images from different subjects for the purpose of identifying patterns of differences in various patient groups or between an individual and a normal reference dataset. It is used clinically in nuclear medicine to assist in diagnosis, but it's main use has been as a research tool in both nuclear medicine and MRI. When used in MRI research, VBSA has most commonly been applied to functional MR images and to gray and white matter probability maps derived from T1w images to analyse local volume changes (Voxel Based Morphometry (VBM)). Although both T1w and T2w images are widely used clinically, and T1w images are used to derive the gray and white matter morphometry images that are used for VBM, it is rare that the structural MRI images themselves are studied directly using VBSA techniques. One reason for this is that the interpretation of changes in T1w or T2w images can be much more subtle or ambiguous, with T1 and T2 changes attributable to a number of biological changes. Nevertheless, there is also a great deal of information contained in T1 weighted and T2 weighted magnetic resonance brain images which is amenable to VBSA methods and can provide further insight into the understand brain structure and function in disease and health. This work examines the utility of VBSA methods applied directly to images of T1w and T2w signal amplitude.

A complication in the application of VBSA methods to T1w and T2w images is the need to adjust for patient-to-patient variations in global signal intensity. MRI signal levels vary due to drift and subtle variations in the scanner environment that affect the global image intensities.[3] Therefore, in order to perform meaningful inter subject comparisons, it is necessary to adjust the overall signal intensity (Weiskopf et al. 2013). Similar adjustments are needed in nuclear medicine applications. A number of methods have been proposed for adjusting the global intensity of MR images including: whole brain mean Scaling, voxel based iterative sensitivity scaling (VBIS) (Abbott et al. 2009), intensity histogram based scaling

[1] There are also other more specialised brain MRI pulse sequences. Functional magnetic resonance imaging (fMRI) detects differences in transverse decay rate between oxygenated and de-oxygenated haemoglobin in order to pinpoint brain areas that are active during cognitive tasks. Diffusion weighted MRI is useful for examining the structure and integrity of white matter fiber tracts. T1w and T2w imaging. T1w and T2w images are sometimes referred to as structural MR images to distinguish them from functional MRI.

[2] The acronym VBSA is not standard terminology. It is introduced here as a variation on the well known acronym for voxel based morphometry (VBM). VBM is essentially VBSA applied to a specific class of images (modulated segmented tissue probability images) derived from MRI.

[3] Similar issues arise in the analysis of nuclear medicine images.

(Barnden et al. 2008), region of interest (ROI) based scaling to reference regions such as the eyeballs, temproalis muscles (Ganzetti et al. 2014) or whole brain.

The need for global intensity adjustment means that in VBSA of T1w and T2w images, only changes relative to the intensity in some reference region can be detected. If a more absolute measure of changes in MRI changes is required, one can perform what is sometimes referred to as voxel based relaxometry (VBR) (Pell et al. 2004) or quantitative MRI[4] (Tofts & Du Boulay 1990, Tofts 2005) which involves acquiring multiple images at different repetition times (TR) and or echo times (TE) respectively and performing exponential fits to estimate the T1 and T2 relaxation times (Callaghan et al. 2015, Weiskopf et al. 2013). The disadvantages of relaxometry are that the acquisition times are much longer so these types of scans are not done routinely, and they rely on the assumption that the relaxation curve is mono-exponential which is not necessarily valid for nonhomogeneous complex cellular environments. In (Abbott et al. 2009), VBSA of T2 relaxometry images was compared with VBSA of T2w images from the same cohort, and found good concordance.

This work is motivated by the previous collaboration (Barnden et al. 2011, Barnden et al. 2015, Barnden et al. 2016) of the author in which VBSA was used to detect correlations between brain MR signals and clinical variables in a population of 25 CFS patients.

The availability of much larger MRI datasets of normal volunteers presented an opportunity to use these techniques to better understand gender related differences and age related changes in healthy controls; as well as providing a testing ground to explore the concordance and validity of different algorithms for both spatial and intensity normalisation.

1.3 Problem Statement

In this work, voxel based statistical analysis is applied to T1w and T2w images for 152 healthy subjects taken from a public database. Using two separate intensity normalisation algorithms: the voxel based iterative sensitivity analysis of (Abbott et al. 2009) which is (a refinement of scaling to the whole brain mean) and normalisation to the histogram peak.

In doing so the following four research questions will be addressed.

1. Are age related changes in brain structure or function detectable by VBSA of T1w and/or T2w MR images?

2. Are there statistical differences between male and female cohorts that are detectable by VBSA of T1w and T2w MR images?

[4]Quantitative MRI (qMRI) includes a battery of other MR scans including magnetisation transfer and diffusion tensor image sequences in addition to T1 and T2 relaxometry images.

3. Are statistically significant differences (if found) attributable to morphometric differences or do they reflect more subtle microanatomical changes.

There are many different settings and parameters which affect VBSA results. The choice of voxel size, smoothing, masking and spatial normalisation algorithm are all important. Of crucial importance is the choice of intensity normalisation algorithm. In this work, three different intensity normalisation approaches are compared to address the following question:

4. How concordant are the results obtained from different intensity normalisation algorithms.

1.4 Thesis Outline

The remainder of this thesis can be divided into two parts. Chapters 2, 3, 4 and 5 are expository in nature and are designed to give background needed to understand the remaining chapters 6, 7, 8 and 9 in which original research is presented.

In Chapter 2 the physics background of MRI is briefly reviewed with a few more technical derivations in Appendix A. In Chapter 3 the micro-anatomy and topographical (or gross) anatomy of the brain are reviewed, and the effect of microanatomical and cellular composition of the brain on MR signal is discussed. In Chapter 4, the preprocessing steps that need to be applied to brain images to prepare them for statistical analysis are discussed. Chapter 5 discusses the application of statistics to images and the important issue of correcting for multiple voxel comparisons. At the end of Chapter 5, global intensity normalisation algorithms are discussed.

In Chapter 6, the details of analysis performed in this work is provided. The results of the voxel based statistical analysis are presented in Chapter 7. Chapter 8 discusses the likely physiological significance of the results, and relates them to other works. Possible future applications of VBSA to T1w and T2w brain images are discussed in light of the results obtained here.

Chapter 2

The Physics of Magnetic Resonance Imaging

2.1 Chapter Outline

This chapter provides background information on how the images studied in this work are generated. In Section 2.2, the basic setup of an MRI system is described. The phenomena of nuclear magnetic resonance is then briefly reviewed in the context of a single nuclear spin in a homogeneous magnetic field at finite temperature. The interaction of a nuclear spin with radio frequency (RF) electromagnetic radiation that allows the spins to be manipulated and their state detected is described in Subsection 2.2.5. Relaxation is the gradual return of the sample magnetisation to its equilibrium value following excitation by RF radiation. In Section 2.3, the interaction of the nuclear spins with their molecular environment is discussed. The role that the random motions of molecules have in determining longitudinal and transverse relaxation rates is covered. This is followed by a discussion on how RF pulse sequences can be used to probe MR relaxation behaviour. Section 2.4 briefly describes how signals coming from different locations in space are distinguished from one another using magnetic field gradients. In Section 2.5 the pulse sequences that are used to generate the T1w and T2w images studied in subsequent chapters are described.

2.2 Magnetic Resonance Imaging Physics

2.2.1 MRI apparatus

In MRI, patients are scanned in a very strong ambient magnetic field, denoted B_0. This main field is usually produced with the aid of a super-conducting magnet. The ambient

field strength of a modern clinical MRI is typically in the range 1.5 to 3 tesla which is in the order of 10^5 times greater than the strength of the earth's geomagnetic field. The MR imaging signal is carried by the spin degrees of freedom of atomic nuclei. These spin degrees of freedom can be manipulated and studied through their interaction with external RF transmitter and receiver coils.

MRI acquisition involves first exciting the nuclear spins by applying electromagnetic radiation with frequency close to the resonant (Larmor) frequency. The system then gradually returns ('relaxes') to its equilibrium configuration. The rate and manner in which the system relaxes depends on the composition of the tissue in its vicinity and can therefore provide useful diagnostic information.

In order to localise the signal to a particular point in space, the magnetic field is fine tuned using gradient magnetic fields. These magnetic field gradients are produced using conventional wire coils, such that the magnetic field varies slightly along a particular spatial axis.

2.2.2 Dynamics of Nuclear Spin Degrees of Freedom

The NMR signal is the result of the synchronised behaviour of many individual nuclei, their behaviour is most strongly influenced by the external RF. The interactions between nuclei and neighbouring nuclei is comparatively weak and to a good approximation, we can build up a picture of the aggregate behaviour by considering the statistical behaviour of a generic individual nuclear spin degree of freedom.

The interaction of a single spin half nucleus with its ambient magnetic field is dominated by the dipole interaction hamiltonian

$$H = \vec{M} \cdot \vec{B} = \hbar \gamma \, \vec{S} \cdot \vec{B}. \tag{2.1}$$

where B is the magnetic flux density, M is the magnetisation vector of the nucleus and γ is its gyromagnetic ratio and S is the nuclear spin operator represented by $\vec{S} = \frac{1}{2}\vec{\sigma}$, where σ^i are the Pauli matrices. The magnetic field

$$B(t) = B_0 + B_1(t) \tag{2.2}$$

can be decomposed into a static (time independent) background field B_0 and a time varying radio frequency magnetic field $B_1(t)$. There are small fluctuations in the field resulting from passing molecules are but these will be neglected until Section 2.3.

The two eigenstates of the hamiltonian have the z-component of nuclear spin aligned

parallel $|\uparrow\rangle$ or antiparallel $|\downarrow\rangle$ to the background magnetic field. The strong background magnetic field B_0 induces an energy splitting

$$\Delta E = \hbar\gamma|B_0| \tag{2.3}$$

between nuclear spin states that align parallel and antiparallel to the direction of the magnetic field and there is a characteristic frequency, the Larmor frequency

$$\nu_0 = \frac{\omega_0}{2\pi} := \frac{\gamma|B_0|}{2\pi}, \tag{2.4}$$

determined by this energy splitting. In most biomedical applications (including this work), the majority of the signal comes from hydrogen nuclei, most of which are contained in water molecules. The proton (hydrogen nucleus) has a gyromagnetic ratio γ_{p} equal to 2.675×10^8 rad $s^{-1}T^{-1}$. Alternatively, $\gamma_{\mathrm{p}}/2\pi = 42.57$ MHz T^{-1}.

2.2.3 The Density Matrix

To take into account thermal dissipative interactions, it is necessary to use the density matrix formalism, in which the spin state of a single nucleus is encoded in a two by two density matrix ρ in place of a two dimensional state vector ψ.

$$\rho = \frac{1}{2}\left(\mathbb{I} + \sum_{\mathbf{j=1}}^{\mathbf{3}} \rho_{\mathbf{j}}\sigma^{\mathbf{j}}\right) = \frac{1}{2}\begin{pmatrix} 1+\rho_3 & \rho_1 - i\rho_2 \\ \rho_1 + i\rho_2 & 1-\rho_3 \end{pmatrix} \tag{2.5}$$

Where $\mathbb{I}$ denotes the 2×2 identity matrix and σ^j are the Pauli matrices. The parameters ρ_i are constrained to lie within a three dimensional solid ball $\vec{\rho} \cdot \vec{\rho} \leq 1$. It's boundary is known as the Bloch sphere. When this inequality is saturated, the nucleus is in a pure state otherwise the state is mixed.

For a closed system, the evolution is unitary and the absolute value $|\rho|$ does not change with time. For dissipative systems such as nuclei under going relaxation, this need not be the case. Dissipative interactions are discussed in Section 2.3.

In the density matrix formalism, expectation values of an observable operator $\mathcal{O}$ are calculated via $\langle\mathcal{O}\rangle = \mathrm{Tr}[\mathcal{O}\rho]$. For example, the magnetisation vector can be calculated from the density matrix via

$$\langle\vec{M}\rangle = \mathrm{Tr}\left[\hbar\,\gamma\frac{\vec{\sigma}}{2}\rho\right]. \tag{2.6}$$

2.2.4 Equilibrium State

Taking into account the nonzero temperature of the human body and assuming thermal equilibrium, the system will be in the Boltzmann configuration

$$\rho_0(t;\beta) = \frac{\exp(-\beta H_0(t))}{\mathrm{Tr}[\exp(-\beta H_0(t))]}. \tag{2.7}$$

where $\beta = 1/kT$ is the Boltzmann factor. If we take B_0 to be in the z direction, so that H_0 is proportional to σ_3, we obtain

$$\rho_0 = \frac{1}{e^{-\beta E_1/2} + e^{-\beta E_2/2}} \begin{pmatrix} e^{-\beta E_1/2} & 0 \\ 0 & e^{-\beta E_2/2} \end{pmatrix} = \begin{pmatrix} \frac{1}{1+e^{-\beta(E_2-E_1)/2}} & 0 \\ 0 & \frac{1}{1+e^{+\beta(E_2-E_1)/2}} \end{pmatrix} \tag{2.8}$$

Identifying the occupancy numbers n_+ and n_- for the two energy states as the eigenvalues of the density matrix, and assuming a field strength of 3 tesla and a body temperature $T = 37°\mathrm{C} = 310°\mathrm{K}$, the population ratio between the two spin works out to be

$$\frac{n_+}{n_-} = \exp\left(-\beta(E_2 - E_1)/2\right) = 0.99999 \tag{2.9}$$

While this is only a very slight population difference, given that there are of order 10^{19} molecules in a cubic millimetre of water, the cumulative effect of this difference when summed over many nuclei give rise to effects which are measurable on a macroscopic scale.

The signal strength is proportional to the magnetisation which, by Eqs. 2.6 and 2.8, is proportional to the population difference which in turn is, to a very good approximation, inversely proportional to the temperature and directly proportional to the magnetic field strength:

$$\langle M_z \rangle_{\mathrm{eq}} = \frac{\hbar\gamma}{2}(n_+ - n_-) = \frac{\hbar\gamma}{2} n_- \left(\frac{n_+}{n_-} - 1\right) = -\frac{\hbar\gamma}{2}\frac{\beta(E_2 - E_1)}{2} + \mathcal{O}((\beta(E_2 - E_1))^2) \tag{2.10}$$

In humans, body temperature is tightly regulated and therefore reducing the temperature to improve the signal to noise ratio is not an option, however there is scope to improve the signal strength by increasing the magnetic field strength. Presently, 1.5 T and 3 T are the most common field strengths used in medical MRI systems, however there are research scanners that operate at 7-11 T . These higher magnetic fields bring with them additional technological challenges and heightened safety concerns, for example the higher gradients needed for theses systems induce peripheral nerve stimulation in some instances.

2.2.5 Excitation by Electro-Magnetic Radiation

In this section, the dynamics of the nuclei under the influence of an external radio frequency (RF) electromagnetic (EM) field are considered. RF radiation propagating parallel to the B_0 field induces an oscillating magnetic field

$$B_1(t) = |B_1| \left(\cos(\omega_{RF} t),\, \sin(\omega_{RF} t), 0\right) \tag{2.11}$$

Resonance is achieved when the RF frequency is tuned to the Larmor frequency ($\omega_{RF} = \omega_0$). In this case we obtain

$$\rho(t) = \frac{1}{2}\Big[\mathbb{I} + \cos(\omega_1 t)\sigma_3 + \sin(\omega_1 t)\big(\cos(\omega_0 t)\sigma_2 + \sin(\omega_0 t)\sigma_1\big)\Big]\rho_3(0). \tag{2.12}$$

Where t is the duration of the RF pulse. (This formula and its generalisation to $\omega_{\mathrm{RF}} \neq \omega_0$ is derived in detail in the appendix.) From Eq 2.12, it is evident that a pulse of RF radiation at frequency ω_0 with an amplitude ω_1 and duration τ rotates the magnetisation vector by an angle of $\theta = \omega_1 \tau$ radians away from the z axis. This angle is called the flip angle of the pulse. For simplicity, in the above we have assumed a rectangular pulse shape, which is switched on and off instantaneously. In practice other pulse shapes may be used to produce the same effect.[5]

2.2.6 Emission of EM radiation and signal detection

Having discussed the effect of electro-magnetic radiation on the magnetisation vector, it should also be noted that there is an equally important reciprocal effect whereby the rotation of the magnetisation vector about the z axis induces fluctuations in the surrounding electro magnetic field which propagates as electromagnetic radiation with frequency centered on the larmor frequency. This frequency falls in the radio frequency region of the electromagnetic spectrum and is detectable by receiver coils, enabling the transverse magnetisation to be measured. The received signal is proportional to the transverse magnetisation of the sample. In order to obtain measurements that depend on the longitudinal magnetization, RF pulses which mix the transverse and longitudinal components are needed.

[5] Usually a sinc pulse shape is preferred because it is the fourier transform of a rectangular pulse in object space, which in the presence of a magnetic field gradient allows for the excitation of a two dimensional slice of prescribed thickness.

2.3 Relaxation

2.3.1 Relaxation Phenomena

After nuclear spins are excited into a higher energy state by RF radiation, they gradually return to their equilibrium configuration through interactions with surrounding electrons and molecules. This process is called relaxation. Relaxation rates are influenced by the composition and properties of the surrounding tissue in which the nucleus resides and are thus able to provide structural information.

When dissipative interactions with surrounding molecules are included, the evolution of the system need not and in general will not be unitary. In this case, the evolution is governed by a more general 'master equation' of the form

$$\frac{d\rho}{dt} = \frac{1}{i\hbar}[\rho, H] + R(\rho; t). \tag{2.13}$$

In general, the relaxation term $R(\rho)$ depends not just on the state of the system at time t but also on its state at earlier times.

Under simplifying assumptions, the relaxation term reduces (Goldman 2001) to the form

$$R(\rho, t) = \sum_{ij} \mathfrak{R}_{ij}(\rho^i(t) - \rho^i_{\text{eq}})\sigma^j \tag{2.14}$$

Due to symmetry constraints, the relaxation matrix $\mathfrak{R}$ contains only two independent components. For B aligned along the z axis, $\mathfrak{R}$ takes the form

$$\mathfrak{R} = \begin{pmatrix} R_2 & 0 & 0 \\ 0 & R_2 & 0 \\ 0 & 0 & R_1 \end{pmatrix} \tag{2.15}$$

The relaxation coefficients R_i are related to the strength of the coupling between the nuclei and surrounding molecules and to the statistical properties of the medium.[6] The reciprocals of R_1 and R_2 define the relaxation times $T_1 = R_1^{-1}$ and $T_2 = R_2^{-1}$. As will be shown in Subsection 2.3.2, longitudinal relaxation time T_1 determines the rate at which the longitudinal magnetisation returns to it's equilibrium value, while the transverse relaxation time T_2 determines the decay rate of the transverse component of the magnetisation. In body tissue, T_1 is usually an order of magnitude longer than T_2.

[6] Note that due to an unfortunate clash of notation conventions, $R_1 = \mathfrak{R}_{33}$ and $R_2 = \mathfrak{R}_{11} = \mathfrak{R}_{22}$.

2.3.2 Bloch Equations

Eqs. 2.13, 2.14 and 2.15 can be combined to obtain the Bloch equations

$$\frac{dM_i}{dt} = \gamma \sum_{j,k} \varepsilon_{ijk} M^j B^k - \sum_i \mathfrak{R}_{ii}(M_i - M_i^{\text{eq}})\sigma^i. \tag{2.16}$$

which describe the time evolution of the magnetisation vector (See the appendix for details). For a constant magnetic field oriented in the z direction, the general solution to the Bloch equations is

$$M_x(t) = M_\perp(0)\exp(-R_2 t)\cos(\omega_0 t + \theta) \tag{2.17}$$

$$M_y(t) = M_\perp(0)\exp(-R_2 t)\sin(\omega_0 t + \theta) \tag{2.18}$$

$$M_z(t) = (M_z(0) - M_z^{\text{eq}})\exp(-R_1 t) + M_z^{\text{eq}} \tag{2.19}$$

where θ, $M_z(0)$ and $M_\perp(0)$ are determined by the initial state of the system.

The Bloch equations can be expected to hold for a homogeneous sample, however if the sample is heterogeneous and there is mixing between different components on a time scale similar to the relaxation times then more general multi-exponential behaviour is to be expected. For example, water molecules near a membrane behave differently to water that is distant from membranes and there is interaction between these compartments through diffusion.

2.3.3 Calculation of relaxation rates

In a fluid environment, nuclei experience a randomly fluctuating background dipole field $f(t)$, due to the influence of passing molecules which randomly tumble and collide around them. The statistical distribution of these fluctuations is encoded in the rotational correlation function[7]

$$C(t) = \langle f(0)f(t)\rangle, \tag{2.20}$$

[7]For water, there is also a translational correlation time related to the time between molecular collisions and measured by the correlation function for the molecular velocity vector. The translational motion can be probed with diffusion mri pulse sequences. A third timescale also exists as due to proton exchange processes, the water molecules themselves having a finite life time (of order milliseconds) . The rotational correlation time is the shortest timescale, and dominates the interactions between the molecular degrees of freedom and the magnetic moment of hydrogen nuclei.

or alternatively by it's (one sided) fourier transform, the spectral function

$$\mathcal{J}(w) = \int_0^\infty C(t)e^{-iw\tau}d\tau. \tag{2.21}$$

The spectral function can be thought of as quantifying the proportion of molecules that are tumbling with frequency w.

In the case of a simple homogeneous liquid such as water, the correlation function has a simple exponential form and the spectral function has a Lorentzian form,

$$C(t) = \exp(-t/\tau_c), \qquad \mathcal{J}(\omega) = \int_0^\infty C(t)e^{-iw\tau}d\tau = \frac{\tau_c}{1+\omega^2\tau_c^2}. \tag{2.22}$$

The time constant τ_c is called the correlation time.

As first shown by Bloembergen, Purcell and Pound (Bloembergen et al. 1948), the relaxation rates R_1 and R_2 are related to the strength of the coupling to the local dipole field $f(t)$ and to the spectral function $\mathcal{J}(w)$, as follows

$$R_1 = \frac{1}{T_1} = \frac{3}{20}\frac{\hbar^2\gamma^4}{\bar{r}^6}\Big(2\mathcal{J}(\omega_0) + 8\mathcal{J}(2\omega_0)\Big), \tag{2.23}$$

$$R_2 = \frac{1}{T_2} = \frac{3}{20}\frac{\hbar^2\gamma^4}{\bar{r}^6}\Big(3\mathcal{J}(0) + 5\mathcal{J}(\omega_0) + 2\mathcal{J}(2\omega_0)\Big), \tag{2.24}$$

where $\bar{r}$ is the mean separation between molecules.

These equations show that the longitudional relaxation is mostly dependent on the number of molecules tumbling at the Larmour frequency, In contrast, t transverse relaxation has a dependence the the low frequency fluctuations of the local magnetic field.

2.3.4 Influence of field inhomogeneity on transverse relaxation

Due to limitations in the precision of MRI equipment and slight variations in the magnetic susceptibility across tissue regions, small amounts of magnetic field inhomogeneity are always present. These slight differences mean that neighbouring nuclei will be under the influence of slightly different magnetic field strengths and will therefore precess at slightly different rates and will gradually drift out of phase. This induces additional transverse relaxation denoted by T_2' $(= 1/R_2')$. The apparent relaxation time due to the combination of intrinsic and field homogeneity related transverse relaxation is denoted T_2^* is given by

$$T_2^* = 1/R_2^* = (R_2 + R_2')^{-1}. \tag{2.25}$$

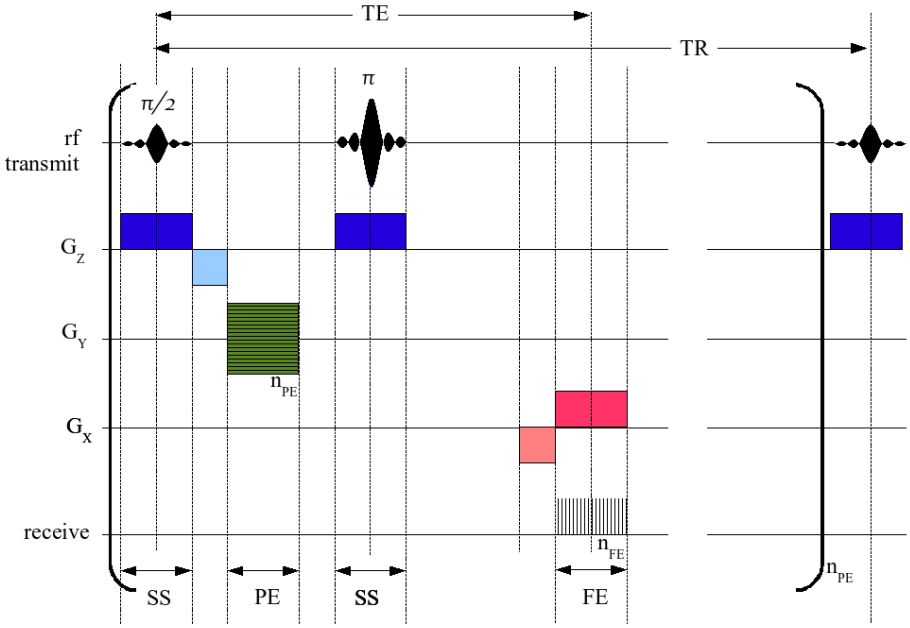

Figure 2.1: Pulse sequence diagram for a spin echo pulse sequence. The horizontal axis represent time. Image courtesy of Brownturkey - Own work, CC BY-SA 3.0, https://commons.wikimedia.org/w/index.php?curid=4179911 accessed 25-04-2017.

Usually, R_2 is the quantity of interest because it is intrinsic to the cellular environment of the sample, whilst R_2' is dependent on the uniformity of the magnetic field produced by the apparatus. The additional dependence on R_2' is therefore often considered a nuisance that adds noise, but it can sometimes be useful in indicating the presence of iron containing metabolites which alter the magnetic susceptibility of tissue thus contributing to the inhomogeneity of the B field. The transverse relaxation induced by field inhomogeneity differs from the intrinsic relaxation of the sample in that it is reversible: The de-phasing can be undone by applying a 180 degree pulse midway between sample excitation and signal acquisition to allow the magnetisation vector from neighboring nuclei to move back into alignment. This re-phasing can be used to minimise the effect of the field homogeneity on the signal making it possible to measure T_2 independent of T_2^*.

2.4 Gradients and Spatial Localisation

The diffraction limit of the RF radiation used in MRI is of the order of several metres, so positional information can not be obtained directly from the emitted signal in the same way as

for other three dimensional medical imaging modalities such as X-ray computed tomography (CT) or single photon emission tomography (SPECT). In MRI, signal localisation is instead achieved through the clever manipulation of magnetic field gradients through different stages of the acquisition sequence to encode positional information in the frequency and phase of the output RF signal.

Three Gradients are applied in three orthogonal directions and in three different ways to resolve the three spatial directions:

1. *Slice selection gradients* (G_z in Fig. 2.1) are turned on during the excitation pulses to ensure that only a narrow two dimensional plane is excited.

2. *Frequency encode gradients* (G_x in Fig. 2.1) are applied during signal acquisition. These alter the frequency of the signal depending on the location along a chosen in-plane axis.

3. *Phase encode gradients* (G_y in Fig. 2.1) are applied between the excitation and the signal acquisition so as to alter the phase of the signal depending on the location to encode positional information on the remaining in plane axis.

Information from each voxel along the frequency encoding direction can be acquired simultaneously, however obtaining all spatial information along the phase encoding and slice selection directions typically requires multiple repetitions.

2.5 Pulse sequences and signal detection

A pulse sequence specifies the timing and coordination of RF excitation pulses, gradient field pulses and image acquisition windows. An example pulse sequence is shown in Fig. 2.1. Pulse sequence parameters determine the degree of weighting that the various relaxation parameters have on the final image.

There are two main families of pulse sequences: spin echo and gradient echo. The data explored in this work used a spin echo sequence to obtain the T2-weighted images and a gradient echo for the T1 weighted images, so each of these sequences will be covered in this section. The simpler partial saturation sequence is first introduced as a warm up.

2.5.1 Partial saturation

The partial saturation pulse sequence consists of RF pulses of flip angle θ repeated at intervals of T_R, with the signal being read at a time interval of T_E after the excitation.

In general, T_R need not be large compared to T_1, so for a generic choice of T_R the longitudinal magnetisation will not fully recover before the next excitation pulse arrives.

Despite this, after the first few excitation pulses, the system will settle into a steady state where each subsequent pulse restores the longitudinal magnetisation to close to the same value it had before the previous pulse. Taking into account the effect of an RF pulse followed by exponential decay, the steady state condition

$$M_z^{\mathrm{SS}}(t) = M_z^{\mathrm{SS}}(t + T_R) \tag{2.26}$$

is found to have solution

$$M_z^{\mathrm{SS}}(t) = M_{\mathrm{eq}} \frac{1 - \exp(-T_R/T_1)}{1 - \exp(-T_R/T_1)\cos\theta}. \tag{2.27}$$

The measured signal, being directly proportional to the transverse magnetization, is therefore given by

$$\begin{aligned} \text{Signal} \propto M_\perp^{\mathrm{SS}}(t + T_E) &= \sin\theta \exp(-T_E/T_2^*) M_z^{\mathrm{SS}} \\ &= \frac{M_{\mathrm{eq}} \sin\theta (1 - \exp(-T_R/T_1))}{1 - \exp(-T_R/T_1)\cos\theta} \exp(-T_E/T_2^*) \end{aligned} \tag{2.28}$$

Note that the T_2^* weighting is determined by the echo time T_E and can be minimized by keeping T_E as short as possible. The T_1 weighting is dependent on both the repetition time T_R and the flip angle θ. If one knows the approximate T_1 for the sample being studied, then for fixed T_R, there is an optimal angle for T_1 contrast, the Ernst angle

$$\theta_{\mathrm{Ernst}} = \cos^{-1}\left(\exp(-T_R/T_1)\right) \tag{2.29}$$

obtained by maximising the RHS of Eq.2.28.

2.5.2 Spin echo

2.5.2.1 Conventional spin echo

In spin echo sequences, the initial excitation pulse always has an angle of 90°. In between these 90° pulses, 180° pulses are added which serve to cancel out any transverse relaxation due to magnetic field homogeneity. A schematic illustration of a spin echo sequence is shown in fig. 2.1.

The sequence begins with a 90 degree RF pulse which transfers the magnetization vector from its equilibrium orientation along the z-axis, into the xy-plane. The system is then allowed to relax for a period of $T_E/2$ before a subsequent 180 degree pulse is applied. After a further interval of $T_E/2$, inhomogeneity effects have been cancelled and the signal is read.

180 degree pulses continue to be applied at time interval of T_E with the RF echo read mid way between 180 degree pulses. At time T_R, a second 90 degree RF pulse is generated and the cycle repeats again. The resulting steady state signal from a spin echo sequence is

$$S \propto M_0\Big(1 - \exp(-T_R/T_1)\Big)\exp(-T_E/T_2) \tag{2.30}$$

From this equation, it is apparent that the signal increases as T_2 increases. For T_1, the reverse is true: The signal increases as T_1 decreases. If T_E is short compared to the expected value of T_2, then the T_2 dependence of the signal is minimized and we obtain a T_1 weighted sequence. Similarly, if T_R is small compared to the expected T_1 value of the sample, then the T_1 dependence of the signal is minimal and we have a predominantly T_2 weighted sequence.

As well as having T_1 and T_2 weightings, the T1w signal is also proportional to proton density (this dependence enters through M_0 in the above equation). However, because water proton density tends to be similar across brain tissue, the T_1 and T_2 weightings provide better contrast between gray and white matter tissue types.

Spin echo is excellent for measuring T_2 as it is able to remove the effect of field inhomogeneity. However as T_1 tends to be much longer than T_2 in body tissue and RF pulses take longer to apply than gradient pulses, T_1w spin echo sequences tend to have rather long acquisition times.

2.5.2.2 Fast spin echo

In conventional spin echo, data from one spatial frequency along the phase encoding direction is acquired per repetition. The scan time for a conventional spin echo sequence is therefore given by

$$\text{scan time (conventional spin echo)} = \text{TR} \times N_{\text{PE}} \times N_{\text{Slice}} \tag{2.31}$$

where TR is the repetition time, N_{PE} is the number of phase encoding steps and N_{slice} is the number of slices acquired.

In fast spin echo, the acquisition can be sped up by measuring more than one spatial frequency per repetition in the phase encoding direction. This involves applying multiple phase encode gradients within each repetition. The number of distinct spatial frequencies is called the echo train length (ETL) or turbo factor, the scan time is then given by

$$\text{scan time (fast spin echo)} = \text{TR} \times N_{\text{PE}} \times N_{\text{Slice}}/\text{ETL}. \tag{2.32}$$

Other names for fast spin echo used by various manufacturers are Turbo Spin Echo (TSE) and Rapid Acquisition with Refocused Echoes (RARE).

2.5.3 Gradient Echo

Compared to spin echo, gradient echo sequences use decreased flip angles and repetition times. In place of the 180 degree refocussing pulses used in spin echo, gradient echo sequences use gradient lobes: a de-phasing gradient pulse just after the RF excitation and a re-phasing gradient pulse just before the echo. The gradient lobes are needed to prevent the residual signal from affecting subsequent pulses. Gradients are faster to apply than 180 degree pulses enabling the echo time to be reduced.

While there is substantial speed up, this comes at the cost of introducing other forms of noise which are absent in the spin echo sequence. Notably, the effect of magnetic field inhomogeneity on the signal can no longer be negated so there is an added T_2^* dependence. A conventional gradient echo sequence uses a flip angle of about 30 degrees, however there are ultra fast 'turbo' variants of gradient echo sequence that use a much smaller angle (typically less than 10°).

The T_1w images used in this study were obtained using an ultra-fast gradient echo sequence referred to as turbo field echo by the manufacturer (Philips Medical). Other names used for ultra fast gradient echo sequences are fast low angle shot FLASH and Turbo gradient echo.

Ultrafast sequences starts with a 180° inversion pulse, followed by alternating small angle pulses (8 degrees in the case of the T1w data used in this work). Rapid gradient echo imaging is discussed in more detail in (Hargreaves 2012).

Chapter 3

Neuro-anatomical Background

3.1 Outline

This chapter provides a brief overview of some of the biology and anatomy of the human brain. Its main purpose is to add some context to assist in the interpretation of patterns of change presented in Chapter 7 and discussed in Chapter 8. The present chapter is divided into four sections. Section 3.2 discusses the microanatomy and cellular composition of the brain and explains the difference between gray and white brain matter. Section 3.3 discusses how the microanatomy of different brain tissue compartments affect the observed MR relaxation parameters. In Section 3.4, a short overview of the topographical anatomy of the brain is provided including discussion of the roles of various key brain structures.

3.2 Neuro-Microanatomy

The brain is made up of two major cell types: Neurons which are the brains information processing cells and glial cells which provide support the neurons.

3.2.0.1 Neurons

Neurons are the brains primary cell components. A neuron consists of a soma (cell body) and two types of projections, axons and dendrites, that transmit and receive electrical signals to and from other neurons, respectively. The diameter of the neuron cell bodies is in the range 0.004 - 0.1 mm. Electrical pulses ('action potentials') travel through the axons and are collected by dendrites from other neurons at special junctions called synapses. Axons are long conductive fibers that transmit electrical signals from one neuron to another. Although typically only about one μm ($=10^{-6}$ m) in diameter, axons may grow to more than ten

centimeters in length. There are an estimated 86 billion (8.6×10^{10}) neurons in the human brain, with an average of seven thousand synaptic connections for each neuron (Pakkenberg et al. 2003). Not all neurons have the same structure. There are many subtypes of neurons including sensory neurons, motor neurons, interneurons, pyramidal cells, purkinje cells and granule cells.

In most cases, it is not possible to identify specific functions of individual neurons, but it is known that there are specific neurons that respond to specific stimuli. For instance, in primates, there are neurons that have been shown to respond preferentially to particular spatial frequencies (Shapley & Lennie 1985, Priebe et al. 2006) and orientations (Hubel & Wiesel 1974, Priebe et al. 2006) .

3.2.0.2 Glial Cells

Neurons are believed to account for roughly half of the cells in the brain. The remaining brain cells are collectively referred to as glial cells. These are the support cells of the neurons. Glial cell can be classified into five main types as follows: as follows;

1. *Astrocytes* regulate the local chemical environment and blood supply. They have numerous projections which attach to axons and capillaries.

2. *Oligodendrocyte cells* make the myelin membrane, an insulating layer which coats the axons to improve their conduction velocity.

3. *Microglia* are small specialised immune cells which protect the neurons by removing pathogens and waste products.

4. *Ependymal cells* line the ventricular system and spinal cord where they produce and secrete cerebro-spinal fluid.

5. *Radial glia* are involved in neurogenesis and are most prominent in early brain development. In the mature brain some are retained in the cerebellum and retina.

Fig. 3.1 provides an image of neuron, oligodentrocyte and astrocyte cells from a rat brain.

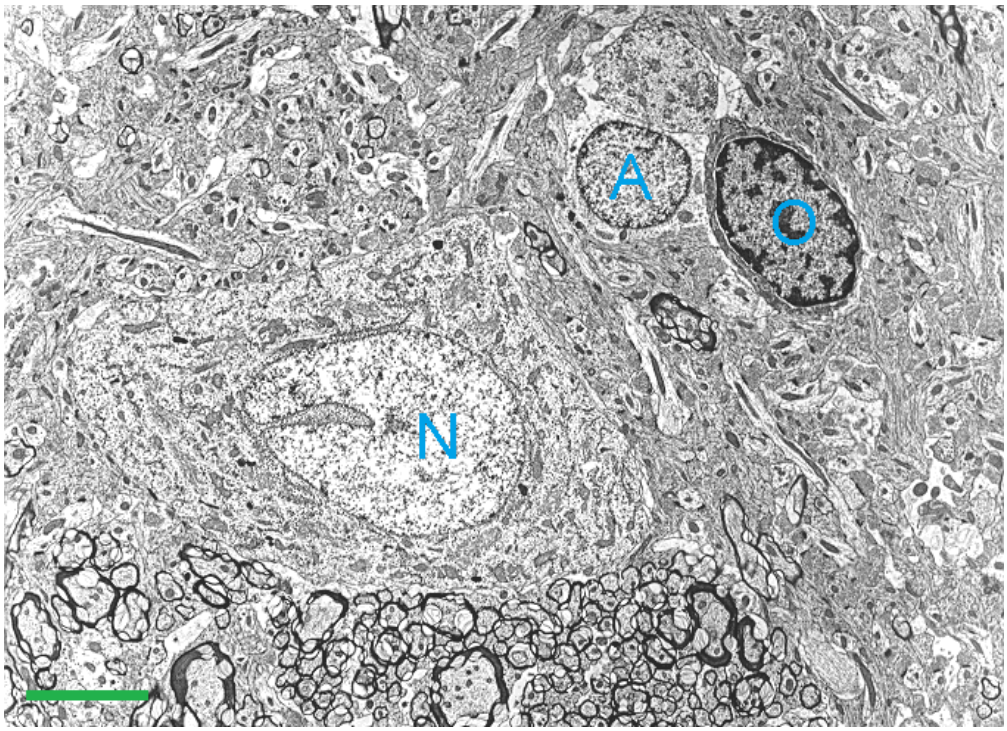

Figure 3.1: Electron microscopy image of rat brain cells, showing neuron(N), astrocyte(A) and oligodendrocyte(O) cells. The scale (green bar) is 5μm. Image adapted from the Atlas of Ultrastructural Neurocytology, http://synapseweb.clm.utexas.edu/atlas.

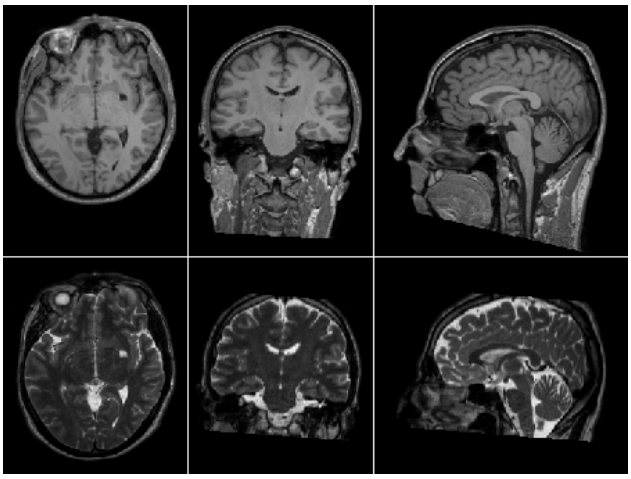

Figure 3.2: T1 weighted (top row) and T2 weighted (bottom row) magnetic resonance images of a human brain.

3.3 Appearance of the brain in MRI

3.3.1 Atomic and molecular composition of the human brain

The most abundant elements in the human body by atomic percentage are Hydrogen 62%, Oxygen 24%, and Carbon 12%.[8] Of these, carbon and oxygen both have paired protons and neutrons and therefore have zero magnetic moment making them invisible to MRI. The NMR signal from the human body is therefore dominated by hydrogen atoms. The majority of hydrogen atoms (approximately 70% in the human body and close to 80% in the brain) are bound in water molecules. About two thirds of water molecules are contained in intracellular fluid with the remaining third contained is extracellular fluid.

3.3.2 T1 and T2 relaxation times for human brain tissue

Fig. 3.2 shows T1 and T2 weighted brain images from a (randomly chosen) normal subject.

The cerebral spinal fluid, present in the ventricles and peripheral regions of the brain, is very bright on the T2 images (indicating relatively slow T2 relaxation time) and dark on the T1 images (indicating that T1 relaxation is also relatively slow).

Recall from Subsection 2.3.3 that T_1 relaxation is most strongly influenced by the number of fluctuating molecules with tumbling rate near to the Larmor frequency while T_2 relaxation is strongest for very slowly fluctuating field.

The appearance of the CSF is therefore consistent with a runny low viscosity fluid made

[8]These ratio's are based on healthy weight individuals, and may vary considerably, especially in obese patients.

up of small fast moving molecules, most of which are tumbling at rates greater than the Larmor frequency, making both T_1 and T_2 relaxation inefficient. Indeed CSF is 99% water.

Living tissues are much more complicated than simple liquids or solids due to their heterogeneous compositions and the presence of semi-permeable membranes which interact with the water molecules. Within the brain, there are two main tissue compartments: white matter regions that consist primarily of myelinated axon fibers and gray matter regions consisting primarily of neuron cell bodies and synapses. Gray matter is more metabolically active than white matter and has a higher rate of perfusion.

The contrast between gray matter and white matter regions is apparent on both T1w and T2w images. In the T1w image white matter appears brighter than gray matter (indicating more efficient longitudinal relaxation in white matter than in gray matter). In the T2w image, white matter is darker, indicating more efficient transverse relaxation in white matter than in gray matter.

3.3.3 MR contrast and Myelin

The source of this contrast between gray and white matter is the myelin sheaf that surrounds the axon fibers (Stueber et al. 2014). The lack of contrast between gray and white matter in neonate brains, whose axons are not yet myelinated confirms this. The myelin content of white matter is substantial, with myelin making up about one quarter of the wet mass and one half of the dry mass of white matter in adults.

The mechanism by which myelin is able to generate these increased relaxation rates has been studied in detail by Koenig and collaborators (Koenig et al. 1990, Koenig 1991, Koenig 1995). The following discussion is based on these references. Chemically, myelin is a phospholipid with a high cholesterol content. It is the cholesterol that has the greatest effect on relaxation through its hydrophilic hydroxyl and phosphate groups. The presence of these groups results in an interaction strength between water and myelin that is significantly higher than for typical cell membranes.

The myelin sheaf consists of a dozen or so concentric rings of phospholipid membrane interspersed with thin layers of water. Only a small percentage of water sits within these myelin membrane layers. The vast majority of the water is located either in the region between the axon fiber and the innermost myelin membrane or in the extracellular space outside the myelin sheaf. At physiological temperatures, the myelin membrane has high permeability to water so that there is substantial exchange of water molecules within the myelin layers with water molecules outside of them. This allows interactions of many different water molecules with the hydroxyl and phosphate groups on the myelin sheaf (over the time

scales T_R, T_E) of a typical MRI measurement.

In summary, it is the combination of the presence of strongly interacting sites on the myelin, the high surface area of the myelin and its high permeability allowing a constant turn over of water molecules in the vicinity of the myelin membrane, that leads to the unusually high relaxation rates observed for white matter.

3.3.4 Iron and T2w contrast

3.3.4.1 Iron in the brain and body

Most iron in the body is found in red blood cells as a key component of the haemoglobin protein used to bind oxygen in red blood cells. Non-haemoglobin (non-haeme) iron is also present in the body in significant quantities and plays a number of other important roles in the body such as the synthesis of adenosine triphosphate (ATP) in mitochondria. In the brain, non-haeme iron is used in a number of important cellular processes including the synthesis of myelin, neurotransmitters and monoamine oxidases. Of all organs, only the liver has a higher non-haeme iron concentration than the brain. Iron concentration is estimated to be between two and four times higher in gray matter than in white matter (Connor et al. 1990), with iron content being highest in the globus palidus and parts of the midbrain (red nucleus and substantia niagra). Iron levels in the brain are low at birth, but rise steadily through childhood and plateau in most regions by middle age (Hallgren & Sourander 1958).

3.3.4.2 Relationship between T2 relaxation and iron content

Non-haeme iron is found mostly in three protein binding complexes: ferritin, haemosiderin and transferrin. In the brain, ferritin is approximately ten times more abundant than transferritin (Connor et al. 1992) and it is ferritin and hemosiderin that have the dominant impact on the MR signal (Schenck 2003). An unresolved puzzle is that ferritin in the brain tends to have a greater influence on MR signal than ferritin *in vitro*. This effect is thought to be due to the way ferritin aggregates in the brain.

Non-haeme iron is wrapped in a protein shell that shields it from the surrounding water molecules, so it's influence on the water molecules which carry the MR signal is indirect. The effect of ferritin on water molecules occurs through the so called outer shell mechanism (Schenck 2003), which results in an increase in T2 relaxation rate, with minimal corresponding change to the T1 relaxation rate (Schenck 2003), (Brass et al. 2006).

The dependence of T1 and T2 on iron using postmortem human and monkey brain samples was analysed in (Vymazal et al. 1996) with a linear correlation between transverse relaxation rate and iron concentration reported.

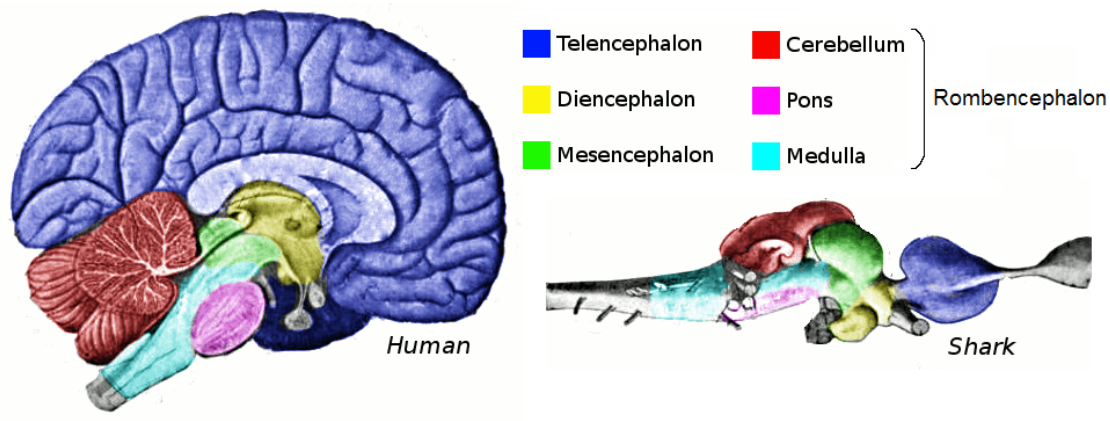

Figure 3.3: Vertebrate Brain regions. Figure adapted from Ranson, S.W. "The Anatomy of the Nervous System: From the Standpoint of Development and Function", WB Saunders, 1920. Public domain via wikimedia commons.

(Stueber et al. 2014) used correlations between and proton induced X-ray emission (PIXE) spectroscopy on post mortem human brains to show that iron is the dominant contribution to T2* contrast.

3.4 Topographical anatomy of the brain

3.4.1 Anatomical subdivisions of the brain

Though much about the brain's functioning remains unknown, its structural anatomy is well studied and has been mapped out in great detail. To get an initial broad overview of the brain's topography, one can begin with its initial formation in embryogenesis where distinct regions first begin to emerge. In vertebrate species, the four areas that become differentiated from very early on in embryological development are illustrated in Fig. 3.3. At the tip of the neural tube is the telencephalon (forebrain) which ultimately goes on to form the right and left hemispheres of the Cerebral cortex along with a small midline component called the lamina terminalis and various deep nuclei such as the putamen and globus pallidus. The diencephalon (interbrain) goes on to form the thalamus and hypothalamus. Further down is the mesencephalon (midbrain) and rhombencephalon (hindbrain), the later goes on to form the cerebellum, pons and medulla. A distinctive feature of mammals and the human brain in particular is the enlargement of the telencephalon/cerebral cortex relative to the other brain structures. This is not the case for many creatures. In the shark (Fig. 3.3), the telencephalon is comparable in size to the other primitive brain structures. In some fish (mormyids), it is the cerebellum which is greatly enlarged relative to other brain regions.

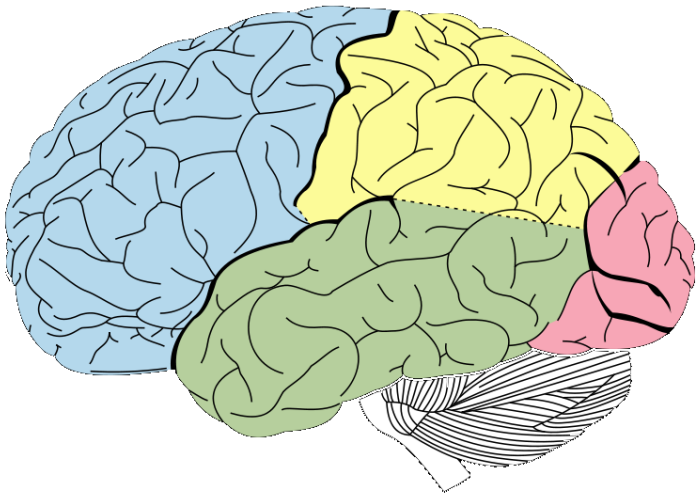

Figure 3.4: Lobes of the cerebral cortex: Frontal (blue), Temporal (Green), Parietal (yellow) and Occipital (Pink). Dark lines indicate fissures, while lighter lines indicate sulci. Figure adapted from Gray's anatomy (Gray 1918)

3.4.2 Cerebral Cortex

The human cerebral cortex has the structure of a large sheet 2-4 mm thick, intricately folded to accommodate a surface area of 2500 cm^2. The surface of the cortex consists of flat ridges (gyri) separated by crevices (sulci or fissures). The sulci and gyri provide landmarks that help define and delineate cortical regions.

The more prominent sulci and fissures are used by anatomists to subdivide the cortex into frontal, temporal, parietal and occipital lobes as shown in Fig. 3.4. A fifth lobe, the limbic lobe located on the medial side of the cortex is also distinguished by some authors. To a large extent distinct brain regions have distinct specialised functions. At the same time, most activities draw on interactions between various different lobes and subcortical areas. Brain areas are often stratified into sensory, motor and association areas.

The frontal lobe plays a key role in executive function. The temporal lobe is involved in higher level auditory processing. The occipital lobe is heavily involved in visual processing. The left parietal lobe contains sensory areas and areas used for associative learning. The limbic lobe is associated with emotional processing and interoceptive awareness.

Within the cortex, there are up to six distinct layers, each having different characteristic neuron cell types. This layered structure is illustrated in Fig. 3.5.

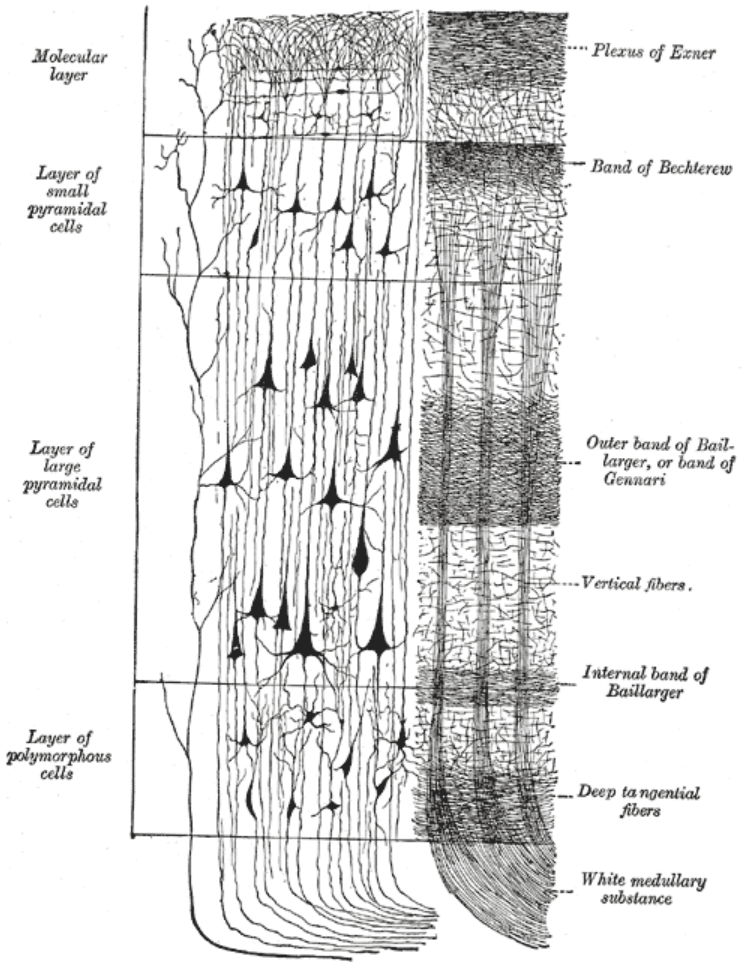

Figure 3.5: Cross sectional illustration of the layers of the cortex. Adapted from Gray's anatomy (Gray 1918).

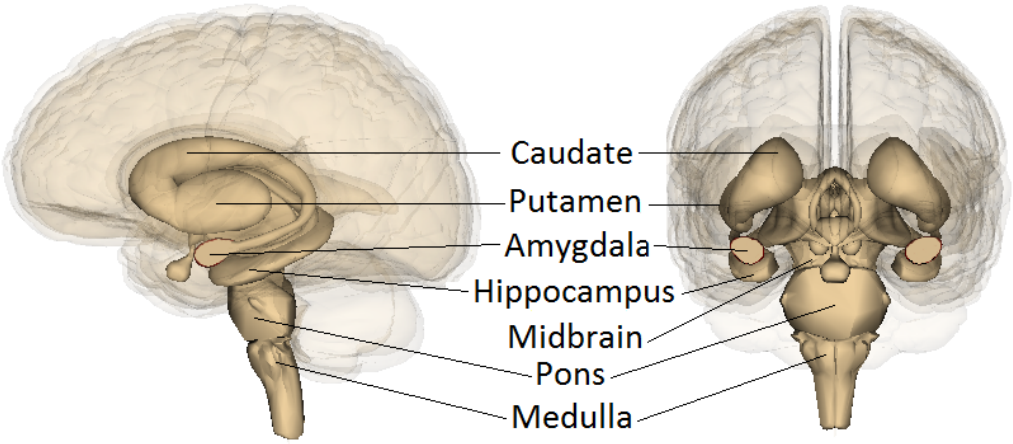

Figure 3.6: Subcortical structures of the human brain. Adapted from images generated from the Life Science Databases(LSDB, website: lifesciencedb.jp) via Wikimedia Commons.

3.4.3 Subcortical brain areas

This section describes key subcortical brain regions shown in Fig. 3.6 and Fig. 3.7.

3.4.3.1 Hippocampus and Amygdala

The hippocampus and amygdala are key structures nestled in the inner temporal lobes (Fig. 3.6). Both are involved in memory. The Hippocampus is more strongly associated with declarative memory (memories that can be consciously declared) and plays a significant role in memory consolidation and indexing. It is also heavily involved in spatial orientation and navigation. In contrast, the amygdala is most prominently involved in subconscious instinctive aspects of memory response. It is involved in the association of emotions to memories and sensory stimuli and, for example, plays a key role in fear conditioning.

3.4.3.2 Striatum and basal ganglia

The striatum contains a head portion called the putamen and a tail portion called the caudate nucleus, which arcs around and terminates on the posterior side of the amygdala (Fig. 3.6).

The striatum is part of the basal ganglia, a dispersed network of brain structures responsible for sensorimotor coordination including response selection and initiation (See Fig. 3.7).

The striatum serves as a major input gateway for signals traveling from the cortex,

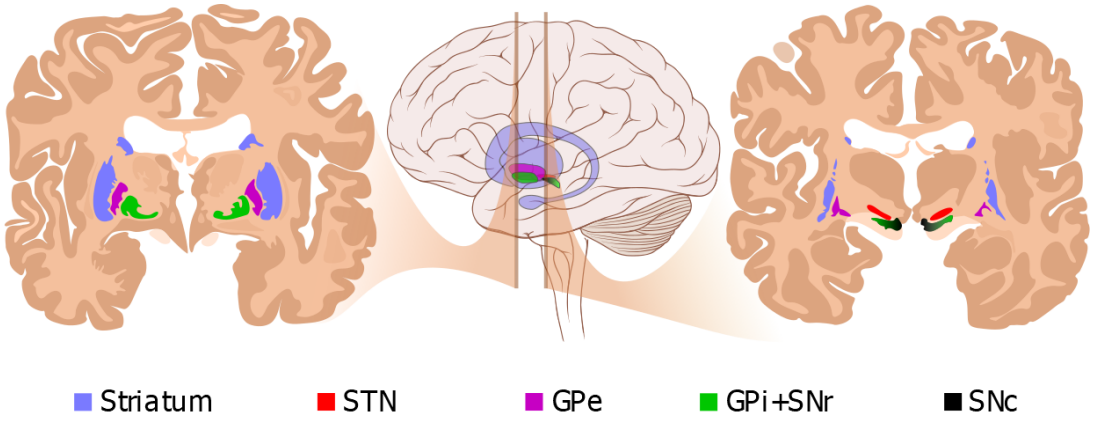

Figure 3.7: Basal Ganglia brain structures. Striatum (Putamen and Caudate nucleus), subthalamic Nucleus (STN), Globus Pallidus external (GPe), Globus Pallidus internal (GPi), Substantia Niagra pars reticulata(SNr) Substantia Niagra pars compacta (SNc). Figure by user:Jlienard via wikimedia commons, produced with Inkscape software and based on works by Andrew Gillies, Mikael Haggstrom and Patrick J. Lynch.

amygdala and hippocampus to the basal ganglia. The striatum is also a key part of the brain's reward system which drives motivation. It interacts with many neurotransmitters including dopamine and glutamate.

Medial to the putamen is the globus pallidus, also part of the basal ganglia, and involved in the regulation of voluntary movement.

3.4.3.3 Thalamus

The thalamus distributes and relays sensory information to the cerebral cortex. It also relays information between the cerebral cortex and subcortical brain structures.

3.4.3.4 Hypothalamus

The hypothalamus originates from the ventral part of the diencephalon, and is about the size of an almond. It is a key interface between the nervous, autonomic and endocrine systems. It plays a key role in regulating body temperature, thirst, appetite, sleep, mood and sex drive.

3.4.3.5 Brainstem: Midbrain, Pons and Medulla

The Brainstem is divided into three components the inferior part contiguous with the spinal chord is the medulla oblongata. The central oblong part of the brainstem which bulges out on the anterior side is the pons. The remaining superior portion of the brainstem is the midbrain. (See Fig. 3.6) Contained in these structures are a diverse collection of nuclei

with functions mostly related to the autonomic nervous system that regulates basic body functions such as digestion, blood pressure, body temperature and sweating.

The medulla contains autonomic centres which control cardiac and respiratory function. Reflex behaviours such as coughing, sneezing and vomiting are triggered in the medulla.

The pons contains nuclei that relay information between the cerebral cortex and the cerebellum and is involved in REM sleep.

The Midbrain contains several key nuclei including the superior colliculi which are involved in visual reflexes, the inferior colliculi which process and relay auditory information and the substantia niagra which is a key dopaminergic centre involved in the reward system and in movement.

Straddling nuclei from all three brainstem substructures is the reticular activation system which regulates arousal, sleep and wakefulness.

3.4.3.6 Cerebellum

Like the cerebral cortex, the cerebellum has a folded structure but the folds of the cerebellum have a more laminar structure. The cellular composition of the cerebellar cortex is also quite different to the cerebral cortex with a much higher density of neurons and a smaller proportion of glial cells. The cells in the cerebellum are arranged in three discernable layers: The molecular layer, the purkinje cell layer and the granular layer. The cerebellum is involved in adaptive motor control and motor learning.

3.4.4 White matter tracts

There are numerous white matter tracts (many of which are illustrated in Fig. 3.8) These fiber tracts facilitate the exchange of information between brain regions and are classified into three basic types: commissural fibers, association fibers and projection fibers. Commissural fibers connect the two hemispheres of the cortex. Association fibers run between different cortical regions of the same hemisphere. Projection fibers connect the cortex with subcortical structures such as the thalamus, midbrain, brainstem and spinal cord.

Commissural fibers include the corpus callosum, fornix, the anterior and posterior commissures and the habenular commissure. Association fibers include the uncinate fasciculus, cingulum, arcuate fasciculus, superior longitudinal fasciculus, inferior longitudinal fasciculus and the occipito-frontal fasciculus.

Most projection fibers travel through the internal capsule/corona radiata (The two structures are contiguous with one another, the internal capsule being ventral to the corona radiata). A distinction can be made between ascending projection fibers which carry electrical

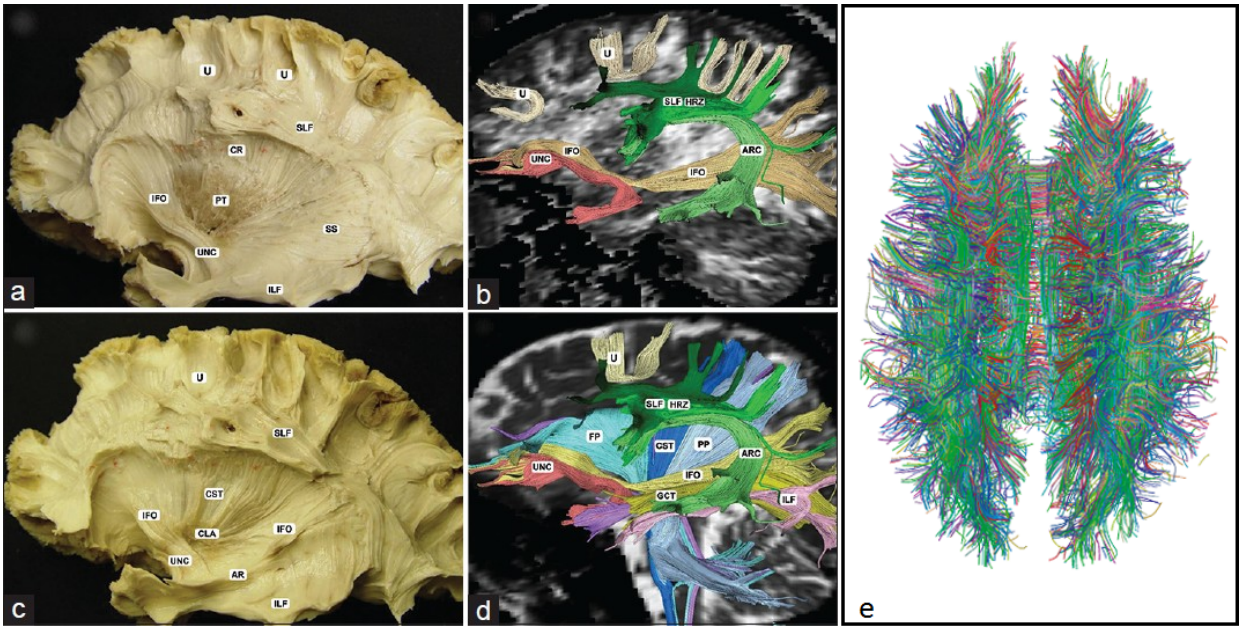

Figure 3.8: White matter brain dissections (**a** and **c**) compared with a segmentation into major fiber tracts (**b** and **d**) based on tractography analysis of diffusion tensor images. Part **e** shows a diffusion tensor image of white matter tracts in a brain from above, with the colours encoding the fiber direction. Part **e** of this figure is taken from (Gigandet et al. 2008), while parts **a-d** are from (Dini et al. 2013), both via Wikimedia Commons. Tract labels are as follows: ARC arcuate fasciculus; CLA claustrum; CR corona radiata; HRZ horizontal segment; IFO inferior fronto-occipital fasciculus; ILF inferior longitudinal fasciculus; PT putamen; AR auditory radiation; SLF superior longitudinal fasciculus; SS sagittal stratum; UNC uncinate fasciculus; U U fibers; GCT geniculocalcarine tract; CST corticospinal tract; PP parietopontine fibers; FP frontopontine fibers.

signals from subcortical areas to the cortex, and descending projection fibers which transmit signals from the cortex to subcortical areas.

A good atlas of white matter tracts, based on high resolution MRI, is (Mori et al. 2005).

3.4.5 Lateralisation of brain function

Although structurally the brain exhibits a high degree of bilateral symmetry, many brain functions are lateralised to particular hemispheres. In most people verbal tasks are performed predominantly by the left hemisphere. This is why strokes which damage the left hemisphere are much more likely to lead to the loss of speech. Another well known manifestation of brain lateralisation is the strong preference people have in using a particular side of their body for complex tasks such as writing or throwing. The right and left amygdala have also been found to respond differently to stimuli (Baas et al. 2004), and there is even evidence of an interaction between lateralisation of amygdala function and gender (Cahill et al. 2004).

3.4.6 Age related changes in the human brain

Profound changes in the brain occur over a persons life span. When babies are born, the brain is still developing and there is no axonal myelin sheath (Aubert-Broche et al. 2008). The brain develops rapidly in early life but takes two decades before it is fully developed. Once adulthood is reached, there is a gradual loss of white and Gray matter over the following decades (Peelle et al. 2012).

In patients with neuro-degenerative disease such as Alzheimer's disease, brain tissue loss is greatly accelerated. One of the challenges for neuro-imaging is to develop the ability to distinguish pathological changes from normal age related changes.

3.4.7 Gender differences in the human brain

Brain differences related to gender are reviewed in (Cosgrove et al. 2007). Men have a larger brain size in line with their larger overall body size, while women have a greater ratio of Gray matter to white matter.

Ghisleni et al (Ghisleni et al. 2015) reported increased cerebellar perfusion in females. A large study (Cao et al. 1999) found differences in the connectivity patterns of male and female brains revealed by functional MR imaging.

Chapter 4

Preparing Medical Images for Statistical Analysis

4.1 Chapter outline

Section 4.2 of this chapter discusses the digital storage of medical images. To perform meaningful statistical comparisons between MR images, adjustments for differences in brain shape and orientation must first be applied. The process of calculating and implementing these adjustments is referred to as 'image registration' or 'spatial normalisation' and is discussed in Section 4.3. Section 4.4 discusses the segmentation of MR images into gray matter, white matter and other tissue class probability maps. In the final section, the option of spatially smoothing the data to improve the sensitivity of the statistical analysis is discussed.

4.2 Medical Image Data

A medical image I can be idealized mathematically as a function $I : \mathbb{V} \rightarrow \mathbb{R}$. Where $\mathbb{R}$ represents the image intensity and $\mathbb{V}$ represents the physical three dimensional region (volume) of which the image was taken. In practice all images have a finite resolution and are stored in finite dimensional arrays. To facilitate data storage, the volume in which the imaged object resides is partitioned into a large but finite number of discrete volume elements called voxels. A voxel is the three dimensional analog of a two dimensional pixel.

Accompanying the image data is so-called header data which provides important ancillary information including patient identification details, pulse sequence parameters, orientation of the patient with respect to the scanner, size of the voxels and field of view, scan time and

other acquisition parameters.

4.2.1 Medical Image File Formats

All major MRI system manufacturers use an image file format known as DICOM (Digital Imaging and Communications in Medicine). Unfortunately, because DICOM is devised for a very wide range of imaging modalities, the format can be rather unwieldy as it contains an enormous number of header fields (tags). The current DICOM standard document runs to hundreds of pages and encompasses many imaging modalities across radiology and nuclear medicine and within the DICOM format there are a lot of different ways of saving the data. A simpler more rigid format called NIFTI (Cox et al. 2004) (an acronym for Neuroimaging Informatics Technology Initiative) has been developed specifically for neuroimaging and is now the image format of choice for quantitative analysis of neuroimaging data sets.

4.2.2 Image Orientation

The structure of the human body and many of its organs including the brain exhibit a large degree of bilateral symmetry. There is therefore a risk of misidentification between left and right image structures. This is exacerbated by the use of two different conventions within the neuro-imaging research community labelled radiological convention and neurological convention. In neurological convention, the left side of the patient appears on the left hand side of the page or computer screen. In radiological convention, the left side of the patient appears on the right hand side of the page or computer screen. This convention has its origin in the use of analogue x-ray films prior to the introduction of digital computer imaging technology. Radiological convention is still the convention used by reporting doctors when assessing patient images. In this work all images will be displayed in radiological convention.

4.2.3 Software Packages

The voxel based statistical analysis in this work was performed using the software package SPM (www.fil.ion.ucl.ac.uk/spm/), a freely available image analysis package developed by Friston et al. at University College London beginning in the 1990's (Friston 1994, Friston et al. 2003). It is written in the scientific computing language MATLAB. While SPM was the first neuroimaging package to gain widespread use, there are now a number of other popular software packages, including FSL (https://www.fmrib.ox.ac.uk/fsl) and ANTsR (picsl.upenn.edu/antsr/), that are able to perform similar analysis.

4.3 Registration and Spatial Normalization

Image registration concerns the computation of transformations which bring one medical image (the source or moving image) into alignment with another image (the fixed, target or template image). Spatial Normalization and Co-registration refer to image registration applied in particular contexts: Spatial normalisation refers to bringing images from multiple subjects into alignment with a common template. Co-registration refers to bringing different images of a single subject into alignment with one another.

A registration algorithm can be divided into the following components,

1. The similarity measure which evaluates how well the alignment is between images and facilitates the optimal solution.

2. The transformation model, which specifies how rigid or constrained the class of admissible transformations is.

3. The method of optimisation which governs how the solution is found. In the case of a nonlinear transformation model, this includes some form of regularisation which penalises excessive amounts of deformation to avoid over fitting.

These components will be discussed in more detail in the following subsections.

4.3.1 Similarity Measures

The similarity measure is a measure of how well two images are aligned. There are three main options for the similarity measure: the sum of square differences (SSD), the mutual information (MI) and the cross correlation (CC).

The *sum of square differences* for images I_1 and I_2 is defined as

$$\mathrm{SSD}(I_1, I_2) = \sum_v \Big(I_1(v) - I_2(v)\Big)^2 \tag{4.1}$$

where the sum runs over all voxels v in the image.

The *mutual information* is defined in terms of the joint histogram $p(Y_1, Y_2)$ which expresses the liklihood that a randomly chosen voxel v will have values $I_1(v) = Y_1$ and $I_2(v) = Y_2$. Writing $p_1(Y)$ and $p_2(Y)$ for the image intensity histogram for the two images, the mutual information is given by

$$\mathrm{MI}(I_1, I_2) = \sum_{i,j} p(Y_i, Y_j) \log \frac{p(Y_i, Y_j)}{p_1(Y_i) p_2(Y_j)}. \tag{4.2}$$

where the sums over i and j run over the intensity values in the images I_1 and I_2 respectively.

A related quantity is the normalised mutual information (NMI) defined as

$$\mathrm{NMI}(I_1, I_2) = \frac{H(I_1) + H(I_2)}{H(I_1) + H(I_2) - \mathrm{MI}(I_1, I_2)} \tag{4.3}$$

where $H(I_a) = -\sum_i p_a(Y_i) \log(p_a(Y_i))$. The NMI is often favoured over the MNI as it is more robust in handling transformations that change the degree of overlap between two images (Studholme et al. 1999).

The MI and NMI have a very high degree of symmetry (for instance they are invariant with respect to permutations in voxel locations) and are remarkably effective in their ability to bring images from different modalities into alignment.

The *cross correlation* (CC) is defined as

$$\mathrm{CC}(I_1, I_2) = \sum_v \frac{\Big(\sum \big(I_1(v + x_j) - \mu_1(v)\big)\big(I_2(v + x_j) - \mu_2(v)\big)\Big)^2}{\Big(\sum_k \big(I_1(v + x_k) - \mu_1(v)\big)^2\Big)\Big(\sum_l \big(I_1(v + x_l) - \mu_1(v)\big)^2\Big)} \tag{4.4}$$

Where the sums over i, j and k run over the indices of a window W centered at v, and μ_i is the average for image I_i taken over the window W. Typically, the window size is no more than a dozen voxels.

The CC is more computationally intensive than the SSD and MI because it's value at each voxel depends on the values of neighbouring voxels. Like the mutual information, the cross correlation can be used to register images for different modalities.

Tustison et al (Tustison et al. 2014) have argued that the use of the SSD may bias subsequent statistical analysis and therefore advocate using either the CC or MI instead.

Transformations	Group	Dimension	Preserves	Includes
Isometry/Rigid	$SO(3,\mathbb{R}) \ltimes \mathbb{R}^3$	6	distances, angles	rotations, translations
Similarity	$O^+(3,\mathbb{R}) \ltimes \mathbb{R}^3$	7	angles	+isotropic zoom
Affine	$GL(3,\mathbb{R}) \ltimes \mathbb{R}^3$	12	parallelness of lines	+anisotropic zoom, shears
Projective	$PGL(4,\mathbb{R})$	15	straightness of lines	+'perspectivity' transforms
Diffeomorphism	$\mathrm{Diff}(\mathbb{R}^3)$	∞	smoothness of lines	+nonlinear transforms

Table 4.1: Classes of spatial transformations in order of increasing flexibility. The most common transformation groups used in medical image registration are the rigid, affine and diffeomorphism groups.

4.3.2 The Transformation Model

How well two images can be brought into alignment depends greatly on the degree of flexibility in the class of transformations that are allowed. A list of possible transformation classes is provided in Table 4.1. The most restrictive class of transformations normally considered are the isometries (also known as rigid transformations) which preserve all distances and angles. The isometry group of three dimensional space is six dimensional and is generated by three rotations and three translations. One can extend this to include an isotropic zoom degree of freedom (similarity transformations), and further still, to the group of affine transformations which in addition includes three shears (which map rectangles to parallelograms) and three (anisotropic) zooms. The transformations mentioned so far are linear: they all map straight lines to straight lines.

For immobile organs like the brain, rigid or affine transformations are usually adequate for aligning different images of the same subject, however for matching different images of moving organs or images of different subjects to one another requires a much more flexible class that includes non-linear transformations: transformations that in general map straight lines to curves. Registration using non-linear transformations is sometimes referred to as deformable registration. The most natural class of nonlinear transformations to consider are the diffeomorphisms. A diffeomorphism is an invertible transformation ϕ, such that both ϕ and it's inverse ϕ^{-1} are continuous and differentiable infinitely many times, ensuring that a smooth curves is always mapped to another smooth curve without any sharp kinks being introduced. Diffeomorphisms have the desirable property of preserving the topology of regions in the image, in the sense that simply connected regions will never be pinched together to form multiply connected regions, a property not guaranteed for more general nonlinear maps.

4.3.3 Nonlinear spatial normalisation and Regularisation

In contrast to the linear case, the space of diffeomorphisms (or more general nonlinear transformations) is infinite dimensional.[9] It is therefore necessary to limit the amount of deformation applied in order to avoid over-fitting, so that a healthy balance is achieved between having sufficiently good overlap between the two images without having extreme contortions that attempt to match every minute difference between the two images. This penalty that is applied to limit extreme deformations is called the regularisation.

[9] Although in practice, the deformation maps are discretised into voxels which renders the degrees of freedom finite, the number of free parameters is still enormous (typically three times the number of voxels), making the optimisation problem undetermined if there is no regularisation term.

Most of the leading nonlinear spatial normalisation algorithms used (including the two trialled in this work) are defined in terms of the formalism of classical field theory. In this approach, the diffeomorphism that maps an image I_0 to a deformed image I_1 is encoded by a one parameter series $\phi_t : I_0 \mapsto I_t$. The map ϕ_t is typically constructed by integrating a vector field v called the velocity vector field.[10] A Lagrangian of the form

$$\mathcal{L}(t) = \mathcal{T}(t) - \mathcal{V}(t) = \frac{1}{2}\int_X ||\hat{L}v(t,x)||^2 d^3x - \mathcal{V}(I_t, I_{\text{target}}). \tag{4.5}$$

determines the optimal solution for ϕ_t, where the integral is over the image X.

The regularisation is encoded in the 'kinetic energy' term $\mathcal{T}(t)$ via the inertia operator $\hat{L}$ which is usually taken to be the inverse of the gaussian smoothing operator. This in effect means that components of the velocity fields with shorter spatial wavelength incur a higher energy penalty than components with longer wavelengths.

The 'potential energy' term $\mathcal{V}(t) = \mathcal{V}(I_t, I_{\text{target}})$ is proportional to the similarity metric (Subsection 4.3.1) with sign chosen so that $\mathcal{V}$ decreases with increasing image similarity.

The optimal deformation is determined by the principle of least action. With the solution found numerically using a gradient descent algorithm.

4.3.4 Available spatial normalisation algorithms

There are numerous spatial normalisation software packages and algorithms available. Fourteen registration algorithms were systematically evaluated against one another in Klein et al (Klein et al. 2009). Overall the best performing algorithm was the symmetric normalisation algorithm SyN, part of the Advanced Normalisation Tools (ANTs) package (Avants et al. 2008). The SPM toolbox DARTEL (Ashburner 2007) also performed well, ranking fourth overall. These two algorithms were trialled in this work as described in Chapter 6, Subsection 6.3.3.

4.3.5 Human brain atlases

In order to compare of the results from different research studies done with different cohorts, and to identify and to correlate results with underlying anatomy, it is desirable to have a reference brain atlas with which to compare locations of activations or changes observed in different studies.

The first widely used digital atlas was constructed by Talairach and Tournoux (1988) from photographs of a dissected brain (Talairach & Tournoux 1988). They introduced the

[10] The velocity field v may be time dependent or time independent depending on the algorithm used.

convention of defining the origin as the location of the anterior commissure.

With the emergence of MR imaging, new digital templates have been constructed. The most commonly used template, which has largely superseded the TT template, was constructed by the Montreal Neurological Institute based on 305 MR brain images. The template was affine coregistered to the Talairach-Tournoux atlas but due to different shape of the two images and the constrained linear nature of the map, the matching is only approximate and a nonlinear transformation is necessary to compare NMI co-ordinates to TT coordinates (Lancaster et al. 2007). Another version of the MNI template, the ICBM-152 template has since been produced.[11] There is a left-right symmetric variant of the ICBM152 MNI template which has perfect bilateral symmetry that is convenient for identifying left-right asymmetries in images. While there are slight differences between the ICBM152 and MNI305 templates and their asymmetric/symmetric variants (Lancaster et al. 2007), all are considered faithful representations of 'MNI space'.

4.4 Segmentation

Segmentation is the separation of an MRI image into different tissue classes. In the case of the brain, the major tissue components are gray matter, white matter and cerebro-spinal fluid. Although this work is primarily focussed on the direct analysis of T1 and T2 weighted imagesets, one of the spatial normalisation algorithms trialled (DARTEL) requires segmented images. For completeness, statistical analysis is also applied to the segmented images in the form of voxel based morphometry (VBM). VBM can be used to detect local volume changes relative to overall brain volume, or the volume of particular tissue classes (gray or white matter) volumes. This information may aid in the interpretation of T1w and T2w results.

SPM's unified segmentation algorithm (Ashburner & Friston 2005) uses a gaussian mixture model in which the distribution of T1w intensity values for each tissue class is modelled by a gaussian distribution, such that the T1w intensity histogram is fit by a superposition of gaussian distributions.

The SPM segmentation algorithm also performs registration of the T1w image to a tissue probability map containing probabilistic information about the spatial distribution of the various tissue components derived from preexisting data. For each tissue component, the segmentation algorithm assigns a tissue probability to each voxel based on both it's intensity and location.

[11] By coincidence the data set used in this work also has 152 subjects; however, the dataset used here is different from the one used to construct the icbm152 template.

4.4.1 Volumetric analysis and modulation

There are two ways to apply a deformation to an image. The simplest method interpolates the voxel values such that image intensity is preserved. This is appropriate for the analysis of T1w and T2w, where one is looking at changes in tissue composition.

For voxel based morphometry, where one is interested in tissue volume, the normalisation is instead applied in such a way that the tissue volumes are preserved. This procedure is referred to as 'modulation' and is implemented by dividing the voxel values of the warped images by the voxel values by the jacobian of the normalisation map. Unmodulated segmented images reflect the probability the tissue in each voxel belongs to a particular tissue class and can never have a value greater than one. In contrast, modulated tissue probability images may be greater than one, in which case they represent a volume of tissue that is larger than the voxel size for the template image.

4.5 Smoothing and the trade off between noise and resolution

For the statistical analysis of medical images, (and in some cases to aid the visual reporting by physicians), images can be smoothed to reduce noise. Smoothing increases the signal to noise ratio at the expense of reducing the spatial resolution. Smoothing is usually implemented by convolving the image with a Gaussian distribution

$$G(x,y,z) = \frac{1}{\sigma\sqrt{2\pi}} \exp\left(-\frac{x^2+y^2+z^2}{2\sigma^2})\right). \tag{4.6}$$

The blurring parameter σ is typically set at between 4 and 12 mm.

In this work, in order to maintain high resolution, smoothing has not been applied. This was feasible because the large number of subjects provided an unusually high signal to noise ratio. For research studies with smaller numbers of subjects, smoothing is advisable in order to enhance statistical power, albeit with the loss of some resolution. More sophisticated denoising algorithms with edge preserving properties such as anisotropic diffusion (Weickert 1998) are likely to be more optimal than the traditional gaussian smoothing approach.

Chapter 5

Voxel Based Statistical Analysis

5.1 Chapter outline

In the previous chapter, the procedure of spatial normalisation was described. Once spatial normalisation has been applied to a data set, meaningful statistical comparisons can be made on a voxel by voxel basis.

Section 5.2 introduces standard statistical parameters that are used to rank the strength of the evidence the data provides against a chosen null hypothesis. Typically the Null hypotheses considered are assertions that there is no systematic difference between brain data from disease and control populations, or more generally, that there is no correlation between brain data and a given clinical variable. The general linear model (GLM) provides a means of studying more complex relationships involving multiple variables.

Voxel based statistical Analysis (VBSA) involves performing statistical tests on many voxels simultaneously and this must be taken into account when assessing the overall significance of the results. In Section 5.3, issues surrounding the statistical analysis of images are discussed including adjustment for multiple comparisons and the use of cluster based statistical measures. Section 5.4 discusses non-parametric statistical analysis, an alternative approach which allows some weakening of assumptions about the statistical distribution of the data, but requires far more computational processing resources than the more traditional parametric approach.

Intensity normalisation algorithms are discussed in Section 5.5.

5.2 Statistical tests

5.2.1 The t-statistic

In biomedical studies, one frequently encounters the problem of assessing the likelihood that an observed pattern seen in the data could have arisen by chance. In the present work, differences in the MR signal level between male and female groups at particular brain locations are examined. In a more typical application, the two groups would be a healthy control group and a disease group. Inevitably in any real world experiment, one expects there to be at least some small difference between the groups. The key question is whether the observed difference is large enough that one can be confident that there is a genuine effect that is reproducible. How significant the difference between the means of the two groups for a given variable y is assessed by computing the t-statistic

$$t = \frac{\overline{Y}_1 - \overline{Y}_2}{\sqrt{\frac{s_1^2}{n_1} + \frac{s_2^2}{n_2}}} \tag{5.1}$$

where n_1 and n_2 are the number of subjects in the two study groups and s_1^2 and s_2^2 are the sample variances

$$s_i^2 = \frac{1}{n_i - 1} \sum_j (Y_j - \bar{Y}_i)^2, \tag{5.2}$$

and $\overline{Y}_1$ and $\overline{Y}_2$ are the within group means for the variable of interest. (In our case MR signal level at the given voxel location). The null hypothesis in this case is that the group a subject belongs to has no influence on the value of Y. The greater the value of t, the greater the evidence that the null hypothesis is false.

Assuming that the data used in a t-test is drawn from a normal (gaussian) distribution and assuming the null hypothesis is true, the t-value obtained will be drawn from a t-distribution. For a small number of degrees of freedom, the t distribution is noticably flatter than the corresponding normal distribution. For a large number of degrees of freedom, the t-distribution approaches a normal distribution.

5.2.2 p-values

The p-value for a statistical result is the probability that the observed correlation would have arisen by chance if the null hypothesis were true. The smaller the p-value, the greater the evidence against the null hypothesis.

Assuming the data is normally distributed, and the null hypothesis is true, the p-value

for obtaining a t-statistic with magnitude $|T|$ greater than $|t|$ is given by

$$p(|T| > |t|) = \mathcal{B}\left(\frac{1}{1+t^2/\nu}; \frac{\nu}{2}, \frac{1}{2}\right) \tag{5.3}$$

where $\mathcal{B}(x; a, b) = \beta(x; a, b)/\beta(1; a, b)$ is the normalised incomplete beta function (expressed here in terms of the (un-normalised) incomplete beta function

$$\beta(x; a, b) = \int_0^x u^{a-1}(1-u)^{b-1}du. \tag{5.4}$$

The above p-value is for a two tailed t-test. For a single tailed test where the hypothesis specifies the direction of the test, the p-value is reduced by a factor of two:

$$p(T > t) = p(T < t) = \frac{1}{2}p(|T| > |t|). \tag{5.5}$$

The question arises as to where one draws the line in deciding if the evidence is of sufficient strength to reject the null hypothesis. There is no canonical choice for this, but as a convention, most journals will demand a p-value less than or equal to 0.05 before a result can be labeled 'statistically significant' and considered worthy of publication.

5.2.3 Linear regression

In the example from the previous section, we were looking at the relationship between a binary variable (gender) and a continuous variable (MR signal level for a specific region or voxel location). Often one instead wants to look at the relationship between two continuous variables such as age and MR signal level. Increase in one of the variables may be associated with an increase or decrease in the other variable. The strength of the association is measured using the Pearson product moment correlation coefficient r.

$$r = \frac{\mathrm{cov}(\vec{x}, \vec{y})}{s_x s_y} \tag{5.6}$$

where s_x and s_y are the standard deviations of x and y respectively and

$$\mathrm{cov}(\vec{x}, \vec{y}) = \frac{1}{n-1}\sum_{i=1}^{n}(x_i - \bar{x})(y_i - \bar{y}) \tag{5.7}$$

is the covariance of $\vec{x}$ and $\vec{y}$.

The related quantity r^2 is called the coefficient of determination. It can be interpreted

as the fraction of the variance accounted for by the linear fit. Thus $r^2 = 1$ implies that the graph of the data is a perfectly straight line and the value of one variable is completely determined from the value of the other variable. Regression analysis reduces to a standard two sample t-test when one of the variables is binary (has only two possible values). In this case, the r- and t-values are related through

$$\frac{t^2}{\nu} = \frac{r^2}{1-r^2}, \qquad\qquad r^2 = \frac{t^2/\nu}{1+t^2/\nu}, \tag{5.8}$$

where ν is the number of degrees of freedom (the number of data points minus the number of fit parameters). For a linear regression there are two fit parameters, a slope parameter and a baseline y-intercept value, and therefore the number of independent degrees of freedom is $\nu = n - 2$. Assuming that the data is drawn from a normal distribution, then by combining Eq. 5.8 and Eq. 5.3, one can derive a p-value from an r-value

$$p(R^2 > r^2) = \mathcal{B}\left(1 - r^2, \frac{\nu}{2}, \frac{1}{2}\right) \tag{5.9}$$

with

$$p(R > r) = p(R < r) = \frac{1}{2}p(R^2 > r^2). \tag{5.10}$$

5.2.4 Multivariate statistics and the General Linear Model

So far only the interactions between two a priori independent variables have been discussed, however in most real world applications, the experimental conditions cannot be precisely controlled and there will always be other external factors which may bias the outcome of the experiment. For instance when comparing MR signal between two groups, it may turn out that one group was significantly older than the other group, or that one group on average had significantly more education. In this case one would like to determine if these other differences could account for any observed differences. There are more general statistical tests such as multiple regression and analysis of covariance (ANCOVA) that can be applied to analyse cases such as this. An elegant formalism which incorporates these tests is the General Linear Model (GLM).

In the GLM, the values of the independent variable Y are fitted by a linear equation

$$y = X\beta + \varepsilon \tag{5.11}$$

Where β is a column vector of model parameters determined by a least squares fit and X is a matrix called the design matrix that incorporates all predictor variables. Each column of X

will contain some form of demographic data about the subjects such as age, gender, disease status, blood pressure or presence of a particular genetic polymorphism. The GLM can be used to isolate variance associated with uninteresting confounding variables, from variance associated with variables of interest. Examples are provided in the following section.

In our applications, y is an n dimensional vector of MR signal intensity measurements for n different subjects made at a particular voxel location. ε is an n dimensional vector containing the residual or 'error' component of the data (The component of the data which cannot be accounted for by the linear fit). Minimising the mean squared error gives us the condition

$$0 = \frac{\partial}{\partial\beta}\left(\varepsilon^T\varepsilon\right) = \frac{\partial}{\partial\beta}\Big((y - X\beta)^T(y - X\beta)\Big). \tag{5.12}$$

which has the solution

$$\beta = (X^TX)^{-1}X^Ty. \tag{5.13}$$

for the optimal β parameter fit to the data (X, y).[12]

Any null hypothesis that we may wish to test is specified by an r dimensional contrast vector c. For example if the null hypothesis is that there is no relationship between the variable y and the subject ages are in column 3 of the design matrix then the contrast vector c would be $(0, 0, 1, 0, \ldots)$ The resulting t-test statistic is calculated as

$$t = \frac{c \cdot \beta}{\sigma}, \tag{5.14}$$

with

$$\sigma^2 = \frac{\varepsilon^T\varepsilon}{N - r}c^T(X^TX)^{-1}c. \tag{5.15}$$

r being the rank of X. (Typically, r will be equal to the number of columns in the design matrix, however if some of the design matrix columns happen to be linearly dependent (when viewed as N-dimensional vectors), the design matrix is 'rank deficient' r is equal to the dimension of the span of these vectors which will be less than the number of columns.

Note that the right hand side of Eq. 5.14 is invariant under scalar multiplication $\mathbf{c} \mapsto \lambda\mathbf{c}$, therefore the overall scaling of a contrast vector makes no difference to the t-statistic. Only the direction of the contrast vector is significant.

[12]The quantity $(X^TX)^{-1}X^T$ is the Moore-Penrose pseudo inverse of X. The pseudo inverse is the closest one can get to having an inverse for a matrix X that is not square.

5.2.5 General Linear Model Examples

Examples of the study designs relevant to this analysis are provided in this section.

5.2.5.1 Two sample t-test with adjustment for age

Suppose the sample consists of N subjects and is divided up into two groups with J and $N - J$ members respectively. The design matrix is

$$X = \begin{pmatrix} 1 & 0 & a_1 \\ \vdots & \vdots & \vdots \\ 1 & 0 & a_j \\ 0 & 1 & a_{j+1} \\ \vdots & \vdots & \vdots \\ 0 & 1 & a_N \end{pmatrix} \tag{5.16}$$

where the $\{a_i\}$ are the ages of the subjects. The t-statistic expressing the statistical significance of any differences between the two groups is calculated using the contrast

$$c = \begin{pmatrix} 1 & -1 & 0 \end{pmatrix} \tag{5.17}$$

The corresponding t-statistic is then given by

$$t = \frac{c \cdot \beta}{\sqrt{\hat{\sigma}^2 c^T (X^T X)^{-1} c}} = \frac{\beta_1 - \beta_2}{\sqrt{\hat{\sigma}^2 \left(\frac{1}{n_1} + \frac{1}{n_2}\right)}} \tag{5.18}$$

where $\hat{\sigma}^2 = \varepsilon^T \varepsilon / (N - r)$. Notice the resemblance between Eq. 5.1 and Eq. 5.18.

5.2.5.2 One Sample Regression with Age

For this example, X is the same as for the previous section but the contrast is now

$$c = (0 \quad 0 \quad \pm 1). \tag{5.19}$$

5.2.5.3 Two Sample Regression (interaction with group design)

Here we allow independent regressions of age between two groups

$$X = \begin{pmatrix} 1 & 0 & a_1 & \bar{a} \\ \vdots & \vdots & \vdots & \vdots \\ 1 & 0 & a_{n_1} & \bar{a} \\ 0 & 1 & \bar{a} & a_{(n_1+1)} \\ \vdots & \vdots & \vdots & \vdots \\ 0 & 1 & \bar{a} & a_{(n_1+n_2)} \end{pmatrix} \tag{5.20}$$

To test the difference in the slopes of the regression between the two groups the contrast

$$c_- = \begin{pmatrix} 0 & 0 & 1 & -1 \end{pmatrix} \tag{5.21}$$

is used. $\bar{a}$ is normally taken to be the mean age of all subjects, however its actual value can be chosen arbitrarily, since a change in $\bar{a}$ can be compensated for by a change in β_1 and β_2 while leaving the predictions of the model unchanged.

5.3 Voxel based statistical tests for images

5.3.1 t statistic images

The output of an SPM analysis is a t-map consisting of a t-statistic value for each voxel in the brain. Usually one is looking for evidence that will refute the null hypothesis: that there are no systematic differences between the two groups, or more generally, that there are no significant correlations between a clinical variable and the image values at a particular voxel.

5.3.2 The Problem of Multiple Comparisons

There are hundreds of thousands of voxels in a typical brain image and therefore voxel based statistical analysis entails doing an enormous number of statistical comparisons simultaneously. To see how this complicates the analysis, suppose two sets of images are randomly generated, with values drawn from identical gaussian distribution so that the null hypothesis is true by construction. Suppose each image has one million voxels (this is roughly how many cubic millimetre voxels there are in an average sized human brain). If one imposes a p-value threshold of 0.05, then due to the large number of voxels, one can expect $0.05 \times 10^6 = 50\ 000$ false positive voxels! This shows that if one were to naively use the p-values derived from

the t statistic image we would be certain of reporting numerous false positive results. This is a manifestation of the problem of multiple comparisons. The chance of reporting a false positive increases with the number of statistical tests performed. It is therefore essential to apply a correction to the p-values when testing multiple hypotheses to allow for this.

5.3.3 The Bonferroni correction

One way to avoid the problem of multiple comparisons is to use the Bonferroni correction. The Bonferroni correction is applied by dividing the p-value threshold by the number of hypotheses tested and then only deeming results significant if they are below this new stricter threshold. Equivalently, the Bonferroni correction can be applied by multiplying each voxel p-value by the number of voxels tested to obtain a corrected p-value.

The Bonferroni correction greatly limits the power of studies which simultaneously test a large number of independent hypotheses.

To increase a study's power, it is often advantageous to choose a small number of null hypotheses that are considered most likely to be false, rather than testing an indiscriminately large number of hypotheses. On the other hand, sometimes one wants to test multiple hypotheses to allow the data to reveal previously unsuspected patterns.

The Bonferroni correction is only strictly necessary if the hypotheses being tested are a priori independent. In brain images there are typically correlations between the values of neighbouring voxels, in which case the Bonferroni correction is overly conservative and places an unnecessarily severe limitation on the statistical power of the analysis.

5.3.4 The False Discovery Rate

An alternative method less conservative than the Bonferroni correction, uses the notion of the false discovery rate (FDR). The FDR is the fraction of results that have been incorrectly reported as significant (or equivalently, the proportion of null hypotheses incorrectly rejected.) The rationale for using the FDR, is that in some circumstances, one may be willing to tolerate reporting some false positive results, provided the ratio of true positive voxels to false positive voxels is acceptably high.

Suppose we perform N voxel comparisons. If we then declare the k strongest results with uncorrected p-values $p_1, \ldots, p_k$ to all be significant. The expected false discovery rate, which we denote q_k, will then be bounded by

$$q_k \leq \frac{N}{k} \max(p_1, \ldots, p_k) \tag{5.22}$$

In the case of a single significant result, this q value is equal to the Bonferroni corrected p-value, however, if there is more than one result the q-value is in general smaller than the corresponding p-value thus giving increased sensitivity.

When looking at an image with many significant voxels, the false discovery rate gives one a sense of what fraction are spurious false positives. As of version 12, SPM provides q-values in addition to p-values for peak voxels.

5.3.5 Random field theory and cluster statistics

An alternative approach to the assessment of the statistical significance of VBSA involves assessing contiguous clusters of voxels with t value above a certain threshold, rather than considering each individual voxel in isolation. This approach can be motivated by the observation that if numerous neighbouring voxels have high t-values then the likelihood that the signal is a true positive is increased. Conversely if all the voxels with high t-values are scattered randomly throughout the image with little spatial correlation, then they are more likely to be false positives that have arisen due to noise.

In the cluster analysis approach, an uncorrected voxel threshold is first chosen and clusters of voxels with statistical significance that exceed the chosen threshold are enumerated. The significance of each *cluster* is then assessed by examining the likelihood that such a concentration of voxels with t-values above the chosen threshold could have arisen by chance.

This analysis is based on the mathematical subject of random field theory (RFT). Random field theory takes into account the topology of a cluster derived from a statistical image, as well as the size and smoothness of the underlying statistical image. To apply random field theory, one first defines a search region Ω (This usually consists of all brain voxels, perhaps excluding ventricular regions, but could be restricted to brain subregions, depending on the hypothesis being tested.) One must then choose a cluster forming threshold u. This is typically chosen to be an uncorrected voxel p-value of 0.001, but the choice is arbitrary.

The probability of a cluster arising by chance depends on the threshold u, the cluster topology, the volume of the search region Ω and the spatial smoothness of the random field.

5.3.5.1 Spatial smoothness and resolution elements

In order to quantify the spatial smoothness of imaging data, it is convenient to introduce the notion of a resolution element. The size of a resolution element is calculated by the determinant of the matrix of partial derivatives

$$\Lambda = \frac{\partial \tilde{\varepsilon}^T}{\partial x^i} \frac{\partial \tilde{\varepsilon}}{\partial x^j}. \tag{5.23}$$

Where $\tilde{\varepsilon} = \varepsilon/\sqrt{\varepsilon^T\varepsilon}$ are the standardised residuals. In practice, Λ is estimated by calculating finite differences between neighbouring voxels. In terms of full width half maximum[13](FWHM), the volume of a three dimensional resolution element is given by

$$v = \text{FWHM}_x \times \text{FWHM}_y \times \text{FWHM}_z. \tag{5.24}$$

In terms of the matrix Λ, v works out to

$$v = (4\ln 2)^{3/2}|\Lambda|^{-1/2}. \tag{5.25}$$

where $|\Lambda|$ is the determinant of Λ. The total number of resolution elements R is therefore given in terms of the volume $V(\Omega)$ of the search region Ω by

$$R = \frac{V}{v} = \frac{V|\Lambda|^{1/2}}{(4\ln 2)^{-3/2}}. \tag{5.26}$$

Random field theory analysis is often performed with the assumption that the resolution is the same everywhere so that the matrix Λ is calculated as the average over the whole analysis region Ω (this is known as the stationary approximation). To allow for image sets with non-homogeneous smoothing, the resel size can be calculated separately at each voxel to give more accurate estimates of statistical significance. In this work the non-stationary approach is used (Hayasaka et al. 2004).

5.3.5.2 Cluster analysis

Returning to the study of cluster significance, having chosen the threshold u, one then calculates the excursion set $A_u = \{x \in \Omega | T(x) \geq u\}$. In order to take into account the cluster topology, it is natural to study the Euler characteristic rather than the number of clusters. The Euler characteristic for a three dimensional region is given by

$$\chi(A_u) = \#\text{connected components} - \#\text{handles} + \#\text{hollows}. \tag{5.27}$$

For a high threshold, clusters are unlikely to have any handles or hollows and the expected Euler characteristic is almost identical to the expected number of clusters. For a general D-dimensional image with cluster forming threshold u, the expected Euler characteristic

[13]The FWHM is the most commonly used measure of spatial resolution in imaging science. It is suboptimal that it was used as the unit for resel size as it leads to the appearance of factors of $4\ln 2$ which could otherwise have been avoided.

d	$\rho_d(z)$
0	$(2\pi)^{-1/2}\int_z^\infty du\exp(-u^2/2)$
1	$(2\pi)^{-1}(4\ln 2)^{1/2}\exp(-z^2/2)$
2	$(2\pi)^{-3/2}(4\ln 2)z\exp(-z^2/2)$
3	$(2\pi)^{-2}(4\ln 2)^{3/2}(z^2-1)\exp(-z^2/2)$

Table 5.1: Euler characteristic density functions of dimension d for a Gaussian random field, normalised so that the coefficients L_i are in units of resolution elements.

density is of the form

$$E[\chi(A_u)] = \sum_{j=0}^{D} L_j(\Omega)\rho_j(u) \tag{5.28}$$

The $\rho_j(u)$ are Euler characteristic density functions. Their form is determined by the (assumed) statistical properties of the distribution from which the voxel values are drawn. Expressions for ρ_j for a gaussian random field are provided in Table 5.1. The analagous expressions for the t-statistic can be found in Table 2 of (Worsley et al. 2004).

The L_i are determined by the geometry of the three dimensional search volume Ω and are described in units of resolution elements as follows

- $L_3(\Omega)$ is the volume of Ω.
- $L_2(\Omega)$ is half the surface area of the boundary of Ω.
- $L_1(\Omega)$ is twice the average caliper diameter (assuming Ω is convex).
- $L_0(\Omega)$ is the euler characteristic of Ω.

Over a three dimensional search region containing a large number of voxels, the $D = 3$ term of the sum in Eq.5.28 will dominate. For a Gaussian field (Recall that for many subjects, a t-distribution is very close to a z-distribution), the expected Euler characteristic is

$$E[\chi(A_u)] = (2\pi)^{-2}V(\Omega)|\Lambda|^{1/2}(u^2-1)\exp(-u^2/2) \tag{5.29}$$

Note that the product $V|\Lambda|^{1/2}$ is dimensionless. It can be calculated using units of voxels or millimetres, so long as the same units are used for V and Λ.

5.3.6 Cluster extent

The above considerations only take into account the number of clusters, however it is also desirable to take into account cluster size (number of resels in the cluster) when assessing

cluster significance. For a chosen threshold, the total number of resels N with t-value above the threshold, the number of clusters m and the number of resels n_i in each of the clusters are related through

$$N = \sum_{i=1}^{m} n_i = m\bar{n}, \tag{5.30}$$

where $\bar{n}$ is the average cluster size. For random fields, the set of values $\{n_i^{D/2}\}$ follow an approximately exponential distribution and for high thresholds, the values of m are drawn from an approximately poisson distribution. With these approximations, the probability of finding a cluster with k or more resels is (Friston et al. 1994)

$$P(n \geq k) \approx e^{-\beta k^{2/D}} \tag{5.31}$$

with

$$\beta = [\Gamma(D/2+1)E[m]/E[N]^{2/D} \tag{5.32}$$

Where $E[m]$ is the expected number of clusters calculated using Eq. 5.29 and $E[N]$ is the expected number of resels above the threshold, given by the product of the cluster forming p-value threshold used and the number of resels. The probability of getting one or more clusters with size $\geq k$ is then given by

$$P(n_{\mathbf{max}} \geq k) = 1 - \exp\left(-E[m]e^{-\beta k^{2/D}}\right) \tag{5.33}$$

where $E[m]$ is the expected number of clusters. The cluster statistics produced by SPM are based on this formula.

5.3.7 The role of the cluster forming threshold

Technically, a significant cluster p only means that the null hypothesis is false (to the nominated significance level) for some subregion within the cluster. This actual region of abnormality could be as small as a single voxel, so it does not follow that the whole cluster is abnormal.

In choosing a cluster forming threshold there is a trade of: Choosing a low threshold gives better sensitivity (more chance of demonstrating there is an abnormality), but poorer spatial specificity (the significant activation could be anywhere within a large cluster). A higher threshold will reduce the cluster sizes bringing better spatial specificity at the expense of decreased sensitivity.

5.3.8 Cluster mass and the threshold free cluster enhancement

A drawback of the cluster statistic method is the results can be quite sensitive to the arbitrarily chosen cluster forming threshold. Two related methods, the cluster mass of (Bullmore et al. 1999) and the threshold free cluster enhancement (TFCE) method of (Smith & Nichols 2009) simultaneously take into account a cluster's height and extent in gauging it's significance have been developed. Both these measures are based on an integral of the form

$$\mathcal{I}(E, H; h_0) = \int_{h_0}^{h_{\text{peak}}} e(h)^E h^H dh \tag{5.34}$$

where h is cluster height and e is cluster extent. h_0 is typically zero. In the special case $(E = 1, H = 0)$ this reduces to the cluster mass of (Bullmore et al. 1999). The recommended values that lead to the TFCE of (Smith & Nichols 2009) are $(E = 0.5, H = 2)$. (Smith & Nichols 2009) justify their choice of these values using empirical simulations and also provide a theoretical argument based on random field theory suggesting the integrand should be approximately

$$\left(\frac{E}{H^3 - H}\right)^{2/3} \tag{5.35}$$

which for large H, is approximated by $(E = \frac{2}{3}, H = 2)$.

The TFCE image or the cluster mass can be used as the result image for non-parametric statistical analysis (discussed in the following section) in place of the t map image.

5.4 Non Parametric Statistical Analysis

The general linear model is limited by the assumption that at each voxel, the image intensities are normally distributed across subjects.

More precisely, for parametric statistical methods to be valid, the error terms should be independent, and identically distributed (i.i.d.). That means the residual error terms ϵ_i for each subject are each drawn from the same distribution with the same variance parameters. For the parametric methods of the previous section, this distribution is assumed to be a normal distribution.

Nonparametric permutation methods allow the assumption of normality to be relaxed. Furthermore, they allow for a weakening of the i.i.d. assumption to the assumption that the ϵ_i are 'exchangeable random variables.' Roughly speaking, a distribution is exchangeable if the operation of exchanging labels of the data does not change the resulting error distribution.

Non parametric statistical analyses are performed by randomly permuting the subject indices and recomputing the statistic and counting how many random permutations give

results comparable in strength to the observed results for the comparison of interest.

After repeating the analysis for J permutations, the p value is given by

$$p(T_{\text{thld}}) = \frac{1}{J}\sum_{j=0}^{J} I[T_j^* \geq T_{\text{thld}}] \tag{5.36}$$

where I is the indicator function (I[true]=1, I[false] = 0). Note that the original unpermutated data is included in the sum, so for J permutations, the minimum possible p-value that can be obtained is $1/J$. Cluster inference is treated similarly, with cluster size or Euler characteristic replacing the T_j.

Non parametric tests have two main drawbacks: They require a great deal more computational resources than parametric approaches and they have less statistical power especially when the sample size is small.

5.5 Normalisation of Signal Intensity

5.5.1 The need to Adjust for Global Intensity

MRI signal levels are known to vary due to drift in the performance of the scanner components and subtle variations in the scanner environment. These variations effect the global image intensities and make direct statistical comparisons of raw voxel values from different images problematic. Similar issues occur in the statistical comparison of nuclear medicine images (in both Positron Emission Tomography (PET) and Single Photon Emission Computed Tomography (SPECT), where image intensity is influenced by confounding factors such as the amount of radio-tracer injected and the patient body size and body composition. In SPECT, an age dependent effect has been demonstrated in the raw global intensity values (Barnden & Behin-Ain 2004). In such cases, in order to make meaningful comparisons, it is necessary to apply some form of intensity normalisation, whereby the intensity of each image is adjusted independently so that the image intensities become more comparable across subjects. A separate intensity normalisation map is computed for each image and is applied uniformly to all voxels in that image.

5.5.2 Intensity normalisation transformations

As with spatial normalisation, there are various classes of intensity normalisation that may be considered, both nonlinear and linear. The most general intensity normalisation is a

transformation of the form

$$y_{i,x} \mapsto \tilde{y}_{i,x} = \mathcal{Z}_i(y_{i,x})y_{i,x} + c_i \tag{5.37}$$

where $y_{i,x}$ is the voxel value in the ith image at voxel location x. In general the functions $\mathcal{Z}_i(y)$ are independent of the voxel location x but a priori could be any positive[14] function of the voxel value y; In practice, one usually works with the linear case where the $\mathcal{Z}_i$ are constant multiplicative factors that do not depend on y,

$$\mathcal{Z}_i(y) = Z_i. \tag{5.38}$$

Furthermore, one usually sets the c_i to zero since there is not typically any additive error to adjust for in MR images and therefore the transformations should be constrained so that a voxel value that starts out zero remains zero. With these two simplifications, Eq. 5.37 reduces to

$$\tilde{y}_{i,x} = Z_i y_{i,x}. \tag{5.39}$$

All intensity normalisation used in this work are linear, with no additive adjustment and are therefore of the form Eq. 5.39.

5.5.3 Components of an Intensity Normalisation Algorithm

An intensity normalisation algorithm is specified by the following two components: A reference region and a formula for computing the normalisation map from the distribution of voxel values in the reference region.

1. **Reference region**
   A reference region specifies the voxel values from which the intensity normalisation is computed. The reference region may be the whole brain, or a subregion of the brain that is assumed to be largely unaffected by the disease or clinical variable being studied. For example in Alzheimer's disease, the cerebellum is sometimes used as a reference region as it is one of the brain regions that is least affected by the disease. If global systematic pathology is suspected, one may choose a reference region outside of the brain such as the eyeballs or temporalis muscles, however as these structures tend to be on the periphery of the brain regions, they are more prone to distortion and systematic errors and therefore may not be representative of the system response nearer to the centre of the field of view.

[14] The positivity condition is needed to ensure the mapping $y \mapsto \tilde{y}$ is one to one.

2. **Formula for the Normalisation Function**

   A formula is applied to compute an intensity normalisation map for an image based on the distribution of voxel intensity values within the reference region. For the linear case this typically involves specifying an aggregate intensity function such as the mean, median or histogram peak intensity, that provides a single aggregate intensity value A for each brain image. In the linear case, the multiplicative normalization factors are then computed as $Z_i = KA_i^{-1}$ so that by construction, the intensity normalized images have the same intensity measure value (The arbitrary constant K) for the reference region.[15] For a nonlinear algorithm this might involve computing a nonlinear map which matches the histogram of voxel values from the reference region with the histogram from the reference region for the template image.

5.5.4 Intensity Normalisation Algorithm Examples

The simplest intensity algorithm uses the whole brain as the reference region and the mean as the global intensity measure. This is a suitable choice if one is expecting only small regions of abnormality, with most brain areas unaffected by any disease or pathology.

To decrease the influence of pathological outlier voxels on the global value, the peak in the intensity histogram can be used instead of the mean. Another variation along these lines, that works even when the gray and white matter peaks are difficult to distinguish is to use the leading or trailing edges of the histogram rather than the peak (Barnden et al. 2008).

When the histogram contains values for different tissues having quite different signal intensities, such as gray matter and white matter, the histogram peak is largely determined by the most common tissue type.

5.5.5 Implementation of Linear Intensity Normalisation

Once the global scale factors have been derived, there are two ways of incorporating them into the statistical analysis, referred to as proportional scaling and ANCOVA scaling respectively.

In proportional scaling, the images are rescaled so that each subject's image has the same prescribed value in the reference region. In ANCOVA scaling, the images are left unchanged and the whole brain means are included in the statistical design as a nuisance covariate.

Although ANCOVA and proportional scaling are based on the same global values, they typically yield very similar but non-identical results. Differences between ANCOVA and proportional scaling arise for the following reasons:

[15] This is the proportional scaling implementation of intensity normalisation. There is also an alternative 'ANCOVA' implementation of intensity normalisation described in Subsection 5.5.5.

1. For proportional scaling, the residual variance is adjusted in proportion to the rescaling factor. This makes proportional scaling well suited to variance associated with signal variations associated with changes in sensitivity of the apparatus. With the ANCOVA implementation of global scaling, the variance is unchanged, which may be more appropriate for voxel based morphometry.

2. In the ANCOVA model, there is an extra fit parameter: information characterising the raw global intensities is still present in the model. If the raw intensity values are not severely affected by noise, this may lead to a better model fit and therefore give different results.

3. If there is substantial correlation between the covariate of interest and the global value, adjustment using ANCOVA must be performed with caution: as effectively the model is only regressing against the components of the covariate of interest vector which are orthogonal to the vector associated with the global signal variations which may result in biases and artifactual results from the voxel-wise statistical analysis.

5.5.6 Voxel Based Iterative Sensitivity Scaling

Voxel based iterative sensitivity (VBIS) scaling (Abbott et al. 2009) is a more refined data driven intensity normalisation technique, in which the reference region is determined by the results of a preliminary voxel based statistical analysis.

The VBIS method consists of the following steps:

1. An initial analysis is done using proportional scaling to the brain mean.

2. A coefficient of variation (cov) image is computed. via the equation[16]

$$\begin{aligned} \text{cov image} &= \frac{\text{standard deviation image}}{\text{local mean image}} \\ &= \frac{\text{contrast image}}{t\text{-statistic image} \times \text{local mean image}} \end{aligned} \tag{5.40}$$

   The local mean is the voxel value predicted by the GLM with all covariates set to their mean values.

[16](Abbott et al. 2009) use a closely related quantity which they denote as C%LM which is a constant multiple of the cov image. The extra multiplicative factor makes no difference to the mask derived in step 3 and so does not influence the final results.

3. Given that the voxels with lower cov have less variability across subjects and are therefore less likely to be affected by spatial normalisation errors, the intensity normalisation factors for VBIS are computed using only the voxels with cov below the median.

4. The statistical analysis is re-run replacing the whole brain mean values with the means from the VBIS region.

5. One then has the option of recomputing the mean in a further iteration which excludes those voxels that lie in statistically significant clusters for either positive or negative contrasts. Regions where there are significant differences between groups, or more generally, significant correlations with a covariate of interest are thereby prevented from influencing the scaling factors.

In (Abbott et al. 2009), it was found that VBIS yielded more significant results than basic whole brain mean scaling for T2w images. The main drawback of VBIS is the added complexity needed to perform the analysis.

While the above algorithms use the mean as the aggregate value, the method can be applied similarly with the mean replaced by another aggregate intensity measure such as the median or histogram intensity peak location (mode).

5.5.7 Global effects in Voxel Based Morphometry

In voxel based morphometry, one is interested in brain volumes of sub regions relative to the total brain volume. Here there are several options to adjust for global volume: One normally uses the total intra-cranial volume (TIV) defined as the combined volume of gray matter, white matter and cerebrospinal fluid. The TIV remains constant through adulthood. However, for age related studies, it is already very well established that both gray and white mater volume decreases steadily with age throughout the brain (Peelle et al. 2012). A more interesting question is which regions shrink unusually fast or slow relative to the overall trend. To assess this one may use the total gray matter volume (when analysing the gray matter images) and the total white matter volume (when analysing the white mater images).

As for T1w and T2w, one has the choice of using proportional scaling, or feeding in the global levels as a covariate (ANCOVA scaling).

5.5.8 Interpretation of results when using intensity normalisation

When intensity normalisation has been used one must take care in interpreting the results as they describe behaviour relative to some particular reference tissue and therefore may

not correspond directly to absolute changes. While intensity normalisation is effective in removing noise associated with global changes in the scanner environment it also has the potential to remove some of the signal. If the disease or phenomena being studied is linked to widely distributed diffuse or global changes that are uniform across the brain or reference region, such changes will not be detectable with this type of VBSA analysis. However, provided one is looking for localised changes that are not expected to greatly effect the intensity values in the reference (or can be prevented from doing so by a second iteration with VBIS), then Voxel Based Statistical Analysis with intensity normalisation will be useful. Importantly, in such scenarios, intensity normalisation methods should weaken statistical inference and not introduce false positives.

Chapter 6

Methods: Data, Preprocessing and Statistical Analysis

6.1 Introduction

In this chapter the methods used to carry out the voxel based statistical analysis are described in detail. Section 6.2 describes the image data used. In performing VBSA there are numerous settings that need to be chosen including the intensity and spatial normalisation algorithms, masking to exclude non-brain tissue from the analysis, and the choice of voxel size and smoothing parameters that determine the trade off between statistical sensitivity and resolution. The spatial normalisation and segmentation used are described in Section 6.3. The statistical analysis, including the intensity normalisation algorithms used and the voxel and cluster significance thresholds are described in Section 6.4. Finally, in Section 6.4.6 multiple comparison correction factors are calculated to allow for the multiple image types and contrasts being examined.

6.2 IXI-152 dataset and acquisition parameters

6.2.1 The full IXI dataset

The IXI dataset is a freely available MRI dataset which can be downloaded online [http://brain-development.org/ixi-dataset/, accessed 6/1/2016]. Anonymised images were supplied in NIFTI format with an accompanying spreadsheet containing demographic data and text files specifying the acquisition parameters. The full dataset includes over 500 normal subjects scanned on one of three different MRI scanners affiliated with University College London. The scanners included two 1.5 T scanners and one 3 T scanner. Imaging protocols included

a T1 ultrafast gradient echo sequence and a T2 weighted fast spin echo sequence. Proton density, diffusion tensor (15 directions) and magnetic resonance angiography images were also available for some subjects but are not examined in this work.

Not all scans were available for all subjects. Of the 593 subjects listed in the database, 519 subjects had T1 images, 524 had T2 images, 214 had proton density images and 397 had diffusion tensor images.

6.2.2 The IXI-152 dataset and acquisition parameters

To ensure the scan conditions were as uniform as possible, the data used in this analysis is restricted to data collected from a single scanner. As the scanner with highest magnetic field is expected to have a higher signal to noise ratio, the data from the 3T Philips Intera scanner at Hammersmith Hospital was chosen for this analysis. Data from the remaining two 1.5T scanners may be used in future work to compare with the results reported here. 153 of the subjects from the 3T scanner had both T1-weighted and T2-weighted images, however an additional subject was excluded because the T2w scan was performed with a much larger slice thickness than the other images and therefore had very poor z resolution. This left 152 subjects, which will be referred to here as the IXI-152 data set. The magnetic resonance acquisition parameters for the IXI-152 data set are listed in Table 6.1. The slices were acquired axially with a pixel size of 0.9375 mm and a spacing of 1.2 mm between slices meaning that the resolution was slightly poorer along the z direction.

The T1w images were obtained using a Turbo Field Echo (TFE) pulse sequence, an ultra fast gradient echo sequence with a very short flip angle and repetition time (see Subsection 2.5.3). The T2 weighted images were acquired using a fast spin echo sequence (see Subsection 2.5.2.2).

6.3 Preprocessing Procedure

6.3.1 Linear co-registration of T2w images to the T1w images

Rigid co-registration of the T2w images to the T1w images was performed using SPM12 with mutual information as the similarity metric. An example of cross-sections of co-registered T1w and T2w images is shown in Fig. 6.1.

Weighting	T1 weighted	T2 weighted
Sequence name	Turbo Field Echo	Fast Spin Echo
Repetition Time	9.60000038146972	5725.79052734375
Echo Time	4.60269975662231	100.0
Flip Angle (degrees)	8.0	90.0
Number of Phase Encoding Steps	208	187
Echo Train Length	208	16
Reconstruction Diameter	240.0	240.0
Acquisition Matrix	208 × 208	192 × 187
Pixel size (mm)	0.9375 × 0.9375	0.9375 × 0.9375
slice thickness (mm)	1.2	1.2
slice orientation	transaxial	transaxial

Table 6.1: Acquisition settings for the IXI-152 data set.

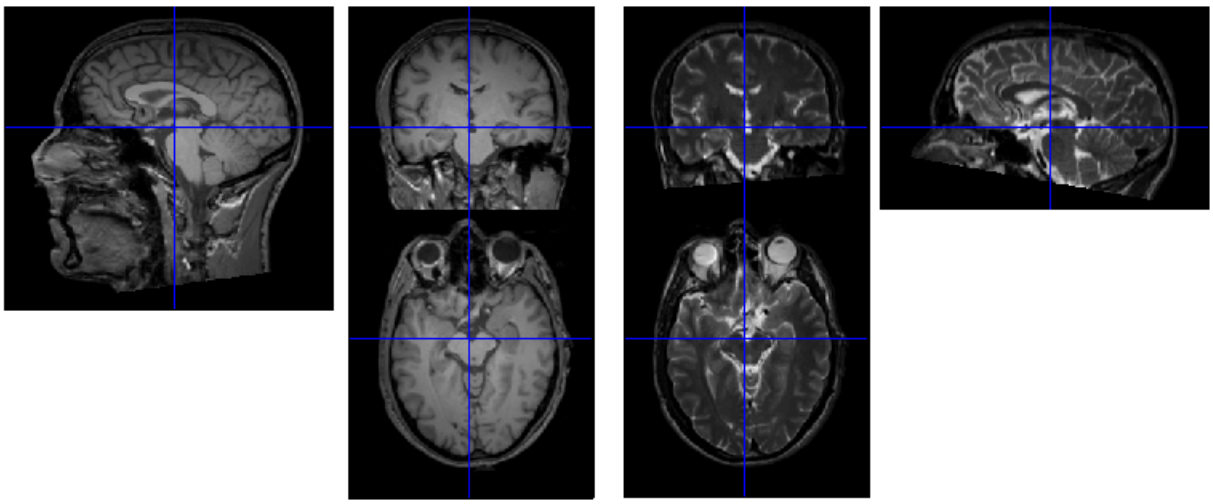

Figure 6.1: Coregistration of T1 (left) and T2w (right) brain images for a sample subject taken from the IXI-152 data set.

6.3.2 Segmentation and Bias Correction

The T1 weighted images were segmented into gray matter, white matter and cerebro-spinal-fluid compartments using SPM12's segmentation algorithm (with default settings). Segmented images were written to native space. Bias correction for magnetic field inhomogeneity computed during the segmentation was also applied to the T1w images. Bias correction was not applied to the T2w images as spin echo sequences are intrinsically resistant to such effects.

6.3.3 Nonlinear spatial normalisation

Although in the course of comparing each subject image to a prior tissue probability template image, the segmentation makes uses of a built in normalisation, other better performing spatial normalisation algorithms, as evaluated in (Klein et al. 2009), were used to perform the final spatial normalisation.

Two separate normalisation algorithms were trialled: SPM's DARTEL (diffeomorphic Anatomical Registration Through Exponentiated Lie Algebra) (Ashburner 2007) and ANTs (Advanced normalisation Tools') Symmetric Normalisation (SyN) algorithm (Avants et al. 2008). SyN was applied directly to the T1w images and was therefore completely independent of the segmentation, while The DARTEL spatial normalisation was based on the segmented gray and white images.[17] The SyN algorithm matches the entire image so that regions outside the brain contribute to the calculation of the normalisation map, while the DARTEL registration is only guided by tissues within the brain.

6.3.3.1 DARTEL spatial normalisation procedure

Following rigid coregistration, nonlinear spatial normalisation to standard MNI space was computed for each subject using SPM's DARTEL toolbox (Ashburner 2007). DARTEL has the option of computing a template specific to the dataset analysed during the process, hoewever in this work an existing fixed template was used: the MNI152 template supplied with the computational anatomy toolbox (Gaser & Dahnke 2012), with 1.5mm isotropic voxels. All other DARTEL settings were left on the default settings.

The spatial normalisation maps were applied to the four image types: T1w, T2w, gray matter and white matter. For the gray and white matter images, the transformation was applied with modulation. Modulation adjusts the output voxel intensities by the Jacobian of the deformation field such that the volume is preserved (see Subsection 4.4.1). No modulation was applied to the T1w or T2w images.

[17] DARTEL is not designed to be applied directly to raw T1w images.

6.3.3.2 ANTs nonlinear spatial normalisation

A separate spatial normalisation based directly on the T1w images was performed using advanced normalisation tools (ANTs) symmetric normalisation (SyN) algorithm. The mutual information similarity metric was used for the initial linear registration. The cross correlation similarity metric with a window size of 6 voxels was used for the final nonlinear registration stage. The 1.5 mm T1 version of the MNI152 template supplied with the computational anatomy toolbox was used as the template/target image.

6.3.4 Assessment of spatial normalisation quality

The performance of the two spatial normalisation algorithms was compared by calculating the normalised mutual information for all pairs of masked T1w images that were normalised with the same algorithm. The mean normalised mutual information (NMI) across all image pairs was computed separately for the ANTs and DARTEL algorithms.

The algorithm with the larger mean NMI was chosen for use in the subsequent voxel based statistical analysis. The spatial normalisation algorithm with the highest mean normalised mutual information between subjects was used for the subsequent statistical analysis.

6.4 Voxel based statistical analysis

6.4.1 Masking

6.4.1.1 The need for masking

To exclude non-brain tissue from the analysis, the images were masked. Masking refers to excluding all voxels outside a predefined 'mask' region. In VBSA there are two reasons for masking:

1. to prevent the appearance of spurious results arising from imperfect spatial normalisation, and

2. to limit the number of voxels in the search region, thus reducing the severity of the multiple comparison correction required and providing greater sensitivity.

In this work the masking was applied in two stages. An initial mask was applied to exclude non brain regions and additional masking was applied based on the image intensities to exclude regions of cerebrospinal fluid from the analysis.

6.4.1.2 Initial Masking

The brain mask supplied with SPM was considered too loose, especially around the pons, with the potential to lead to spurious results there. A tighter brain mask was therefore derived from the ICBM template. The mask was defined by the nonzero portion of the from the symmetric ICBM template (The McConnell Brain Imaging Centre 2009, Lancaster et al. 2007) and applied to both the T1 and T2 weighted images.

6.4.1.3 Threshold masking for T1 images

SPM includes a 'threshold masking option' whereby voxels are excluded from the statistical analysis if any of the subjects have a voxel value below a nominated threshold. The threshold can be set at a constant absolute value or can be set in a voxel dependent fashion, such that the threshold is a fixed fraction of the mean intensity across all subjects at each voxel.

The SPM default value for the masking, a relative threshold of 0.8 times the sample mean was trialled initially. Although this was successful in excluding spurious results, for the T1w images, it excluded nearly all cortical gray matter from the analysis. This is not surprising, given that this threshold value is geared towards the analysis of PET and VBM images. In order to allow the analysis to also be sensitive to gray matter changes, the threshold was relaxed to half the population mean as in the author's previous collaborations (Barnden et al. 2011), (Barnden et al. 2015), (Barnden et al. 2016).

6.4.1.4 Cerebro spinal fluid masking for T2 images

Because CSF regions are brighter than brain tissue on T2w, an upper threshold to exclude these regions was applied instead of the usual lower threshold. This was implemented by setting all voxels with intensity greater than 1.25 times the histogram peak T2 value to zero prior to the statistical analysis. No lower threshold masking was applied for the T2w image analysis.

6.4.1.5 Threshold masking for VBM analysis

An absolute threshold of 0.25 was used for the VBM statistical analysis.

6.4.2 Global Intensity Normalisation

Recall from Section 5.5 that a linear intensity normalisation algorithm is specified by a reference region and a function to compute an aggregate intensity value from the distribution of voxel values for the reference region. The intensity normalisation can then be implemented

either by dividing the images by the aggregate intensity measure (proportional scaling) or by including the vector of intensity values in the general linear model statistical design as a nuisance covariate (ANCOVA scaling). As one of the goals of this work is to examine the effect of the choice of intensity normalisation algorithm on the T1w and T2w VBSA results, the analysis of the T1w and T2w was repeated for three different intensity normalisation algorithms, as summarised below and in Table 6.4.2. The three intensity normalisation algorithms used were:

1. **whole brain mean intensity normalisation.** The mean intensity across the whole brain region (defined by the 'initial mask' specified in Section 6.4.1.2) was computed separately for each of the 304 T1w and T2w spatially normalised images.

2. **Voxel Based Iterative Sensitivity** VBIS mean intensity normalisation The VBIS region was determined using MATLAB based software developed in-house which analysed the statistical parametric maps from a comparison of males and females using SPM's default proportional scaling. Recall from Subsection 5.5.6 the VBIS region is the half of the brain where the inter-subject variance is less than the median for the whole brain. VBIS regions were calculated separately for T1w and T2w images and the mean for each subject in the appropriate VBIS region was then calculated for the T1w and T2w images respectively. Fig. 6.2 shows, for T1w and T2w, images of all voxels analysed and the VBIS reference region used to compute global values for intensity normalization. In both cases, the VBIS reference region shows voxels were excluded in gray matter and at the edges of lateral ventricles. That is, these areas showed greater population variability relative to the whole brain mean than white matter.

3. **Intensity histogram peak normalisation**. The peak location of the image intensity histogram were computed using MATLAB software developed in-house making use of a freely available third party peak finding algorithm (Yoder 2011). Histograms for T1w and T2w images for a sample subject are shown in Fig. 6.3. It was verified through visual inspection that the highest peak corresponded to the white matter peak for all subjects. The peak locations is therefore expected to correlate well with the the values derived from fits to the leading (trailing) slope of the T2w (T1w) histograms using the method of (Barnden et al. 2008).

   The ratio of peak white matter height to peak gray matter height was higher in these images compared to (Barnden et al. 2008) which analysed spin-echo T1w instead of the higher contrast gradient-recalled-echo T1w here.

Table 6.2: Intensity normalisation algorithms examined in this work. Abbreviations: GMV -Gray Matter Volume, WMV -White Matter Volume, loc. -location. ANCOVA -Analysis of co-variance.

Modalities	**Name**	**Ref. Region**	**intensity measure**	**Implementation**
T1w, T2w	peak	whole brain	histogram peak loc.	proportional
T1w, T2w	mean	whole brain	mean voxel value	proportional
T1w, T2w	VBIS	VBIS region	mean voxel value	proportional
GMV	total WMV	whole brain	total GMV	ANCOVA
WMV	total GMV	whole brain	total GMV	ANCOVA

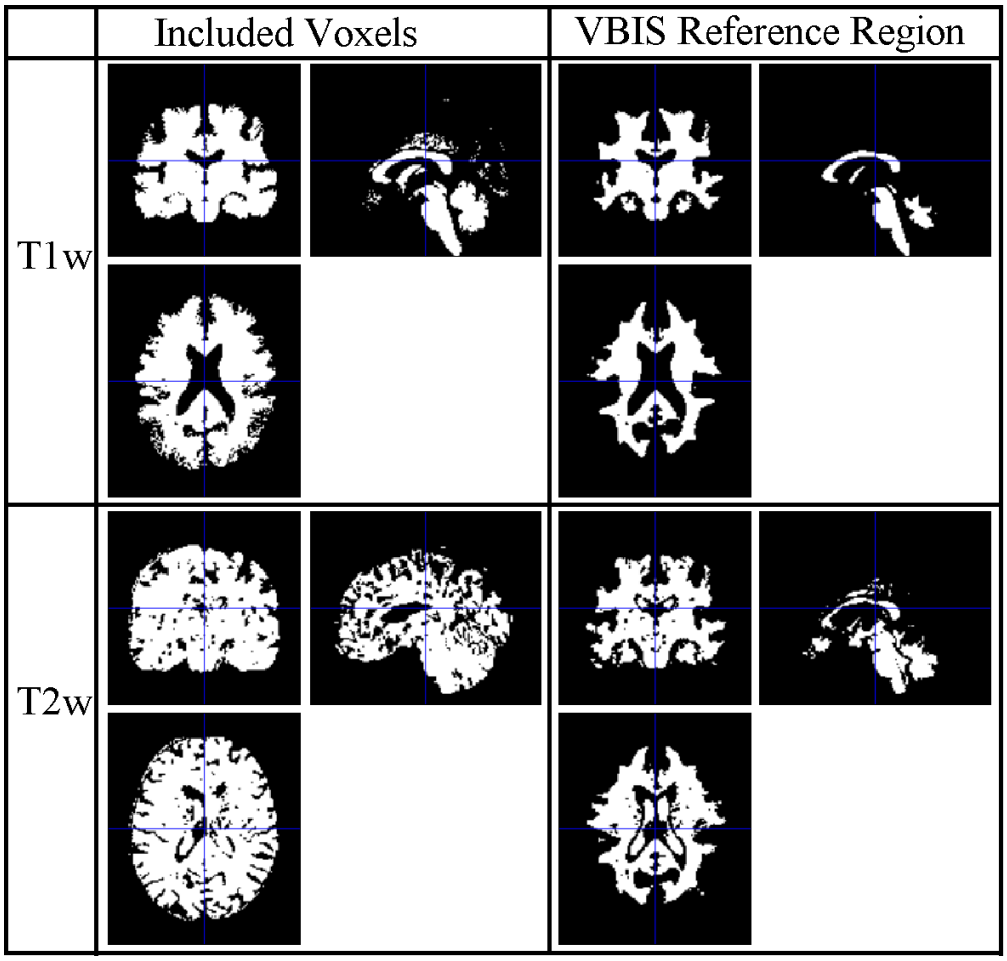

Figure 6.2: Orthogonal sections showing brain voxels included in the whole brain mean statistical analysis (left) and the corresponding VBIS reference regions (right), for the T1w (top row) and T2w (bottom row) analysis. The VBIS reference region has half the number of voxels.

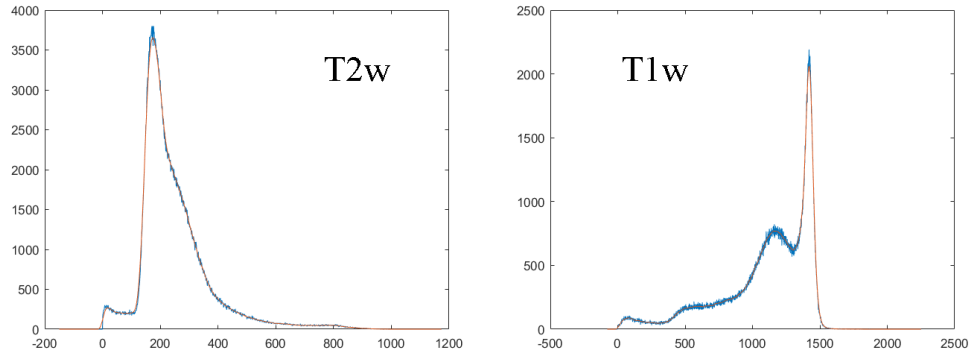

Figure 6.3: Sample Intensity histograms from one of the IXI152 subjects. The curves in orange are the smoothed version of the raw histogram data(blue). For both T2w and T1w histograms,the histogram peak locations correspond to the most common white matter voxel values. In the T1w histogram a second gray matter peak is visible. Units are arbitrary.

Proportional scaling was used for all T1w and T2w intensity normalisations and was implemented outside of SPM by dividing the images by the respective global intensity measures and multiplying by 1000 using in house MATLAB scripts based on SPM's routines for reading and writing image files. Thus, by construction, the intensity normalised images all had an aggregate intensity (mean or histogram peak location) equal to 1000 in their respective reference regions. (ANCOVA was used for the VBM analysis, see Subsection 6.4.4.)

6.4.3 Statistical Analysis of the T1w and T2w image sets

Voxel by voxel general linear model fits were computed using SPM12 with age and gender as covariates. t-statistic images were then generated for both age and gender contrasts.

6.4.4 Voxel based Morphometry

Total gray and white matter tissue volumes were computed for each subject by summing up the respective gray and white matter images. No lower threshold was applied when summing the images. Intra-cranial volumes were computed by summing the (modulated) gray matter, white matter and cerebro-spinal fluid images and then summing over all voxels.

Voxel by voxel general linear model fits were computed separately for white matter volume (WMV) and gray matter volume (GMV) images with age and gender both included as covariates. Adjustment for global differences was implemented by total gray matter volume (resp. total white matter volume) as the respective global variables using the ANCOVA scaling option in the factorial design specification. The choice of the ANCOVA implementation of global intensity in VBM was influenced by the results of (Peelle et al. 2012) who found

that the ANCOVA model derived from half of their data set was better able to predict age related effects in the other half of their dataset.

As for the T1w and T2w analysis, t-statistic images were generated for age and gender contrasts using SPM12.

6.4.5 Cluster Analysis

An uncorrected cluster forming voxel P value threshold of 0.001 was used for cluster formation. Cluster significance was evaluated with correction for non-stationary smoothness.[18]

The Xjview toolbox (Cui et al. 2016) was used to assess cluster location with the aid of the aal (Tzourio-Mazoyer et al. 2002) and Talairach daemon (Lancaster et al. 2000) brain atlases and the John Hopkins University white matter atlas (Mori et al. 2005).

6.4.6 Correction for multiple comparisons

While SPM corrects for multiple voxel comparisons, additional corrections are applied to account for the fact that multiple image contrasts($\pm$age, F>M, F<M), multiple image modalities (T1w, T2w, GMV, WMV) and multiple intensity normalisation algorithms were all considered.

The number of distinct voxel based statistical analyses performed involving just the T1w and T2w MR images, N_{MR}, is found by multiplying the number of contrasts (4:+age, $-$age, F>M, F<M), by the number of modalities (2:T1w, T2w) and the number of intensity normalisation algorithms (3: whole brain mean, VBIS region mean, histogram peak) giving a total of $N_{\mathrm{MR}} = 4 \times 2 \times 3 = 24$ voxel based statistical analyses of the MR images. The number VBM analysis, $N_{\mathrm{VBM}} = 8$ was a third of this as only one intensity normalisation algorithm was used for each modality. The total number of comparisons was therefore

$$N = N_{\mathrm{MR}} + N_{\mathrm{VBM}} = 24 + 8 = 32 \tag{6.1}$$

Applying this Bonferroni correction factor, the p-value threshold for a corrected significance level of 0.05 becomes $0.05/N = 0.0016$.

[18] This was implemented by creating a file spm_my_defaults.m in the MATLAB path consisting of the following lines:

```
global defaults
defaults.stats.rft.nonstat=1
```

Chapter 7

Results

7.1 Chapter outline

This chapter presents the results obtained from the analysis described in the previous chapter. Section 7.2 describes the demographics of the group from which the images were obtained. Section 7.3 discusses the performance of the two spatial normalisation algorithms and reveals which one was chosen to use for the subsequent statistical analysis. In Subsection 7.4.1 the degree to which the intensity normalisation algorithm chosen affected the results is broadly discussed.

The remainder of the chapter is devoted to presenting the results of the voxel based statistical analysis. The results are stratified first by covariate of interest (age, gender), and then by imaging modality (in the order T1w, T2w, GMV, WMV). Section 7.5. describes age related changes. Section 7.6. covers gender differences. Recall that for all T1w and T2w analyses, intensity normalisation was implemented using proportional scaling. For the VBM analysis (applied to the GMV and WMV image sets), the global intensity normalisation was implemented by adding the total GMV or total white matter volume respectively as ANCOVA nuisance covariates.

7.2 Demographics

The IXI-152 data set consists of 64 Male and 88 Female subjects. The age distribution is plotted in fig. 7.1. Ages ranged from 20.2 to 81.9 years. The mean age at time of scanning was 46.0 years for males, 50.5 years for females and 48.6 years across all subjects. The intra-cranial volumes for the male and female groups were 1.49 ± 0.10 and 1.32 ± 0.12 Litres respectively, a statistically significant difference ($p < 10^{-16}$).

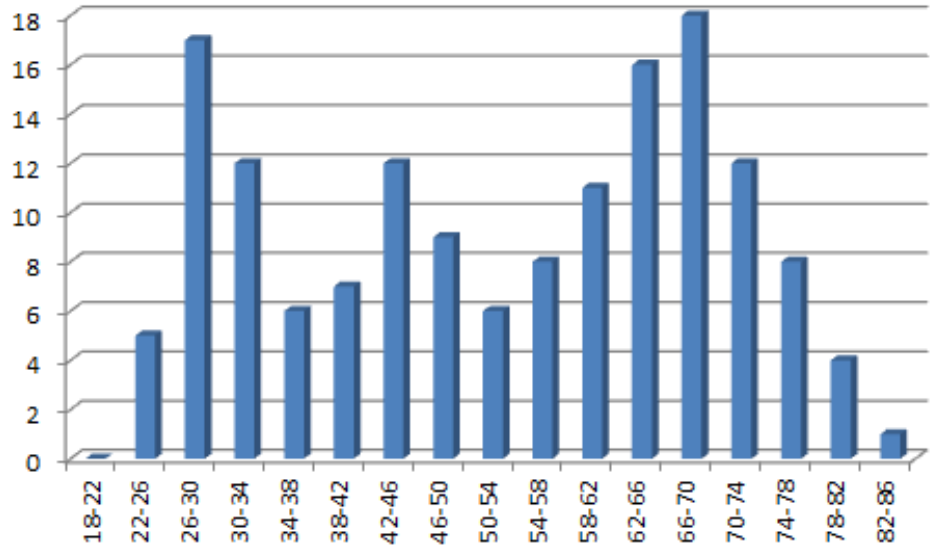

Figure 7.1: Age distribution of the IXI-152 cohort.

7.3 Spatial normalisation

The DARTEL spatial normalisation (applied to segmented images) performed better than the ANTs registration (applied directly on T1w images). For the T1w image set, the mean normalised mutual information for the T1w DARTEL normalised images was 1.33 compared to 1.18 for the ANTs normalized T1w images.

7.4 Intensity normalisation

7.4.1 Effect of intensity normalisation on VBSA results

For correlations with age, the VBIS and histogram peak intensity normalisation algorithms yielded very similar results. The whole brain mean scaling results differed considerably from the histogram peak and VBIS global intensity normalisation results. Because of the similarities between the peak and VBIS results, the figures show VBIS mean and whole brain mean results only, with the histogram results omitted. Results for all three normalisation methods are listed in the tables.

7.5 Age related changes

Statistically significant T1w changes with age are summarised in Tables 7.1 and 7.2 and illustrated in Fig. 7.2. Similarly, statistically significant T2w changes with age are summarised in Tables 7.3 and 7.4 and illustrated in Fig. 7.3. Statistically significant gray matter and white matter volume changes with age are summarised in Tables 7.5 and 7.6 and illustrated in Fig. 7.4.

7.5.1 T1w increases with age

For T1w increases with age (Table 7.1), whole brain mean intensity normalisation gave the strongest results in the form of a single very large cluster overlapping numerous white matter tracts including the external capsule, corona radiata and superior longitudinal fasciculus (right hand side of Fig. 7.2). The cluster also includes parts of the brainstem and cerebellum. The peak voxel is close to the border between the left external capsule and left putamen. The most significant clusters were in the cerebellum.

With VBIS and histogram peak normalisations, positive correlations between T1w and age were more diffuse (left hand side of Fig. 7.2). Other significant clusters, seen bilaterally were in the medial globus pallidus. Bilateral T1w increases with age were also seen in the thalamus.

7.5.2 T1w decreases with age

The most significant cluster, seen with all three normalisations, shows decreased T1w signal with age in a cluster that lines much of the lateral ventricles.

VBIS and peak normalisations both show significant results bilaterally on the boundary of the putamen and external capsule, but these results are absent from the whole brain mean analysis.

Negative correlations between T1w and age are detected in the vicinity of the thalamus (see Fig. 7.2, $x = -20$ sagittal slice).

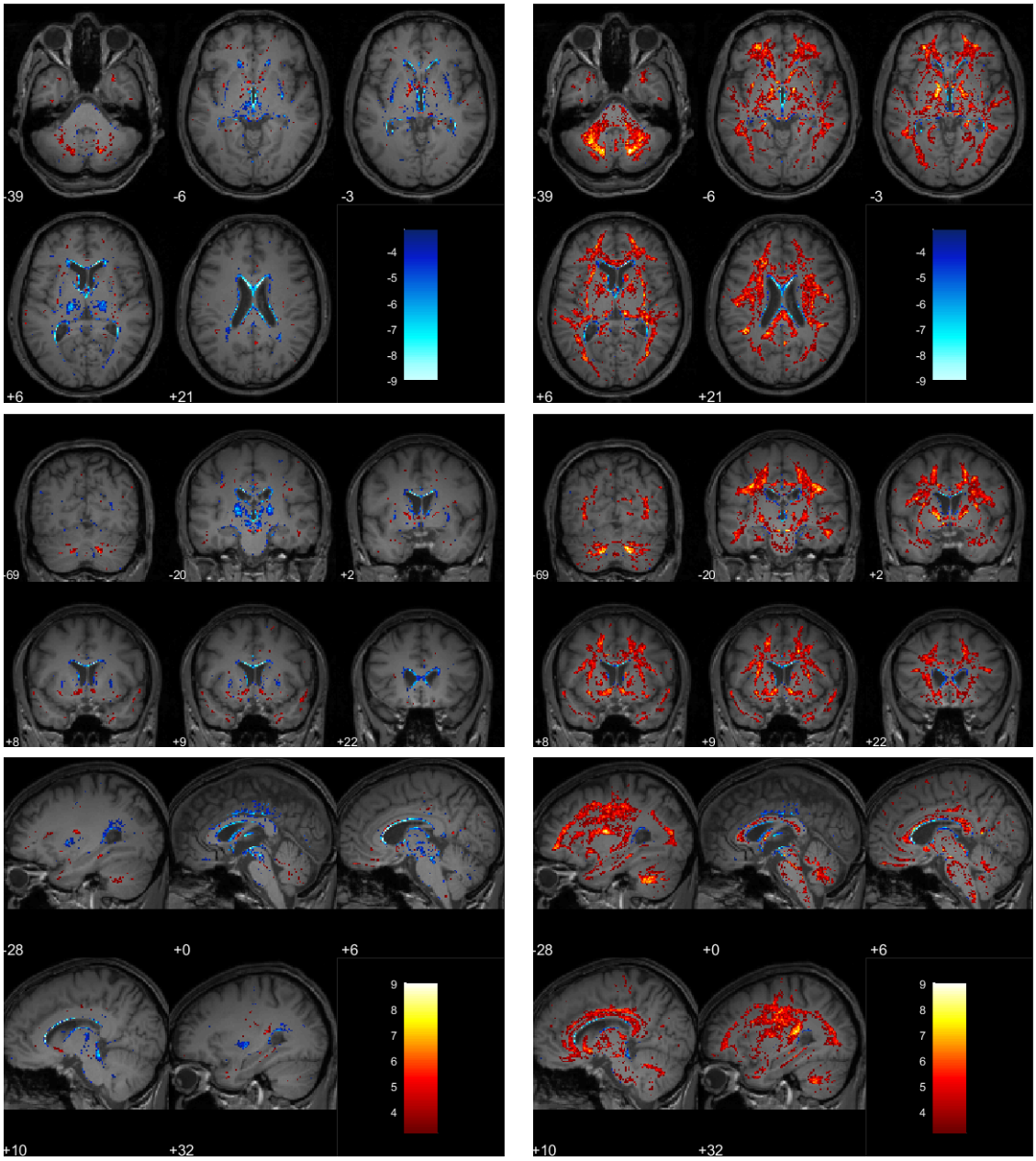

Figure 7.2: T1w correlations with age with VBIS scaling (left) and whole brain mean scaling (right). The t-statistic is color-coded and superimposed on T1w sections from a reference subject. Blue regions indicate negative correlations between age and MR signal, while warm colours indicate positive correlations. The colour bars run from t=3.15 to t=9, corresponding to uncorrected p-values of 0.001 and 5e-16, respectively.

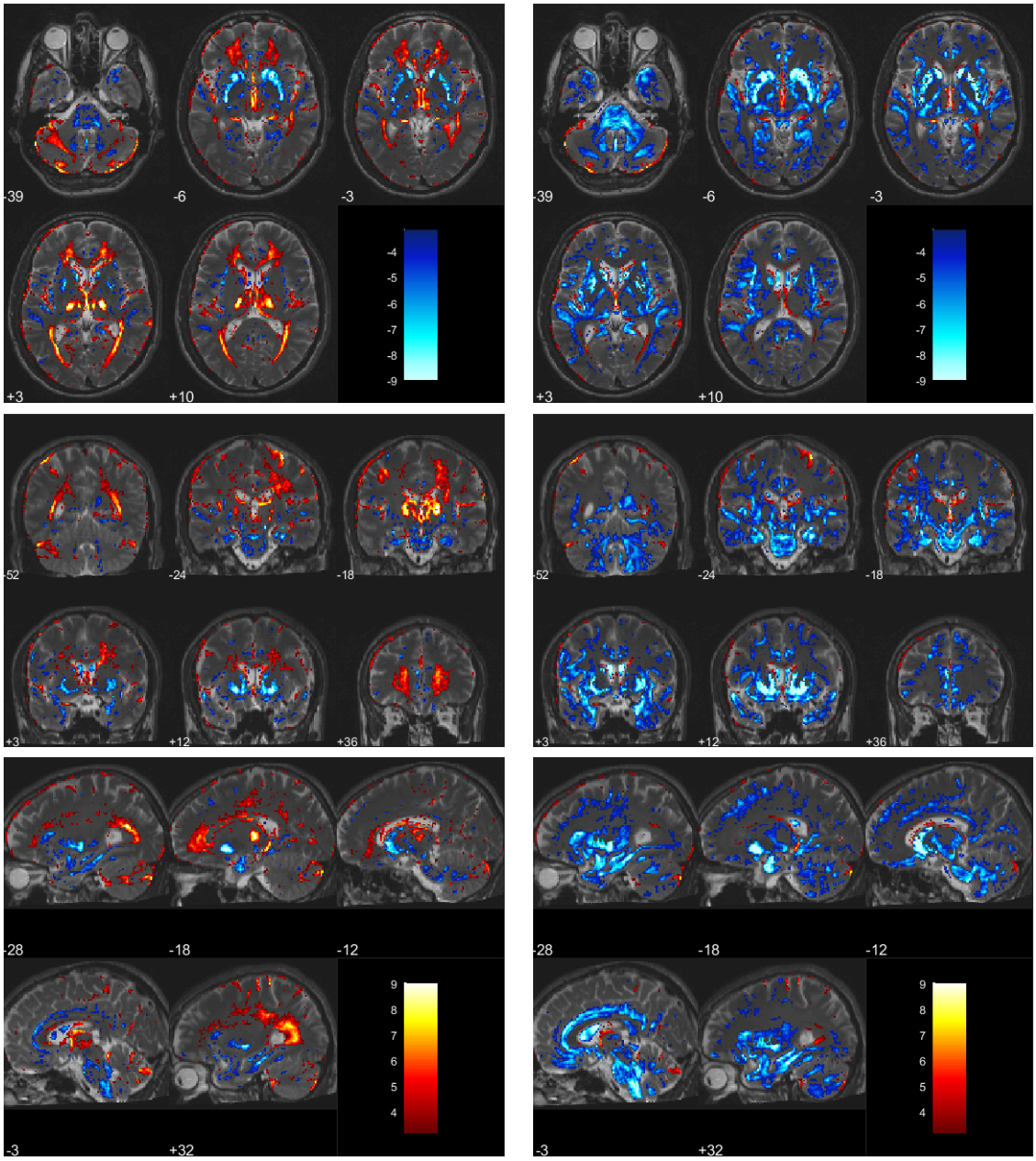

Figure 7.3: T2w correlations with age with vbis scaling (Left) and whole brain mean scaling (right). The t-statistic is color-coded and superimposed on T2w sections from a reference subject in this study. Blue regions indicate negative correlations between age and MR signal, while warm colours indicate positive correlations. The colour bars run from t=3.15 to t=9, corresponding to uncorrected p-values of 0.001 and 5e-16, respectively.

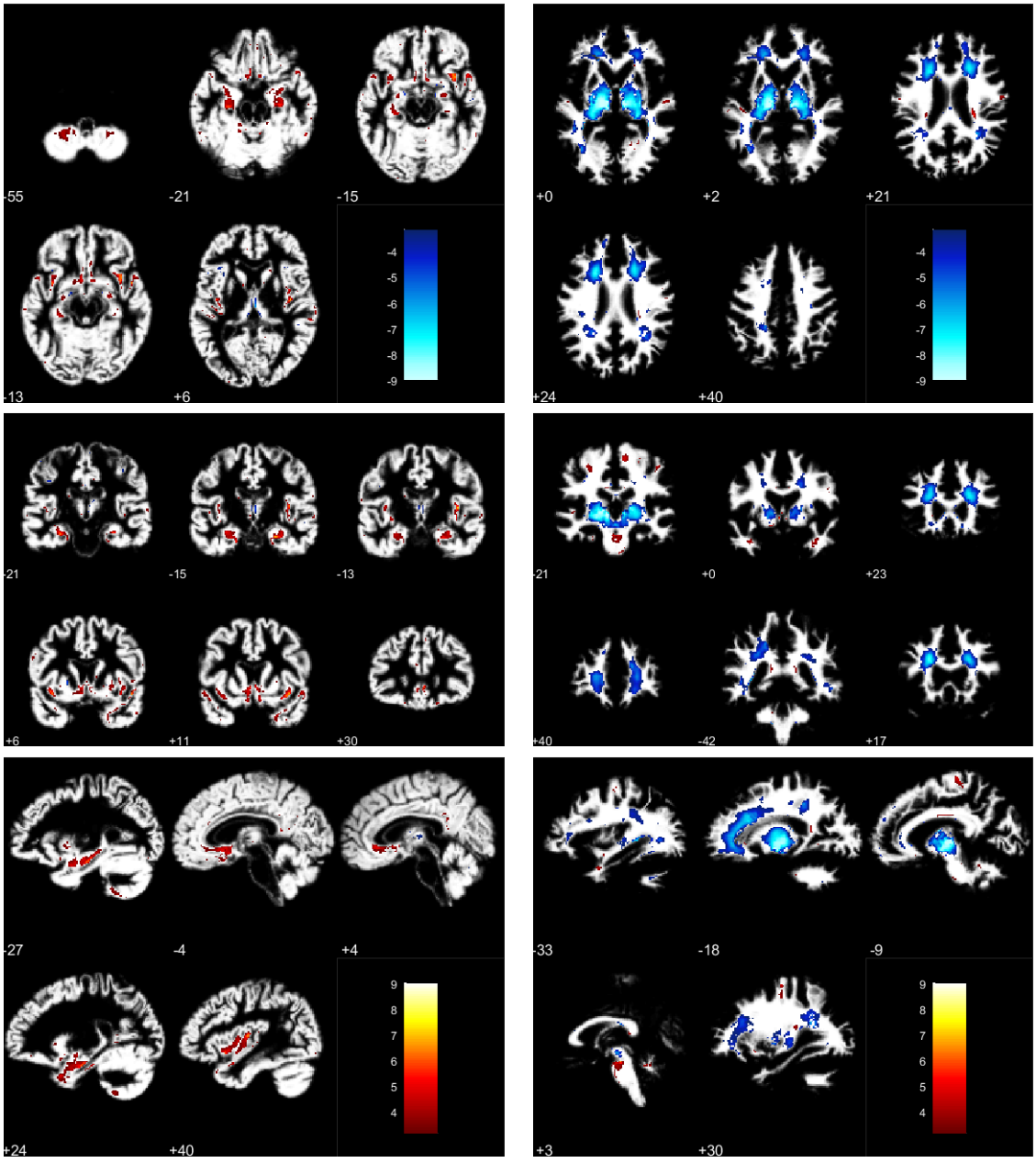

Figure 7.4: Gray and white matter volume changes with age relative to total gray and white volume respectively. The t-statistic is color-coded and superimposed on the gray matter (left) and white matter (right) images from this study. Blue regions indicate negative correlations between age and local tissue volume, while warm colours indicate positive correlations. The colour bars run from t=3.15 to t=9, corresponding to uncorrected p-values of 0.001 and 5e-16, respectively.

Table 7.1: T1w vs +age. Voxel and cluster statistics for positive correlations between T1w signal and age. p(unc) denotes the raw uncorrected p-value, q(FDR) denotes the false discovery rate q-value, and p(FWE) denotes the bonferoni corrected p-value. An additional multiple of 32 should be applied to these p-values to fully correct for multiple imaging modalities and contrasts as described in Subsection 6.4.6. equivk is a measure of cluster size, weighted according to image smoothness. See Subsection 5.3.6.

cluster				peak voxel				coords (mm)			intensity	cluster	
p(FWE)	q(FDR)	equivk	p(unc)	p(FWE)	q(FDR)	t	p(unc)	x	y	z	norm	id	region(s)
< 1E-99	< 1E-99	67350	< 1E-99	< 1E-99	3.E-10	9.9	4.E-16	-28	-9	10	mean	1	L dorsal putamen
< 1E-99	5.E-19	186	2.E-23	3.E-05	4.E-04	6.9	9.E-11	15	-69	-39	vbis	2	R cerebellum-Pyramis
< 1E-99	4.E-19	225	7.E-26	8.E-05	9.E-04	6.7	2.E-10	15	-69	-39	peak	2	R cerebellum-Pyramis
< 1E-99	7.E-14	155	5.E-20	2.E-02	1.E-02	5.6	6.E-08	-24	-52	-42	peak	3	L cerebellar Tonsil
1.E-16	7.E-14	160	1.E-19	5.E-04	2.E-03	6.3	2.E-09	-12	-2	-3	peak	4	R lentiform nucleas, medial globus pallidus
2.E-16	7.E-14	171	6.E-19	2.E-04	1.E-03	6.5	5.E-10	-3	0	-4	peak	5	Thalamus, lateral ventricle, caudate
2.E-16	4.E-16	167	4.E-19	2.E-04	2.E-03	6.5	7.E-10	-3	0	-4	vbis	5	Thalamus, lateral ventricle, caudate
2.E-16	4.E-16	150	4.E-19	7.E-04	3.E-03	6.2	2.E-09	-12	-2	-3	vbis	4	R lentiform nucleus, medial globus pallidus
4.E-15	8.E-13	130	8.E-18	4.E-02	2.E-02	5.4	1.E-07	-24	-52	-42	vbis	3	L cerebellar Tonsil
4.E-10	1.E-08	82	8.E-13	6.E-04	2.E-03	6.3	2.E-09	-14	-68	-39	peak	6	cerebellum-Pyramis
7.E-10	1.E-08	108	2.E-12	2.E-03	4.E-03	6.0	8.E-09	50	-24	-16	peak	7	L temporal WM tract
8.E-10	1.E-08	76	2.E-12	3.E-02	2.E-02	5.5	1.E-07	10	9	-10	peak	8	R Caudate
8.E-10	1.E-08	75	2.E-12	2.E-03	4.E-03	6.0	6.E-09	33	-39	10	peak	9	R frontal WM tract
1.E-09	1.E-08	83	3.E-12	6.E-04	2.E-03	6.3	2.E-09	14	-3	-3	peak	10	L lentiform nucleas, medial globus pallidus
1.E-09	1.E-08	88	3.E-12	5.E-02	2.E-02	5.4	2.E-07	33	-24	18	peak	11	insula/Parahippocampal gyrus
2.E-09	1.E-09	73	3.E-12	8.E-04	3.E-03	6.2	2.E-09	-14	-68	-39	vbis	6	L cerebellum-Pyramis
2.E-09	1.E-09	79	4.E-12	1.E-03	4.E-03	6.1	4.E-09	14	-3	-3	vbis	10	L lentiform nucleas, medial globus pallidus
2.E-09	1.E-09	71	4.E-12	5.E-02	2.E-02	5.4	2.E-07	10	9	-10	vbis	8	R Caudate
6.E-09	1.E-08	81	1.E-11	2.E-01	4.E-02	5.1	6.E-07	-33	-20	32	peak	12	R Cerebrum white matter
7.E-09	1.E-08	88	1.E-11	1.E-03	3.E-03	6.2	3.E-09	-15	-45	10	peak	13	corpus callosum/ posterior cingulum/ventrical edge
7.E-09	2.E-08	95	1.E-11	3.E-03	5.E-03	6.0	8.E-09	50	-24	-16	vbis	7	L temporal WM tract
2.E-08	2.E-08	62	4.E-11	3.E-03	5.E-03	5.9	1.E-08	33	-39	10	vbis	9	R frontal WM tract
4.E-08	2.E-08	72	7.E-11	6.E-02	3.E-02	5.3	2.E-07	33	-24	18	vbis	11	insula/Parahippocampal gyrus
4.E-08	1.E-08	87	8.E-11	3.E-03	5.E-03	5.9	1.E-08	3	-20	33	peak	14	cingulum/cingulate gyrus
2.E-07	5.E-08	105	3.E-10	7.E-02	3.E-02	5.3	2.E-07	-46	-15	-28	peak	15	WM underlying Fusiform gyrus
3.E-07	5.E-08	54	6.E-10	2.E-01	4.E-02	5.1	6.E-07	-36	-28	26	peak	16	parrahippocampal gyrus
4.E-07	1.E-07	62	9.E-10	5.E-01	7.E-02	4.9	2.E-06	-33	-20	32	vbis	17	WM tract underlyimg L frontal
7.E-07	1.E-07	68	1.E-09	4.E-03	5.E-03	5.9	1.E-08	-15	-45	10	vbis	13	corpus callosum/ posterior cingulum/ventrical edge
9.E-07	2.E-07	93	2.E-09	1.E-01	3.E-02	5.2	3.E-07	-50	-27	-21	vbis	18	WM underlying inferior temporal gyrus
6.E-06	2.E-06	49	1.E-08	3.E-04	2.E-03	6.4	1.E-09	30	-6	10	peak	19	R dorsal putamen
1.E-05	2.E-06	45	3.E-08	8.E-04	3.E-03	6.2	3.E-09	30	-6	10	vbis	19	R dorsal putamen
1.E-05	2.E-06	40	2.E-08	2.E-01	5.E-02	5.0	7.E-07	-36	-28	26	vbis	17	WM tract underlyimg L frontal

Table 7.2: T1w vs -age. Voxel and cluster statistics for negative correlations between T1w signal and age. p(unc) denotes the raw uncorrected p-value, q(FDR) denotes the false discovery rate q-value, and p(FWE) denotes the bonferoni corrected p-value. An additional multiple of 32 should be applied to these p-values to fully correct for multiple imaging modalities and contrasts as described in Subsection 6.4.6. equivk is a measure of cluster size, weighted according to image smoothness. See Subsection 5.3.6.

cluster				peak voxel				coords (mm)			intensity	cluster	
p(FWE)	q(FDR)	equivk	p(unc)	p(FWE)	q(FDR)	t	p(unc)	x	y	z	norm	id	region(s)
< 1E-99	6.E-28	7394	< 1E-99	0.E+00	2.E-11	10.38	4.E-16	6	22	2	vbis	1	lateral ventricle/corpuis callosum
< 1E-99	7.E-25	6982	< 1E-99	0.E+00	2.E-11	10.32	4.E-16	6	22	2	peak	1	lateral ventricle/corpuis callosum
< 1E-99	7.E-16	3167	< 1E-99	0.E+00	9.E-11	9.83	4.E-16	10	26	6	mean	1	lateral ventricle/corpuis callosum
< 1E-99	1.E-09	233	3.E-24	5.E-06	1.E-06	7.2	1.E-11	32	-9	-6	vbis	2	R putamen (lateral border)
< 1E-99	2.E-08	200	3.E-21	9.E-06	2.E-06	7.06	3.E-11	32	-9	-6	peak	2	R putamen (lateral border)
< 1E-99	1.E-09	283	6.E-21	1.E-07	8.E-08	7.83	4.E-13	0	-20	30	vbis	3	cingulum
< 1E-99	1.E-09	203	6.E-21	3.E-04	4.E-05	6.42	8.E-10	-28	2	-2	vbis	4	L putamen (lateral border)
2.E-16	2.E-08	182	5.E-19	5.E-04	7.E-05	6.28	2.E-09	-28	2	-2	peak	4	L putamen (lateral border)
3.E-16	2.E-08	244	7.E-19	1.E-07	8.E-08	7.83	4.E-13	0	-20	30	peak	3	cingulum
7.E-15	8.E-07	145	2.E-17	3.E-06	7.E-07	7.31	8.E-12	-14	-24	-21	mean	5	between midbrain and L parahippocampal gyrus
6.E-07	3.E-07	65	1.E-09	2.E-06	7.E-07	7.34	7.E-12	39	-16	36	vbis	6	R precentral edge of white matter
6.E-06	8.E-06	47	1.E-08	2.E-05	3.E-06	6.96	5.E-11	-14	-38	-2	mean	7	L parahippocampal gyrus
8.E-06	4.E-06	55	2.E-08	2.E-06	8.E-07	7.31	8.E-12	39	-16	36	peak	6	R precentral edge of white matter
1.E-05	4.E-06	45	3.E-08	3.E-03	3.E-04	5.95	9.E-09	-9	-21	-40	vbis	8	pons (ventral edge)
1.E-05	4.E-06	37	3.E-08	1.E-01	4.E-03	5.21	3.E-07	15	-44	-44	vbis	9	cerebellum(edge of WM tract)
2.E-05	7.E-06	44	4.E-08	4.E-03	3.E-04	5.9	1.E-08	-9	-21	-40	peak	8	pons (ventral edge)
4.E-05	3.E-05	34	8.E-08	5.E-08	4.E-08	8.01	2.E-13	-12	-40	-45	vbis	10	cerebellum(edge of L WM tract)
9.E-05	3.E-05	44	2.E-07	4.E-03	4.E-04	5.87	1.E-08	0	20	18	vbis	11	Anterior Corpus calosum

Table 7.3: T2w vs +age. Voxel and cluster statistics for positive correlations between T2w signal and age. p(unc) denotes the raw uncorrected p-value, q(FDR) denotes the false discovery rate q-value, and p(FWE) denotes the bonferoni corrected p-value. An additional multiple of 32 should be applied to these p-values to fully correct for multiple imaging modalities and contrasts as described in Subsection 6.4.6. equivk is a measure of cluster size, weighted according to image smoothness. See Subsection 5.3.6.

cluster				peak voxel				coords (mm)			intensity	cluster	
p(FWE)	q(FDR)	equivk	p(unc)	p(FWE)	q(FDR)	t	p(unc)	x	y	z	norm	id	region(s)
< 1E-99	< 1E-99	31898	9.9e-324	< 1E-99	2.E-11	10.95	4.E-16	36	-52	8	vbis	1	post. edge of lateral ventrical
< 1E-99	< 1E-99	12199	4.E-152	< 1E-99	1.E-10	10.19	4.E-16	2	-18	4	peak	2	fissure,thalamus
< 1E-99	1.E-61	4176	2.E-65	4.E-07	2.E-06	7.68	1.E-12	-42	-52	60	mean	3	Inf. parietal lobe edge
< 1E-99	7.E-45	5652	3.E-89	1.E-10	6.E-09	9.04	6.E-16	21	-92	-33	peak	4	edge of cerebellum
< 1E-99	7.E-45	6548	2.E-90	2.E-07	4.E-07	7.87	3.E-13	-42	-52	60	peak	3	Inf. parietal lobe edge
< 1E-99	4.E-33	2289	2.E-42	< 1E-99	3.E-10	9.75	4.E-16	2	-18	4	mean	2	fissure,thalamus
< 1E-99	4.E-33	1945	6.E-45	1.E-09	2.E-08	8.71	3.E-15	-26	-90	-36	mean	4	edge of cerebellum
< 1E-99	4.E-33	1504	3.E-37	1.E-09	2.E-08	8.71	3.E-15	21	-92	-33	mean	4	edge of cerebellum
< 1E-99	3.E-25	8697	4.E-130	< 1E-99	2.E-10	9.47	4.E-16	-36	-40	-42	vbis	5	cerebellar tonsil/edge
< 1E-99	3.E-25	8065	4.E-108	5.E-08	8.E-08	8.04	1.E-13	-42	-52	60	vbis	3	Inf. parietal lobe edge
< 1E-99	7.E-18	692	4.E-24	2.E-09	3.E-08	8.58	6.E-15	39	-20	4	peak	6	insula edge
< 1E-99	7.E-18	1295	3.E-27	2.E-06	2.E-06	7.43	4.E-12	33	-36	63	peak	7	post central gyrus
< 1E-99	3.E-17	531	6.E-20	8.E-06	4.E-06	7.14	2.E-11	2	28	16	vbis	8	edge of corpus calosum
< 1E-99	2.E-16	922	9.E-23	5.E-05	3.E-05	6.8	1.E-10	33	-36	63	mean	7	postcentral gyrus
1.E-14	1.E-14	407	3.E-17	2.E-04	4.E-05	6.52	5.E-10	51	10	-6	vbis	9	sylvian fissure
1.E-13	4.E-14	438	3.E-16	4.E-07	4.E-07	7.68	1.E-12	62	-4	39	vbis	10	Frontal lobe
1.E-13	1.E-13	401	4.E-16	5.E-05	1.E-05	6.81	1.E-10	8	-62	15	vbis	11	precuneus
2.E-12	1.E-12	307	8.E-15	7.E-03	5.E-04	5.84	2.E-08	-26	-102	-10	vbis	12	edge of occipital lobe
6.E-13	3.E-12	274	2.E-15	6.E-08	2.E-07	8.02	1.E-13	-16	-36	-2	peak	13	parahippocampal gyrus
2.E-13	5.E-12	546	6.E-16	6.E-04	2.E-04	6.32	1.E-09	33	-54	0	mean	1	post. edge of lateral ventrical
2.E-13	5.E-12	335	6.E-16	2.E-07	9.E-07	7.83	4.E-13	39	-20	4	mean	5	cerebellar tonsil/edge
6.E-12	8.E-12	244	2.E-14	3.E-05	9.E-06	6.91	6.E-11	33	66	-8	vbis	14	orbito-frontal edge
4.E-11	5.E-11	273	1.E-13	1.E-02	1.E-03	5.7	3.E-08	-26	-102	-10	peak	12	edge of occipital lobe
4.E-11	5.E-11	347	1.E-13	4.E-06	3.E-06	7.29	8.E-12	62	-4	39	peak	10	Frontal lobe
6.E-11	5.E-11	304	2.E-13	2.E-04	5.E-05	6.57	4.E-10	2	28	16	peak	15	edge of corpus calosum
6.E-11	7.E-11	218	2.E-13	5.E-03	7.E-04	5.92	1.E-08	-44	-16	6	mean	16	L sylvian fissure
3.E-09	1.E-09	219	1.E-11	1.E-06	8.E-07	7.51	3.E-12	-28	-44	-4	vbis	17	parahippocampal gyrus
8.E-09	2.E-09	261	3.E-11	9.E-04	2.E-04	6.25	2.E-09	6	-63	16	peak	11	precuneus
2.E-08	8.E-09	172	5.E-11	1.E-03	2.E-04	6.23	2.E-09	38	-8	33	peak	18	parahippocampal gyrus
4.E-08	8.E-09	235	1.E-10	7.E-03	5.E-04	5.83	2.E-08	-12	-33	44	vbis	19	cingulate gyrus
4.E-08	8.E-09	197	1.E-10	6.E-03	5.E-04	5.88	1.E-08	51	10	-6	peak	9	sylvian fissure
7.E-08	1.E-08	143	2.E-10	1.E-02	6.E-04	5.77	2.E-08	-36	-10	32	vbis	20	Precentral Gyrus
2.E-07	4.E-08	117	6.E-10	1.E-02	6.E-04	5.76	2.E-08	-4	-33	-22	vbis	21	Midbrain
2.E-07	4.E-08	209	7.E-10	1.E-04	3.E-05	6.64	3.E-10	69	-39	4	vbis		
2.E-07	6.E-08	136	5.E-10	6.E-05	2.E-05	6.77	1.E-10	33	66	-8	peak		
3.E-07	6.E-08	202	1.E-09	5.E-11	2.E-09	9.32	4.E-16	33	-24	62	peak		
4.E-07	1.E-07	231	1.E-09	5.E-04	8.E-05	6.34	1.E-09	32	-2	66	vbis		
4.E-07	1.E-07	194	1.E-09	2.E-03	2.E-04	6.07	5.E-09	57	18	32	vbis		
1.E-06	1.E-07	161	3.E-09	3.E-03	3.E-04	6.01	7.E-09	-8	-75	30	vbis		
2.E-08	2.E-07	190	6.E-11	4.E-02	3.E-03	5.46	1.E-07	-34	-98	-8	mean	12	0
5.E-07	2.E-07	153	2.E-09	3.E-06	3.E-06	7.31	8.E-12	-3	-42	-15	peak		
1.E-06	2.E-07	191	4.E-09	1.E-02	9.E-04	5.72	3.E-08	9	-26	45	peak		
1.E-06	2.E-07	124	5.E-09	6.E-06	5.E-06	7.19	2.E-11	-2	-69	-14	peak		
2.E-06	1.E-06	114	8.E-09	4.E-07	2.E-06	7.69	9.E-13	-16	-36	-3	mean		
3.E-06	1.E-06	163	1.E-08	7.E-10	2.E-08	8.8	2.E-15	33	-24	62	mean		
3.E-05	6.E-06	96	1.E-07	2.E-03	4.E-04	6.11	4.E-09	-38	-20	46	mean		

Table 7.4: T2w vs -age. Voxel and cluster statistics for negative correlations between T2w signal and age. p(unc) denotes the raw uncorrected p-value, q(FDR) denotes the false discovery rate q-value, and p(FWE) denotes the bonferoni corrected p-value. An additional multiple of 32 should be applied to these p-values to fully correct for multiple imaging modalities and contrasts as described in Subsection 6.4.6. equivk is a measure of cluster size, weighted according to image smoothness. See Subsection 5.3.6.

cluster				peak voxel				coords (mm)			intensity	cluster	
p(FWE)	q(FDR)	equivk	p(unc)	p(FWE)	q(FDR)	t	p(unc)	x	y	z	norm	id	region(s)
< 1E-99	< 1E-99	104579	< 1E-99	< 1E-99	1.E-12	13.3	4.E-16	-18	10	-9	mean	1	putamen, caudate
< 1E-99	< 1E-99	31390	< 1E-99	< 1E-99	9.E-12	11.84	4.E-16	-18	12	-9	peak	1	putamen, caudate
< 1E-99	4.E-29	976	4.E-33	6.E-10	2.E-09	8.83	2.E-15	4	26	21	peak	2	anterior cingulate
< 1E-99	3.E-26	15677	< 1E-99	< 1E-99	8.E-12	12.02	4.E-16	-18	12	-9	vbis	1	putamen, caudate
< 1E-99	3.E-20	696	8.E-30	3.E-08	3.E-08	8.13	8.E-14	-57	3	27	peak	3	L precentral
< 1E-99	2.E-16	414	1.E-19	4.E-04	4.E-05	6.41	9.E-10	-21	36	28	peak	5	Frontal lobe
< 1E-99	6.E-13	566	6.E-23	1.E-04	2.E-05	6.6	3.E-10	56	12	-15	vbis	4	R temporal Pole
< 1E-99	6.E-13	494	9.E-21	3.E-07	2.E-07	7.77	6.E-13	4	26	21	vbis	2	anterior cingulate
< 1E-99	6.E-13	491	1.E-19	2.E-06	9.E-07	7.38	5.E-12	-3	36	10	vbis	6	corpus calosum
2.E-16	6.E-13	448	7.E-19	3.E-04	4.E-05	6.44	8.E-10	-60	-24	2	vbis	8	L temporal
2.E-12	1.E-12	264	6.E-15	4.E-02	2.E-03	5.45	1.E-07	9	34	52	peak	12	R superior frontal gyrus
4.E-11	2.E-11	309	1.E-13	4.E-06	1.E-06	7.29	8.E-12	36	-38	-22	peak	14	R fusiform gyrus
1.E-16	1.E-10	536	2.E-19	7.E-06	9.E-07	7.16	2.E-11	40	-12	60	mean	7	R precentral
3.E-15	1.E-10	481	1.E-17	7.E-06	9.E-07	7.16	2.E-11	-14	-75	-34	mean	9	Cerebelum Uvula
5.E-15	1.E-10	409	2.E-17	9.E-03	3.E-04	5.79	2.E-08	-21	-82	-44	mean	10	Cerebellum
2.E-13	1.E-10	409	6.E-16	2.E-02	6.E-04	5.63	4.E-08	26	54	-4	mean	11	R superior frontal gyrus
1.E-11	1.E-10	549	4.E-14	< 1E-99	1.E-12	12.38	4.E-16	9	3	18	mean	13	R caudate body/Lateral ventricle
2.E-08	7.E-09	204	7.E-11	4.E-05	8.E-06	6.84	9.E-11	36	-38	-22	vbis	14	R fusiform gyrus
7.E-09	3.E-08	380	3.E-11	< 1E-99	1.E-12	13.39	4.E-16	-6	3	15	mean	15	L caudate body/Lateral ventricle
1.E-07	5.E-08	152	3.E-10	7.E-04	7.E-05	6.3	2.E-09	14	-57	-51	vbis	16	cerebellum
5.E-07	1.E-07	128	2.E-09	7.E-03	4.E-04	5.85	2.E-08	-44	6	6	vbis	19	L insula
1.E-06	2.E-07	118	4.E-09	2.E-02	9.E-04	5.61	5.E-08	-51	-9	16	vbis	20	L postcentral gyrus
4.E-07	3.E-07	181	1.E-09	2.E-04	3.E-05	6.51	6.E-10	50	-50	-15	peak	17	R fusiform gyrus
4.E-07	3.E-07	237	1.E-09	2.E-02	9.E-04	5.61	5.E-08	18	-75	-36	peak	18	R cerebellum
3.E-06	1.E-06	183	1.E-08	1.E-02	5.E-04	5.73	3.E-08	21	-68	-32	peak	18	R cerebellum
3.E-06	1.E-06	114	1.E-08	2.E-02	7.E-04	5.67	4.E-08	-22	12	44	peak	19	Frontal Lobe WM
4.E-06	1.E-06	102	1.E-08	2.E-05	4.E-06	7.01	4.E-11	-57	3	27	vbis	3	L precentral
1.E-05	2.E-06	131	3.E-08	3.E-02	1.E-03	5.51	8.E-08	-20	-66	-30	peak	20	L cerebellum
1.E-05	2.E-06	86	4.E-08	1.E-03	1.E-04	6.18	3.E-09	-6	-51	8	vbis	21	Precuneus/Post. Cingulate

Table 7.5: GMV vs +age. Voxel and cluster statistics for positive correlations between gray matter volume and age (normalised to total gray matter volume). p(unc) denotes the raw uncorrected p-value, q(FDR) denotes the false discovery rate q-value, and p(FWE) denotes the bonferoni corrected p-value. An additional multiple of 32 should be applied to these p-values to fully correct for multiple imaging modalities and contrasts as described in Subsection 6.4.6. equivk is a measure of cluster size, weighted according to image smoothness. See Subsection 5.3.6.

cluster				peak voxel				coords (mm)			cluster	
p(FWE)	q(FDR)	equivk	p(unc)	p(FWE)	q(FDR)	t	p(unc)	x	y	z	id	region(s)
< 1E-99	3.E-18	1304	6.E-24	1.E-05	2.E-04	6.83	1.E-10	24	-15	-24	1	R parahippocampal gyrus/ hippocampus, amygdala
1.E-11	3.E-11	532	2.E-13	3.E-06	1.E-04	7.08	3.E-11	40	-13	8	2	R insula
3.E-11	6.E-11	633	5.E-13	9.E-05	5.E-04	6.4	1.E-09	-27	-21	-21	3	L parahippocampal gyrus,hippocampus, amygdala
2.E-10	6.E-06	297	5.E-12	1.E-03	2.E-03	5.92	1.E-08	4	30	-6	4	anterior cingulate
4.E-09	6.E-06	333	8.E-11	2.E-03	3.E-03	5.77	2.E-08	-3	11	-6	5	L caudate
1.E-07	6.E-06	314	2.E-09	4.E-04	1.E-03	6.12	4.E-09	-36	6	-12	6	L insula
4.E-05	2.E-04	346	8.E-07	2.E-01	3.E-02	4.83	2.E-06	-21	-55	-58	7	L Cerebellum

Table 7.6: WMV vs - age. Voxel and cluster statistics for negative correlations between local white matter volume and age (normalised to total white matter volume). p(unc) denotes the raw uncorrected q-value, q(FDR) denotes the false discovery rate q-value, and p(FWE) denotes the bonferoni corrected p-value. An additional multiple of 32 should be applied to these p-values to fully correct for multiple imaging modalities and contrasts as described in Subsection 6.4.6. equivk is a measure of cluster size, weighted according to image smoothness. See Subsection 5.3.6.

cluster				peak voxel				coords (mm)			cluster	
p(FWE)	q(FDR)	equivk	p(unc)	p(FWE)	q(FDR)	t	p(unc)	x	y	z	id	region(s)
< 1E-99	1.E-58	8391	9.E-69	< 1E-99	1.E-11	10.43	4.E-16	-9	-19	0	1	Thalamus
< 1E-99	2.E-14	4570	1.E-25	5.E-08	8.E-08	7.84	4.E-13	-21	17	24	2	L Superior longitudional fasciculus
< 1E-99	2.E-14	4421	3.E-24	9.E-07	1.E-06	7.31	8.E-12	22	21	21	3	R Superior longitudional fasciculus
1.E-07	4.E-03	1080	5.E-09	2.E-03	4.E-04	5.87	1.E-08	-18	-42	40	4	L Parietal/temporal/Frontal lobe junction
2.E-07	4.E-03	707	7.E-09	6.E-04	2.E-04	6.08	5.E-09	30	-49	21	5	R Parietal/temporal/Frontal lobe junction
7.E-07	4.E-03	440	3.E-08	2.E-05	2.E-05	6.69	2.E-10	-33	-42	2	6	L Parietal/temporal/Frontal lobe junction

7.5.3 T2w increases with age

Increases in T2w signal intensity with age (red-yellow in Fig. 7.3) are seen on the outside edges of the cortex and cerebellum, at the edges of ventricles and in the midline fissures. With VBIS intensity normalisation, There are also peaks in the right thalamus, right precentral gyrus, right insula and left para-hippocampal gyrus.

The cluster also overlaps white matter tracts, notably the posterior thalamic radiation (axial slices x=+3,+10, coronal slice y=−52) and the anterior corona radiata(y=+36).

The decrease in the thalamus obtained with VBIS and peak scaling mirrors the significant decrease in T1w found in the same location.

7.5.4 T2w decreases with age

The blue-white overlays in Fig. 7.3 show the statistically strongest and most striking result from this analysis: a decrease in T2w signal with age bilaterally in the putamen and caudate heads. This cluster appears in all three intensity normalisations, but is strongest with whole brain mean normalisation. The cluster almost covers the entirety of these anatomical regions. There was also strong decreases seen in parts of the para-hippocampal gyrus, amygdala, cerebral peduncles and dorsal medulla (Fig. 7.3). At an uncorrected voxel p-value threshold of 0.001 the regions of significant differences in these areas merge into one extremely large cluster with a very low p value.

7.5.5 Gray matter volume changes with age

Clusters where gray matter loss significantly slower than the overall mean loss were detected were most significant in the para-hippocampal gyrus, amygdala and hippocampus and insula. There were also significant clusters in the caudate and cerebellum. There are no significant clusters of accelerated decreases evident in this analysis.

7.5.6 White matter volume changes with age

Accelerated white matter loss was detected bilaterally in the thalamus and anterior corona radiata. Regions where white matter loss was significantly slower than the overall trend were found in a cluster including the superior portion of the pons and part of the midbrain. Two clusters with decreased rate of white matter volume loss were also detected underlying the right supplementary motor area.

7.6 Gender Differences

Results from VBIS mean and whole brain mean intensity normalisation approaches are shown on the left and right hand side of Fig. 7.5 and 7.6. Fig. 7.5 shows T1w patterns of difference between genders. Fig. 7.6 shows T2w patterns of difference between genders. T1w gender difference results are listed in tables 7.7 and 7.8. T2w gender difference results are listed in 7.9 and 7.10.

Clusters showing significant gray matter differences between genders are listed in Table 7.11 and illustrated in Fig. 7.7. There were no significant white matter differences observed between genders.

7.6.1 T1 Gender differences

7.6.1.1 Locations where Females have higher T1w signal than Males

With whole brain mean intensity normalisation, there is a dominant cluster where T1w signal is significantly greater in Females. Most of the cluster is in white matter, the highest peak is near the junction of the right Putamen adjacent to the external capsule. There is also a similar pattern seen around the left putamen.

With VBIS and histogram normalisation, there are no significant T1w signal increases seen in females relative to males.

7.6.1.2 Locations where Males have higher T1w signal than Females

With VBIS and peak intensity normalisation, small clusters in the midbrain with significantly higher T1w signal in Males than in Females. secondary clusters were in the red nucleus. These results were stronger with peak normalisation. There were no significant clusters detected in the corresponding analysis with whole brain mean intensity normalisation.

7.6.2 T2 Gender Differences

7.6.2.1 Locations where Females have higher T2w signal than Males

With all three intensity normalisation algorithms, Females had significantly higher T2w signal in a large cluster including much of the superior longitudinal fasciculus and the superior internal capsule.

7.6.2.2 Locations where Males had higher T2w signal than Females

All three intensity normalisations detected significant clusters on the outer edges of the brain. Both VBIS mean and histogram peak intensity normalisation, revealed a cluster in the brainstem where males had significantly higher T2w intensity than females. With histogram peak scaling, significant clusters were also seen in the left and right insula and putamen. VBIS scaling revealed clusters in the midbrain, pons, and anterior cingulate.

7.6.3 Gray matter volume differences between genders

Males had increased gray matter volume (relative to total gray matter) compared to females are seen bilaterally in parts of the cerebellum and putamen. There was also a significant cluster encompassing parts of the left hippocampus, Amygdala and para-hippocampal gyrus.

No significant differences in white matter volume between genders is evident in this analysis.

7.6.4 White matter volume differences between genders

No significant differences in white matter volume between genders is evident in this analysis.

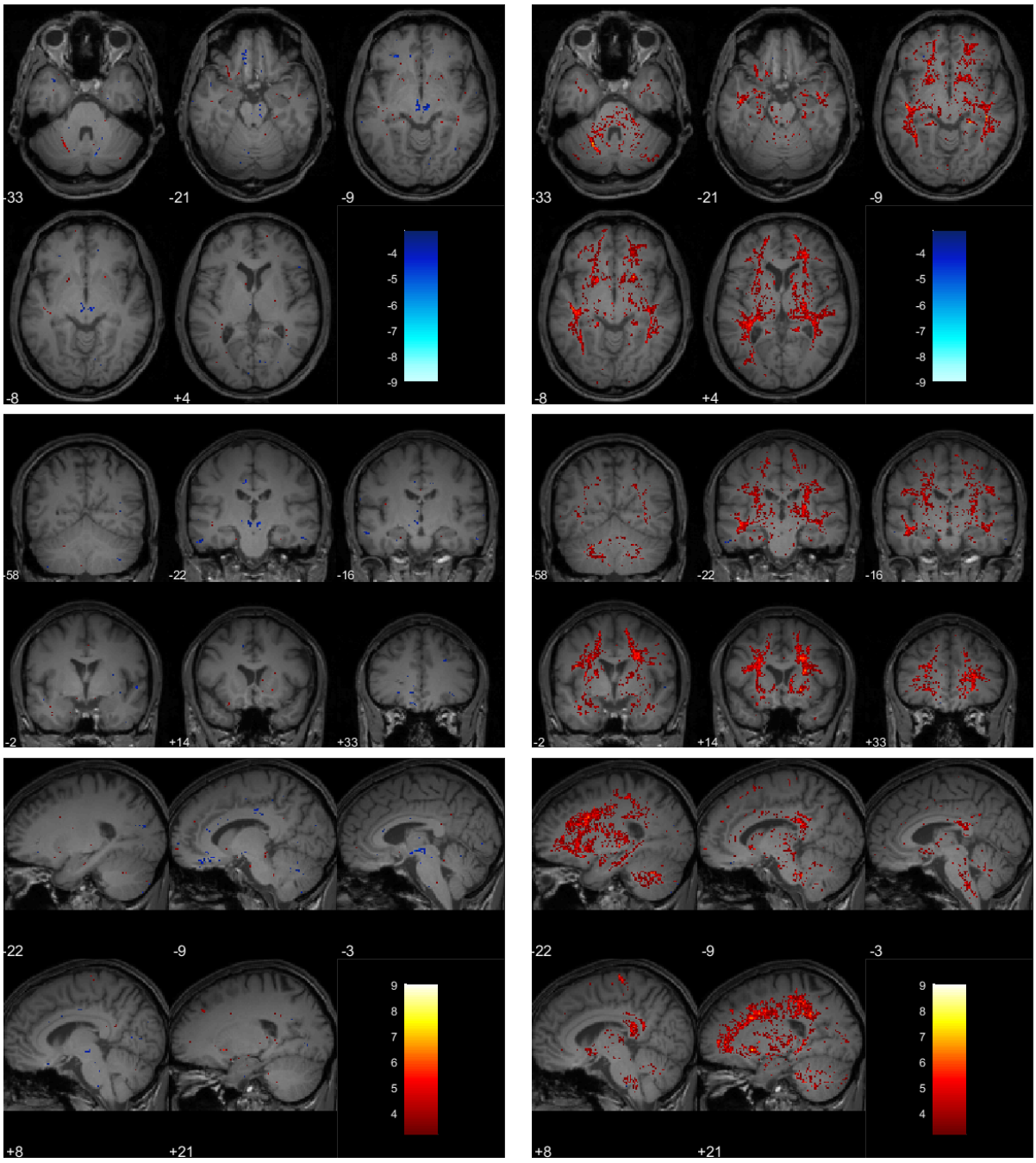

Figure 7.5: T1 gender differences with vbis scaling (Left) and whole brain mean scaling (right). Warm colours indicate the MR signal intensity is significantly higher in females. Cool colours indicate where the MR signal intensity is significantly higher in males.

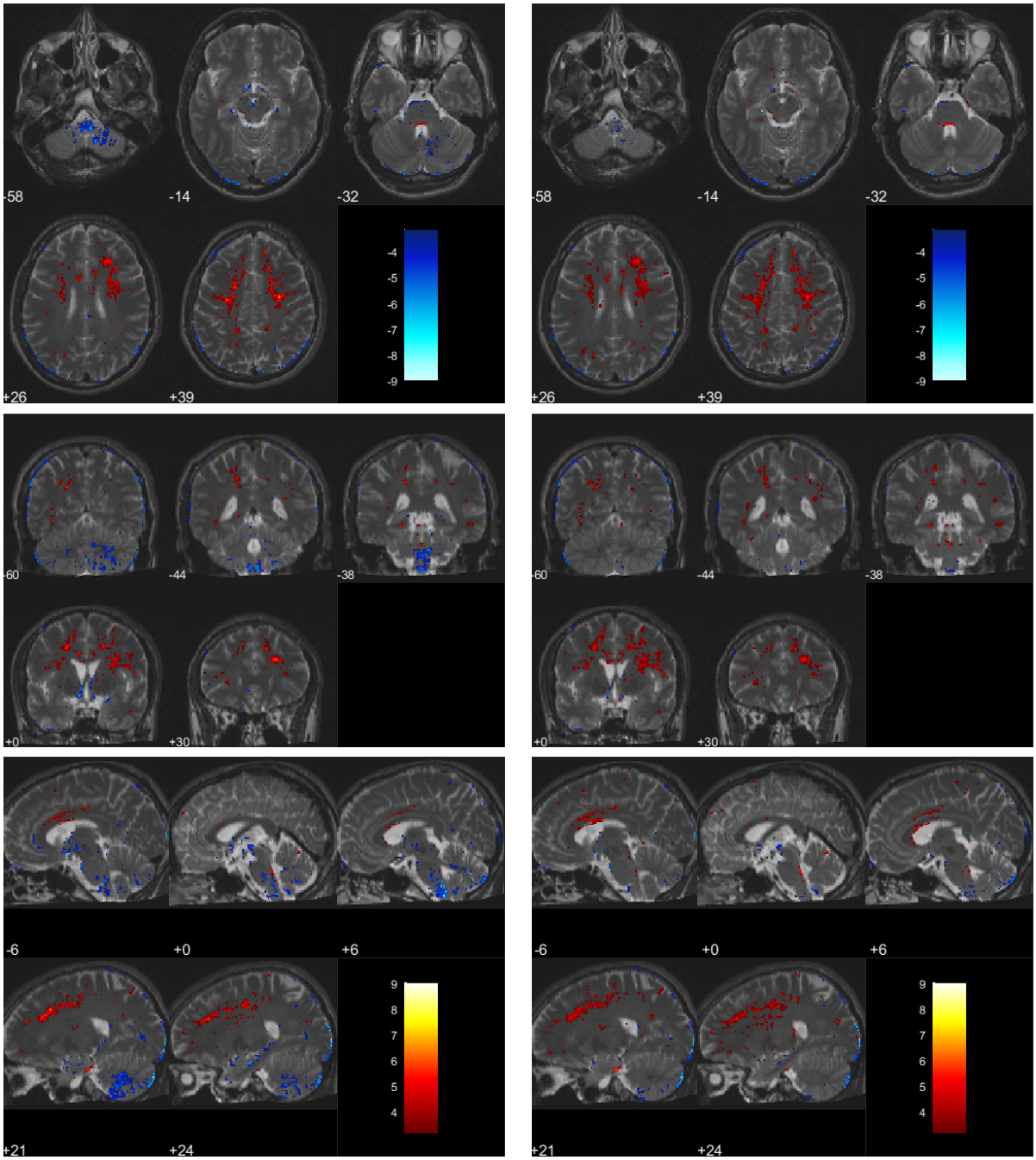

Figure 7.6: T2 vs gender with vbis scaling (Left) and whole brain mean scaling (right). Warm colours indicate the MR signal intensity is significantly higher in females. Cool colours indicate where the MR signal intensity is significantly higher in males. The t-statistic is color-coded and superimposed on sample T2w images from this study. The colour bars run from t=3.15 to t=9, corresponding to uncorrected p-values of 0.001 and 5e-16, respectively.

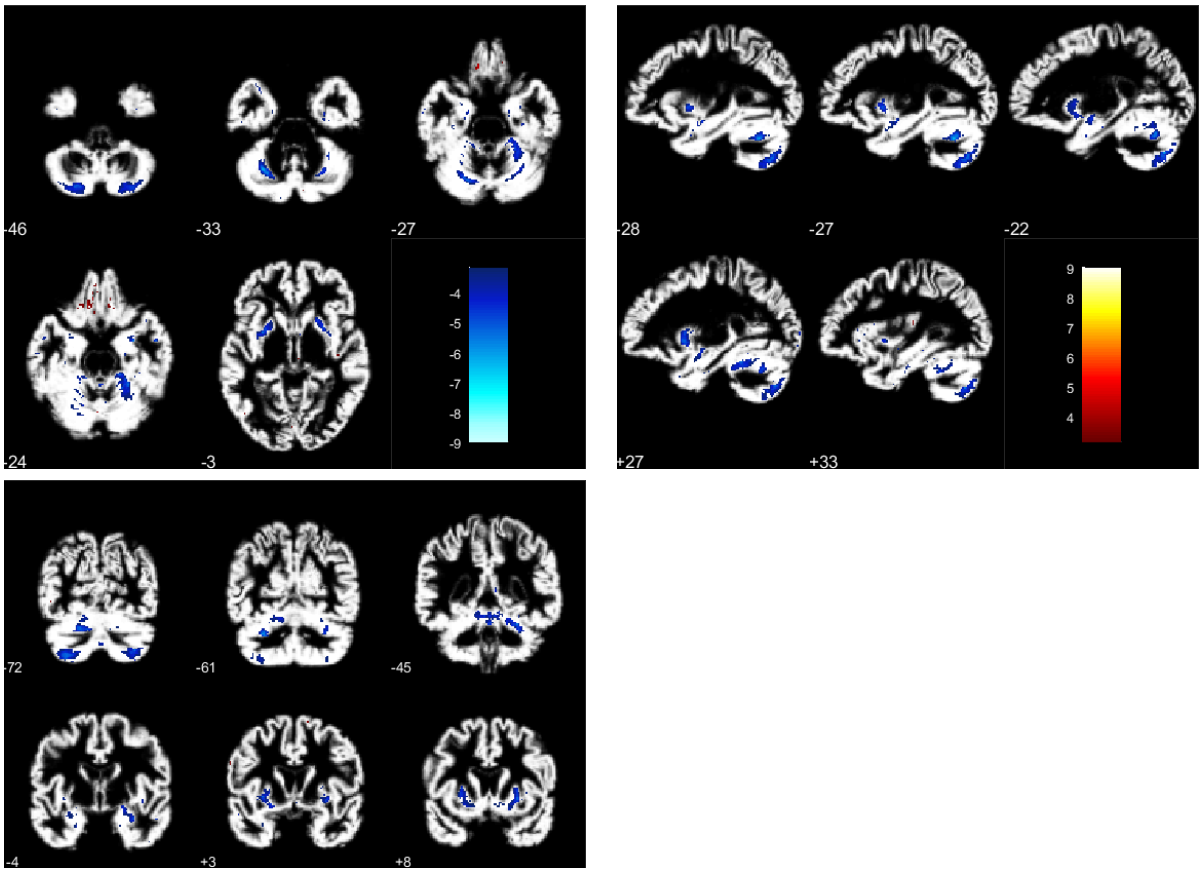

Figure 7.7: Gender differences in gray matter volumes. The t-statistic is color-coded and superimposed on a sample gray matter images from this study. Warm colours indicate the local GMV is significantly higher in females. Cool colours indicate where the local GMV is significantly higher in males (adjusted for total GMV). The colour bars run from t=3.15 to t=9, corresponding to uncorrected p-values of 0.001 and 5e-16, respectively.

Table 7.7: T1w: F > M. Voxel and cluster statistics for significant increases in T1w signal in females relative to males. p(unc) denotes the raw uncorrected p-value, q(FDR) denotes the false discovery rate q-value, and p(FWE) denotes the bonferoni corrected p-value. An additional multiple of 32 should be applied to these p-values to fully correct for multiple imaging modalities and contrasts as described in Subsection 6.4.6. equivk is a measure of cluster size, weighted according to image smoothness. See Subsection 5.3.6.

cluster				peak voxel				coords (mm)			intensity	cluster	
p(FWE)	q(FDR)	equivk	p(unc)	p(FWE)	q(FDR)	t	p(unc)	x	y	z	norm	id	region(s)
< 1E-99	< 1E-99	34508	< 1E-99	2E-06	1E-04	7.38	5E-12	21	14	-8	mean	1	putamen
< 1E-99	2E-25	2914	< 1E-99	2E-05	2E-04	6.92	6E-11	-22	-58	-33	mean	2	Culmen (L cerebellum)
< 1E-99	2E-06	283	2E-20	1E-02	3E-03	5.63	4E-08	-32	-72	4	mean	3	L occipital WM
5E-06	1E-05	46	1E-08	3E-01	2E-02	4.95	1E-06	-10	-16	-26	mean	2	Culmen (L cerebellum)
7E-05	6E-05	40	2E-07	5E-02	6E-03	5.37	2E-07	-30	-21	-16	mean	1	putamen

Table 7.8: T1w: M > F. Voxel and cluster statistics for significant increases in T1w signal in males relative to females. p(unc) denotes the raw uncorrected p-value, q(FDR) denotes the false discovery rate q-value, and p(FWE) denotes the bonferoni corrected p-value. An additional multiple of 32 should be applied to these p-values to fully correct for multiple imaging modalities and contrasts as described in Subsection 6.4.6. equivk is a measure of cluster size, weighted according to image smoothness. See Subsection 5.3.6.

cluster				peak voxel				coords (mm)			intensity	cluster	
p(FWE)	q(FDR)	equivk	p(unc)	p(FWE)	q(FDR)	t	p(unc)	x	y	z	norm	id	region(s)
6.E-07	2.E-05	48	1.E-09	1.E-01	0.23	5.2	3.E-07	8	-22	-9	peak	1	midbrain
1.E-06	2.E-05	48	2.E-09	1.E-01	0.23	5.17	4.E-07	-3	-16	-8	peak	2	midbrain (Red Nucleus)
2.E-06	3.E-06	42	4.E-09	2.E-01	0.27	5.1	5.E-07	8	-22	-9	vbis	1	midbrain
1.E-05	2.E-05	71	2.E-08	6.E-01	0.27	4.82	2.E-06	-9	33	-21	peak	3	Anterior cingulate
1.E-05	4.E-04	38	3.E-08	2.E-01	0.27	5.11	5.E-07	-3	-16	-8	vbis	2	midbrain (Red Nucleus)

Table 7.9: T2w: F > M. Voxel and cluster statistics for significant increases in T2w signal in females relative to males. p(unc) denotes the raw uncorrected p-value, q(FDR) denotes the false discovery rate q-value, and p(FWE) denotes the bonferoni corrected p-value. An additional multiple of 32 should be applied to these p-values to fully correct for multiple imaging modalities and contrasts as described in Subsection 6.4.6. equivk is a measure of cluster size, weighted according to image smoothness. See Subsection 5.3.6.

cluster				peak voxel				coords (mm)			intensity	cluster	
p(FWE)	q(FDR)	equivk	p(unc)	p(FWE)	q(FDR)	t	p(unc)	x	y	z	norm	id	region(s)
< 1E-99	1.E-87	4149	4.E-94	1.E-04	2.E-03	6.64	3.E-10	24	30	26	vbis	1	R superior WM
< 1E-99	3.E-36	11686	< 1E-99	1.E-02	7.E-02	5.77	2.E-08	28	-9	39	mean	2	R superior WM
< 1E-99	7.E-19	3218	2.E-81	7.E-04	5.E-03	6.28	2.E-09	-20	2	39	vbis	3	L superior WM
6.E-16	7.E-16	354	2.E-18	2.E-02	2.E-02	5.6	5.E-08	-28	-76	-3	vbis	4	R occipital WM
3.E-15	6.E-12	290	8.E-18	4.E-02	2.E-02	5.45	1.E-07	-20	-60	30	vbis	5	corpus calosum
< 1E-99	3.E-11	1066	2.E-29	5.E-01	1.E-01	4.91	1.E-06	-32	-63	15	mean	6	post. Thalamic Radiation
1.E-10	1.E-07	273	4.E-13	7.E-02	2.E-02	5.36	2.E-07	-10	9	28	vbis	7	corpus callosum
2.E-10	1.E-07	184	7.E-13	4.E-01	4.E-02	4.98	9.E-07	14	-32	52	vbis	8	paracentral lobule
5.E-08	4.E-06	213	2.E-10	9.E-01	1.E-01	4.76	2.E-06	42	-45	27	mean	9	sup. Long. Fasciculus
7.E-07	4.E-06	189	3.E-09	1.E+00	2.E-01	4.38	1.E-05	-36	-45	14	mean	10	sup. Long. Fasciculus
4.E-06	5.E-06	102	1.E-08	6.E-02	2.E-02	5.38	1.E-07	-39	-48	-4	vbis	11	sagital stratum
2.E-05	2.E-04	95	7.E-08	1.E+00	2.E-01	4.48	7.E-06	32	-28	48	mean		
6.E-05	2.E-04	92	2.E-07	8.E-03	7.E-02	5.8	2.E-08	0	-38	-32	mean		

Table 7.10: T2w: M > F. Voxel and cluster statistics for significant increases in T2w signal in males relative to females. p(unc) denotes the raw uncorrected p-value, q(FDR) denotes the false discovery rate q-value, and p(FWE) denotes the bonferoni corrected p-value. An additional multiple of 32 should be applied to these p-values to fully correct for multiple imaging modalities and contrasts as described in Subsection 6.4.6. equivk is a measure of cluster size, weighted according to image smoothness. See Subsection 5.3.6.

cluster				peak voxel				coords (mm)			intensity	cluster	
p(FWE)	q(FDR)	equivk	p(unc)	p(FWE)	q(FDR)	t	p(unc)	x	y	z	norm	id	region(s)
< 1E-99	2.E-62	20995	< 1E-99	8.E-10	1.E-08	8.78	2.E-15	6	-44	-58	peak	1	brainstem
< 1E-99	4.E-60	2943	1.E-65	5.E-08	2.E-07	8.07	1.E-13	18	-92	-36	vbis	2	R cerebellum edge
< 1E-99	8.E-42	2113	3.E-47	1.E-10	3.E-09	9.17	4.E-16	-15	-105	10	peak	3	L occipital lobe edge
< 1E-99	9.E-38	1857	4.E-44	2.E-10	4.E-09	8.98	8.E-16	-15	-105	10	vbis	3	L occipital lobe edge
< 1E-99	9.E-38	934	2.E-45	5.E-08	2.E-07	8.06	1.E-13	6	-44	-58	vbis	1	brainstem
< 1E-99	1.E-32	1657	4.E-41	3.E-10	3.E-09	8.94	9.E-16	-15	-105	10	mean	3	L occipital lobe edge
< 1E-99	1.E-23	754	2.E-26	< 1E-99	7.E-11	10.1	4.E-16	16	-105	0	vbis	4	R occipital lobe edge
< 1E-99	2.E-23	840	1.E-27	< 1E-99	1.E-10	10.22	4.E-16	16	-105	0	peak	4	R occipital lobe edge
< 1E-99	2.E-23	871	1.E-27	3.E-06	4.E-06	7.35	6.E-12	-40	-8	-50	peak	8	L temporsl edge
< 1E-99	2.E-23	1178	7.E-29	1.E-05	1.E-05	7.09	3.E-11	48	-81	14	peak	7	R occipital edge
< 1E-99	3.E-21	714	9.E-26	< 1E-99	5.E-11	10.03	4.E-16	16	-105	0	mean	4	R occipital lobe edge
< 1E-99	3.E-21	890	2.E-28	8.E-08	3.E-07	7.98	2.E-13	18	-92	-36	mean	2	R cerebellum edge
< 1E-99	3.E-21	911	4.E-25	6.E-05	2.E-05	6.79	1.E-10	48	-81	14	mean	5	R occipital edge
< 1E-99	1.E-19	472	1.E-22	2.E-07	5.E-07	7.87	3.E-13	-6	0	-14	vbis	6	mid brain/ optic tract
< 1E-99	1.E-19	572	7.E-23	7.E-07	2.E-06	7.6	2.E-12	-34	-82	-48	vbis	7	R parietal edge
< 1E-99	1.E-19	944	4.E-25	3.E-05	2.E-05	6.93	6.E-11	48	-81	14	vbis	5	R occipital edge
< 1E-99	1.E-19	618	2.E-22	3.E-05	2.E-05	6.88	8.E-11	-40	-8	-50	vbis	8	L temporal edge
< 1E-99	3.E-18	507	3.E-21	1.E-03	3.E-04	6.15	3.E-09	-9	45	-28	peak	9	WM underlying medial frontal Gyrus
< 1E-99	3.E-18	461	4.E-22	1.E-02	1.E-03	5.76	2.E-08	44	-21	0	peak	10	Insula
2.E-16	9.E-17	486	8.E-19	9.E-05	3.E-05	6.7	2.E-10	-40	-9	-50	mean	8	L temporal edge
6.E-14	2.E-12	357	2.E-16	3.E-02	3.E-03	5.55	7.E-08	-27	10	-3	peak	11	putamen
6.E-13	1.E-11	228	2.E-15	1.E-04	5.E-05	6.65	3.E-10	-9	-15	-27	vbis	12	pons
8.E-11	2.E-10	163	3.E-13	3.E-02	3.E-03	5.5	8.E-08	-34	-27	4	peak	13	insula
1.E-10	2.E-10	475	4.E-13	1.E-01	6.E-03	5.28	2.E-07	-34	40	44	peak	14	edge of frontal lobe
3.E-10	2.E-10	328	1.E-12	3.E-02	3.E-03	5.5	8.E-08	21	-81	3	peak	15	cuneus/R post edge of lateral ventrical
1.E-14	7.E-10	390	4.E-17	1.E-06	2.E-06	7.5	3.E-12	-21	-92	-38	mean	2	L cerebellum edge
2.E-08	8.E-09	343	6.E-11	3.E-01	1.E-02	5.03	7.E-07	-34	40	44	mean	14	edge of frontal lobe
1.E-09	1.E-08	209	5.E-12	6.E-02	4.E-03	5.39	1.E-07	-42	-15	-10	peak	16	Insula/Sylvian fissure
5.E-08	1.E-08	161	2.E-10	2.E-03	4.E-04	6.1	4.E-09	-12	36	-2	peak	17	Ant. Cingulate
2.E-10	1.E-07	270	6.E-13	7.E-04	2.E-04	6.31	2.E-09	44	-10	-48	vbis	18	precentral gyrus
2.E-08	1.E-07	362	6.E-11	3.E-01	1.E-02	5.03	7.E-07	-34	40	44	vbis	19	frontal lobe edge
4.E-07	1.E-07	97	1.E-09	4.E-05	2.E-05	6.87	8.E-11	26	-16	-21	vbis	20	parahippocampal gyrus
7.E-07	1.E-07	174	2.E-09	6.E-04	2.E-04	6.33	1.E-09	70	-40	3	vbis	21	edge of Temp. Lobe
2.E-07	2.E-07	140	7.E-10	1.E-03	2.E-04	6.21	3.E-09	-9	-15	-27	mean		
8.E-07	2.E-07	164	3.E-09	1.E-03	2.E-04	6.23	2.E-09	70	-40	3	mean		
5.E-07	4.E-07	183	2.E-09	2.E-04	9.E-05	6.53	5.E-10	70	-40	3	peak		
1.E-05	4.E-06	124	4.E-08	3.E-01	1.E-02	5.01	8.E-07	14	26	-21	peak		
8.E-06	4.E-06	108	3.E-08	7.E-06	5.E-06	7.16	2.E-11	-56	-74	-6	mean		

Table 7.11: GMV: M > F. Voxel and cluster statistics for significant increases in gray matter volume in males relative to females. p(unc) denotes the raw uncorrected p-value, q(FDR) denotes the false discovery rate q-value, and p(FWE) denotes the bonferoni corrected p-value. An additional multiple of 32 should be applied to these p-values to fully correct for multiple imaging modalities and contrasts as described in Subsection 6.4.6. equivk is a measure of cluster size, weighted according to image smoothness. See Subsection 5.3.6.

cluster				peak voxel				coords (mm)			cluster	
p(FWE)	q(FDR)	equivk	p(unc)	p(FWE)	q(FDR)	t	p(unc)	x	y	z	id	region(s)
8.E-16	1.E-13	1060	2.E-17	7.E-03	2.E-02	5.52	8.E-08	27	-45	-24	1	Rcerebelum (Culmen)
3.E-14	1.E-13	729	6.E-16	1.E-04	3.E-03	6.32	1.E-09	-27	-61	-33	2	L cerebelum (Culmen)
2.E-10	2.E-08	1013	4.E-12	1.E-03	7.E-03	5.88	1.E-08	-22	-76	-46	3	L cerebelum (post. Lobe)
6.E-08	5.E-07	725	1.E-09	9.E-03	2.E-02	5.48	9.E-08	33	-72	-48	4	R cerebelum (post. Lobe)
3.E-07	5.E-07	400	5.E-09	2.E-02	2.E-02	5.26	2.E-07	-28	3	-3	5	L putamen
7.E-07	5.E-07	383	1.E-08	3.E-02	2.E-02	5.24	3.E-07	27	8	-4	6	R putamen
8.E-06	3.E-02	204	2.E-07	7.E-03	2.E-02	5.51	8.E-08	32	-4	-24	7	L parrahippocampal gyrus, hippocampus, amygdala

Chapter 8

Discussion

8.1 Introduction

The results presented in the previous chapter included many notable statistically significant results. In the first part of this chapter, the possible physiological significance of these changes is discussed, first for the age related changes and then for the gender differences. The possible reasons for the differences between results obtained using the different intensity normalisation algorithms is then examined. Finally, the performance of the spatial normalisation algorithms are discussed.

8.2 Age related MR signal changes

8.2.1 T2w decreases with age and iron accumulation in the brain

The statistically strongest and most striking result obtained in this work is the decrease in T2w signal with increasing age encompassing the left and right putamen and caudate heads. A decrease in T2w indicates decreased transverse (T2) relaxation time. The same trend is observed in parts of the amygdala, para-hippocampal gyrus and brainstem.

The most likely explanation for these decreases in T2w signal is a significantly more rapid increase in iron concentration with age in these locations relative to the rest of the brain.

8.2.1.1 Iron, inflammation and microvascular disease

The effect of iron on T2w signal was discussed in Section 3.3.4. Recall that there are two kinds of iron in the body: haemoglobin (haem) iron and non-haem iron. In normal circumstances, haemoglobin is not able to cross the blood brain barrier and is therefore not expected to have a large influence on the MRI signal. On the other hand non-haem iron (often bound by the transporter protein transferrin) is transported across the blood-brain barrier into the brain parenchyma (Moos 2002). Within the brain, most iron is stored in the form of ferritin which therefore is the dominant contributor to the iron component of the MR signal. Transferrin and unbound iron are also present, but in smaller quantities.

Though the MR signal is dominated by ferritin, there is a good correlation between bound and unbound non-haeme iron in oligodendrocyte cells (Salgado et al. 2010, Daugherty & Raz 2015). Unbound iron is of particular interest as in this form, it can promote oxidative stress, inflammation and interfere with normal brain metabolism. Such changes may be considered as part of the broader phenomena of 'inflamm-aging', whereby there is a progressive increase in the pro-inflammatory status with aging (Franceschi et al. 2000). Inflamm-aging may be accelerated in the striatum due to its higher metabolic rate as well as it's high iron content.

Given that microvascular bleeds are more common in the putamen than other areas of the brain[19] (Smith et al. 2012), the most likely explanation for the accumulation of iron with age is through the cumulative effects of multiple cerebro-vascular micro-bleeds, leading to saturation of iron storage (Janaway et al. 2014).

Following a vascular injury, there is infiltration of leukocytes (red blood cells carrying haeme iron) into the brain parenchyma. The cellular debris are initially taken up by glial cells acting as macrophages. Astrocytes form part of the blood brain barrier through their end feet which attach to microvessels enabling them to modulate the blood supply. Following vascular injury, proliferation of astrocytes is triggered. The iron is eventually transferred into the astrocytes where it accumulates in haemosiderin complexes (Craggs et al. 2014), haemosiderin being an amalgamation of ferritin and denatured ferritin proteins. This picture is supported by the immuno-staining study (Connor et al. 1990) which found that while most of the iron was present in oligodendrocytes, the concentration remained relatively stable with advancing age. In contrast, iron concentration in astrocytes tended to be greater in older subjects.

Other possible factors proposed in (Drayer 1988) that may contribute to the increased accumulation of iron with aging include decreased oxidative phosphorylation, decreased dopamine production and turnover, abnormal blood brain barrier permeability, and acceler-

[19]The author thanks Dr Wilson Vallat for suggesting this explanation.

ated hydroxyl free radical formation with lipid membrane peroxidation.

8.2.1.2 Related studies

Our results are supported by numerous other studies in the literature. The histopathological study of Hallgren and Sourander demonstrated increased iron in the putamen with age, for ages twenty to fifty, with the data becoming more scattered above the age of fifty (Hallgren & Sourander 1958). The immunostaining study (Connor et al. 1990) showed iron accumulation in the amygdala and basal ganglia with age. Cass et al found increased iron content with age in the striatum of rhesus monkeys (Cass et al. 2007). Aquino et al found increased R2 in the basal ganglia with age which they also attributed to increasing iron content[20] (Aquino et al. 2009). Haacke et al also reported increasing iron content with age based on MRI (Haacke et al. 2010). Steiger et al found R2* increases with age in the striatum and in addition, a correlation between iron accumulation in the striatum and memory performance (Steiger et al. 2016).

Some neuro-degenerative conditions show abnormal patterns of iron accumulation in specific parts of the brain. In patients with Parkinson's disease, increased iron in the basal ganglia has been reported based on T2 relaxivity MR imaging measurements (Burgetova et al. 2010). In contrast, the basal ganglia in Alzheimer's disease are similar to those in healthy controls (Connor 2013), despite increased iron content observed in other brain areas including the amygdala, hippocampus and globus pallidus.

The significant decreases in T2w in the brainstem reported here are consistent with results of Lambert et al. who reported increases in R2* signal in parts of the midbrain (Lambert et al. 2013), however they also reported more widespread increases in R2* in the brainstem that were not detected in this work.

8.2.1.3 Relationship between neurotransmitters and iron in the striatum

Iron concentration is not uniform across the brain and shows "a peculiar predilection for the circuits associated mainly with the domain of movement" (Daugherty & Raz 2015). The striatum is notable as being a major dopaminergic centre and having high energy metabolism, as is evident from ^{18}FDG PET imaging. This higher energy metabolism may result in increased wear and tear on the cells leading to a more rapid build up of iron metabolites.

Iron is known to be involved in neurotransmitter synthesis. Neurotransmitter levels also change with age. For example glutamate levels in the striatum decrease significantly with advancing age (Zahr et al. 2013) and correlate with cognitive decline. It is likely that

[20] Recall that $R2 = T2^{-1}$, so increased R2 implies decreased T2w signal.

increased iron would influence the homoeostatic balance between glutamate, dopamine and other neurotransmitters in these areas (Smythies 1999).

Abnormalities in putamen volume and glucose metabolic rate have been reported in Schizophrenia and schizotypal personality disorder (Shihabuddin et al. 2001). Increased putamen volume has also been reported in adults with autism (Sato et al. 2013). This suggests this region may be relevant to neuro-developmental and neuro-psychiatric disorders.

Further studies examining the correlation between iron accumulation and glutamate levels (measured with MR), and other measures such as glucose metabolic rate, and dopamine uptake may provide further insight in to the aging striatum in health and disease.

8.2.1.4 Iron and Cognitive function

Several studies have reported associations between increased iron (as inferred from MRI) and decreased cognitive ability in the basal ganglia and the brain as a whole (Daugherty & Raz 2015). (Ghadery et al. 2015) reported a correlation between increased R2* in the basal ganglia brain tissue and worse performance in global cognition, executive function and psychomotor speed tasks. A longitudinal study (Raz et al. 2003) reported a connection between iron accumulation in brain regions and subsequent volume loss in the affected regions.

8.2.1.5 Influence of Iron on T2w at different field strengths

The effect of iron on T2w signal is found to be amplified at higher field strength, this phenomena has been used in (Daugherty & Raz 2015) to define an index, 'the field-dependent R2 increase' which reflects iron content. Computation of this index requires subjects to be scanned in two scanners with different field strengths. As the remainder of the IXI images were scanned at 1.5 T, a population based comparison between the 3T and 1.5T IXI data sets may provide further support for the hypothesis of increasing iron content with age in the human brain.

8.2.2 T2w increases with age

The increases in T2w signal seen in the peri-ventricular regions and outer edge of the cortex are almost certainly due to age related brain atrophy(loss of tissue volume) inadequately compensated for by the intensity normalisation algorithm. As the brain tissue volume decreases, the space is filled by cerebro-spinal fluid that appears much brighter on T2w imaging, accounting for these results. Increases in T2w signal in the thalamus are mirrored by decreases in T1w signal and are discussed further in the following section.

8.2.3 T1w decreases with age

As for the T2w increases with age, with whole brain mean intensity normalisation, the most statistically significant decreases in T1w with age are primarily in the peri-ventricular regions and the outer edges of the brain and fissures and are likely due to inadequate compensation for brain atrophy by the spatial normalisation algorithm. If voxels containing gray or white tissue are replaced by cerebro-spinal fluid, a decrease in T1w signal and an increase in T2w will result. This will be more pronounced for older subjects and the resulting changes in their whole brain means will bias scaling to accelerate positive T1w ageing and negative T2w ageing.

With VBIS and peak scaling, which exclude the effects of para-ventricular and outer-edge voxels (Figures 6.2, 6.3), the areas of decrease in T1w (Figure 7.2) with age seen in the thalamus are mirrored by a significant decrease in T2w (Figure 7.3). This is consistent with the accelerated white matter volume loss in the thalamus with age (Figure 7.4) indicating a decrease in myelin with age which leads to an increase in both T1 and T2 relaxation times (an decrease in T1w and an increase in T2w) with age.

8.2.4 T1w increases with age

With whole brain mean normalisation, there are widespread increases in T1w signal with age found in numerous white matter tracts (Figure 7.2). The absence of these results with other intensity normalisation algorithms, the likelihood of upward bias in T1w ageing with whole-brain mean scaling, and the conflict with or absence of corresponding white matter volume changes, casts serious doubt on the reliability of these findings. With VBIS mean and histogram based normalisations, the more peripheral regions of the brain have a much smaller influence in determining the global intensity normalisation scaling factors because the signal values in deep white matter are more uniform across age groups.

Steiger found correlations between magnetisation transfer MRI intensity and age concentrated in these same areas (Steiger et al. 2016) [21]

8.2.5 Volumetric age related changes

There have been a number of previous VBM studies of aging, the largest being (Good et al. 2002). The relative preservation of GMV seen this work in the hippocampus and amygdala is corroborated by that study.

[21] Unfortunately, VBSA of T1w or R1 images were not performed in that study.

While both studies found significant decreases in the thalamus, Good et al. saw decreases primarily in gray matter while the analysis reported here shows white matter volume decreases in the thalamus. The segmentation algorithm used in (Good et al. 2002) is from an older version of SPM; The segmentation algorithm from SPM12 (Ashburner & Friston 2005) used for this work has been significantly revised from previous versions which may account for some of the discrepancy.

8.2.5.1 Iron and mis-segmentation

Gotto et al (Goto et al. 2013) have reported the occurrence of mis-segmentation due to the inability of segmentation algorithms to take into account variance in T1 signal due to iron content as well as myelin content. It would be of interest to develop an algorithm which uses T2w or T2*w images in conjunction with T1w images to take the effects of iron into account.

8.3 Gender Differences

8.3.1 Gender differences in T1w and T2w weighted images

Recall that with whole brain mean scaling, the female group showed a simultaneous increase in T1w and T2w in the internal capsule, corona radiata and prefrontal white matter areas. The increase in T1w is consistent with females having increased myelin content in these regions, however this alone would also lead to a decrease in T2w signal which is not consistent with the T2 result. A significantly greater non-haeme iron content in males in these white matter regions would be needed to counteract this effect giving the observed result.

Alternatively the results could be explained by a higher proton density in these regions in females. A third possibility is the global normalisation values may be gender biased and that the there is actually no local white matter differences between gender in these regions, but rather more subtle diffuse differences spread across the brain. It may be that in this case, VBIS mean and peak intensity scaling provides a more accurate description of the local differences.

The origin of the increased T1w signal in males in the midbrain may be increased white matter/myelination in this location compared to females. Increased T2w signal in Males seen with VBIS and histogram peak scaling in the brainstem and cerebellum are consistent with greater amounts of non-haeme iron in males in these locations.

8.3.2 Volumetric Gender Differences

The increased gray matter for males was also reported in (Good et al. 2001) in the amygdala, hippocampus and anterior lobe of the cerebellum. Good et al. also observed this difference in the temporal lobe but those results do not corroborate the difference in the putamen reported here.

8.4 Effect of Intensity Normalisation on VBSA results

8.4.1 Relationship between global T1w and T2w values

The variation between the three global intensity measures can be assessed by looking at the variation in their ratio across subjects. These ratios are shown in Table 8.1. For T1w, the concordance between the histogram and VBIS measures is remarkable and explains the strong concordance between VBSA results obtained with these two intensity normalisations. For the ratios of histogram peak to VBIS, the coefficient of variation (CoV) is less than half of one percent while for the other two ratios involving the T1 mean, the CoV is four times larger, though still modest at just under 1.5%. The greater variance deriving from the T1w mean scaling reflects the strong but variable effects of paraventricular and brain edge CSF on the whole brain means as discussed in 8.2 above. For the T2w analysis, the ratios of globals were moreuniform. The least variance again being between the VBIS and histogram peak intensity measures; consistent with the VBSA results for VBIS and peak normalisations being the most concordant.

	T1w VBIS/ T1w mean	T1w peak/ T1w mean	T1w peak/ T1w VBIS	T2w VBIS/ T2w mean	T2w peak/ T2w mean	T2w peak/ T2w VBIS
mean	1.253	1.291	1.030	0.896	0.705	0.787
SD	0.016	0.018	0.004	0.039	0.037	0.025
CoV	0.013	0.014	0.004	0.043	0.052	0.032

Table 8.1: Variation across subjects in the ratios between the three global intensity measures (whole brain mean, VBIS region mean and histogram peak) for both T1w and T2w images. Abbreviations: SD Standard deviation; CoV Coefficient of Variation.

	T1w VBIS/ T1w mean	T1w peak/ T1w mean	T1w peak/ T1w VBIS	T2w VBIS/ T2w mean	T2w peak/ T2w mean	T2w peak/ T2w VBIS
age	0.57	0.51	-0.05	-0.62	-0.33	0.31
gender	0.47	0.47	0.14	0.10	0.32	0.39

Table 8.2: Pearson correlation coefficients for correlations between ratios of global signal measures and the covariates of interest in this study (age and gender). A positive correlation coefficient indicates the corresponding intensity ratio is higher in females.

8.4.2 Correlations with T1w and T2w global intensity measures

Correlations between the ratios of the three global intensity measures with age and gender for both T1w and T2w image sets are shown in Table 8.2.

8.4.2.1 Age and T1w/T2w global intensity measures

For the T1w global intensities, as age increases, both the VBIS and histogram peak measures increase relative to the whole brain mean (Table 8.2). For T2w we see a similarly strong correlation for the ratio of VBIS to whole brain mean, but with the opposite sign. The likely explanation for this pattern is the following: Older subjects have decreased brain tissue volume and larger ventricles and hence a larger proportion of CSF. As CSF is bright on T2w images and dark on T1w images, this leads to a spurious increase in the whole brain mean for T2w in older subjects and a spurious decrease in T1w whole brain mean. (Although these effects are partially compensated for by the spatial normalisation, some residual dependence is to be expected, due to partial volume effects and the extent of deformation being limited by the regularisation built into the spatial normalisation algorithm.)

As the VBIS region tends to lie well inside the borders of the brain parenchyma, the VBIS technique is expected to be immune to these spurious effects associated with morphological changes occurring with age. In contrast, the whole brain mean is the most susceptible to such effects because it is likely to include a relatively large amount of CSF. For T1w, peak normalisation appears to be unbiased but for T2w, the appears to be the middle ground between VBIS mean and whole brain mean.

The age dependence in the ratios of global intensity values likely accounts for much of the discrepancy between VBSA results obtained with different intensity normalisations. For the T2w comparisons with age, the spurious correlation between the whole brain mean and ages would bias the results towards showing an artificial decrease in T2w with age especially for the whole brain mean and to a lesser extent for the histogram peak results. The more modest but still highly significant decreases seen with VBIS normalisation are likely to be the more realistic representation of the statistical significance of the observed changes. The VBIS

result is also more balanced showing areas of significant increases in T2w with age as well as decreases. Similarly, for T1w, the whole brain mean result is likely biased towards showing an increase in T1w signal with age and should, therefore, be interpreted with caution.

8.4.2.2 Gender and T1w/T2w globals

For the T1w gender correlations, there is no signifcant difference between the correlations of gender with VBIS and with histogram peak global intensity measures, however the whole brain mean differs from the other two normalisations in its relationship to gender.

For T2w it is the peak intensity global normalisation factors that show a different relationship with gender than the other two intensity measures. The T2w histogram peak intensity in Females is approximately 3% high relative to the other two global intensity measures. The reason for this difference is unclear, but may be that there are different concentrations of iron between genders. as one would expected this to skew the whole brain mean and VBIS mean values more than the histogram peak.

For gender, the VBIS mean seems to give the most balanced results between positive and negative results and therefore appears to more fully adjust for global intensity differences-between the two genders.

8.4.3 Relationship of VBM globals with gender and age covariates

Significant correlations between total WMV and total GMV were present as shown in Table 8.3.

	TIV	TWMV	TGMV	TCSFV
age	-0.18	-0.17	-0.72	0.70
gender	-0.60	-0.52	-0.38	-0.24

Table 8.3: Pearson correlations of VBM global measures with age and gender. The minus sign for gender indicates decreased volume in females compared to males. Abbreviations: TIV Total Intercranial Volume; TWMV Total White Matter Volume; TGMV Total Gray Matter Volume; TCSFV Total Cerebro-Spinal Fluid Volume.

As discussed in Subsection 5.5.5, when there is a high correlation between the covariate of interest (CoI) (in this case age or gender) and the vector of ANCOVA globals, the regression is effectively being carried out with respect to the component of the CoI that is orthogonal to the vector of global values. Given the large correlation, the orthoginal component of the CoI may differ considerably from the original CoI, thus increasing the risk of obtaining artefactual results. (Peelle et al. 2012) looked at the differences in VBM results for voxelwise correlations

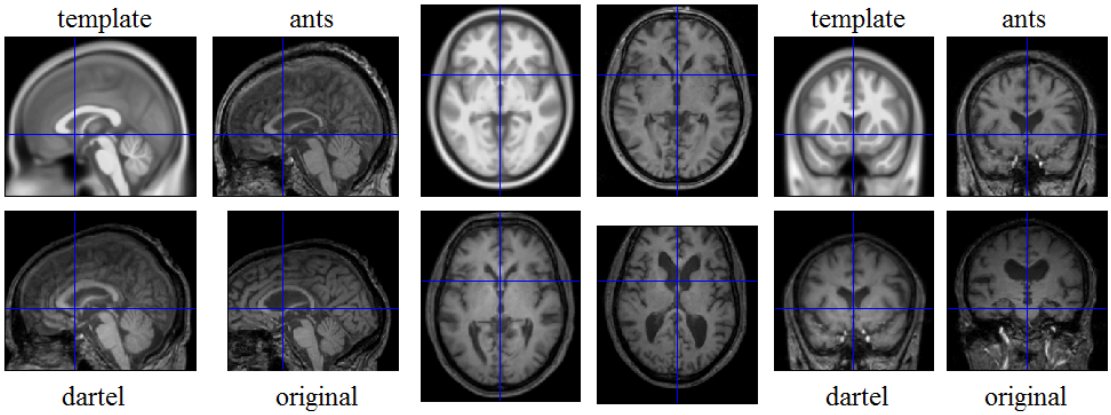

Figure 8.1: Comparison of spatial normalisation algorithms for subject 175, a challenging subject to achieve good normalisation due to significant atrophy and expansion in the ventricles. Top left: template image, bottom left: image after DARTEL normalisation, top right: image after SyN normalisation, bottom right: original image.

between GMV and age, obtained using ANCOVA and proportional scaling, finding that the overall patterns of change were similar for both methods.

8.5 Spatial Normalisation

The superior performance of DARTEL over ANTS' SyN algorithm is somewhat surprising given that (Klein et al. 2009) ranked ANTs higher than DARTEL. The difference in normalisation performance is likely due to the use of raw T1w images for the ANTS normalisation in this work rather than segmented images that were used for ANTS in (Klein et al. 2009). This suggests that the use of segmented images is preferable to using the raw T1w images in obtaining spatial normalisation maps.

For subjects with a large degree of brain atrophy, both normalisation algorithms struggled to fully compensate for the enlarged ventricles and cortical atrophy. Fig. 8.1 shows an example of a subject with severe atrophy and greatly enlarged ventricles. For this subject, the DARTEL segmentation based spatial normalisation is seen to perform better in matching the corpus callosum to the template (Fig. 8.1).

Chapter 9

Conclusion and Future Work

This work has demonstrated that voxel based statistical analysis of T1w and T2w images can be used to identify age related changes and gender differences in normal brains.

In assessing age related changes, the VBIS intensity normalisation yielded similar results to the histogram-based intensity normalisation, while the whole brain mean intensity normalisation sometimes gave quite different results. The histogram and VBIS methods provided a more reliable intensity normalisation because they did not exhibit the susceptibility to bias of the whole brain mean intensity normalisation.

The good agreement between VBIS mean and histogram peak scaling suggests that a hybrid of the two methods - taking the histogram peak location in the VBIS region instead of the mean may be the most optimal intensity normalisation strategy for minimising bias.

The use of segmented MR brain images to guide spatial normalisation was found to give superior results to the use of raw T1 weighted images.

The most statistically significant and striking result revealed in this study was a strong correlation between age and T2- weighted MR signal in the putamen, caudate head, amygdala and para-hippocampal gyrus, providing evidence of increasing iron content in these locations, most likely due to a higher rate of micro-bleeds in these regions. A logical next step would be to investigate T2w differences between healthy individuals and patients with neurological disorders involving the putamen such as Parkinson's disease and autism, with the goal of establishing T2w signal as a useful bio-marker. In such studies T2* weighted or susceptibility weighted images may be preferable for measuring iron related pathology and are equally amenable to the VBSA methods presented here. Higher resolution studies focusing on subcortical areas of interest would be useful in further elucidating the specific nuclei where iron accumulation is occurring. Sub-millimetre resolution T2* contrast "optimised 3D fast spin echo sequences" (Mugler 2014) such as Siemens "T2 SPACE',' offer such a possibility. Comparison with simultaneous PET and MR spectroscopy imaging may lead

to an improved understanding the complex neurophysiological interactions between neurotransmitter levels, iron content, metabolism and inflammation.

Longitudinal data would be useful to confirm that T2w changes are occurring in individual subjects and are not due to date specific environmental effects, and to explore how changes in T2w may be related to changes in symptoms and cognitive performance. Longitudinal studies may also be able to establish a prognostic value for MR imaging allowing targeted preventative measures to be deployed for individuals at high risk of vascular dementia.

In addition to the 152 subjects scanned with a 3T scanner studied here, the IXI dataset also includes more than 200 normal subjects scanned on 1.5T scanners. Analysis of this additional data would show how dependent the results are on the scanners ambient magnetic field strength. It is expected that scanners with higher field strengths are more sensitive to the effects of iron.

Other age related results revealed by this study include increasing T2w signal and decreasing T1w signal together with decreasing white matter volume with increasing age in the thalamus, and decreased T2w signal with increasing age in the anterior cingulate. The voxel based morphometry analysis performed here has given support to previous study showing preserved gray matter in the hippocampi, amygdala and para-hippocampal gyri.

Gender differences found with VBIS and peak normalisations include increased T1w signal in females in the putamen. Increased T1w signal in males was detected in the midbrain and increased T2w signal in the brainstem and medulla. All three intensity normalisations revealed increased T2w signal in Females in the superior longitudinal fasciculus.

Appendix A

More on the Physics of MR

A.1 Evolution under a fixed external magnetic field

If we for the moment neglect the time dependent B_1 term, the Schrodinger equation

$$i\hbar\frac{d}{dt}\psi_0(t) = \hat{H}_0\psi_0(t) \tag{A.1}$$

has solution

$$\psi_0(t) = \exp\left(i\gamma B_0 \cdot \frac{\sigma}{2}t\right)\psi_0(0). \tag{A.2}$$

The time evolution operator is therefore $U_0(t) = \exp\left(i\gamma B_0 \cdot \frac{\sigma}{2}t\right)$. The density matrix evolves according to $\rho_0(t) = U_0(t)\rho(0)U_0^\dagger(t)$ and satisfies the Heisenberg equation

$$i\hbar\frac{d\rho_0}{dt} = [\rho_0, H_0]. \tag{A.3}$$

Choosing a reference frame such that the background magnetic field B_0 is aligned along the z-axis, we have $U_0(t) = \exp\left(i\omega_0\frac{\sigma_3}{2}t\right)$ and

$$\rho_0(t) = U_0(t)\rho_0(0)U_0^\dagger(t) = \begin{pmatrix} \rho_0^{\uparrow\uparrow}(0) & e^{i\omega_0 t/\hbar}\rho_0^{\uparrow\downarrow}(0) \\ e^{-i\omega_0 t/\hbar}\rho_0^{\downarrow\uparrow}(0) & \rho_0^{\downarrow\downarrow}(0) \end{pmatrix} \tag{A.4}$$

Note that only the off-diagonal elements show a time dependence.

A.2 Interaction with Electro Magnetic Radiation

We now want to study the dynamics of the nuclei under an external radio frequency (RF) electromagnetic field. RF radiation propagates parallel to the B_0 field, inducing an oscillating

magnetic field

$$B_1(t) = |B_1|(\cos(\omega_{RF}t), \sin(\omega_{RF}t), 0) \tag{A.5}$$

The RF component of the Hamiltonian in the pauli matrix basis is therefore

$$H_1(t) = \frac{\hbar\omega_1}{2}\begin{pmatrix} 0 & \exp(-i\omega_{RF}t) \\ \exp(+i\omega_{RF}t) & 0 \end{pmatrix} \tag{A.6}$$

with $\omega_1 = \gamma|B_1|$. We now transform all operators to a frame of reference rotating about the z axis with frequency ω and use the tilde symbol ($\widetilde{}$) to denote an operator transformed to this frame

$$\widetilde{\mathcal{O}}(t) = \exp\left(\, i\omega t\frac{\sigma_3}{2}\right)\mathcal{O}(t)\exp\left(-i\omega t\frac{\sigma_3}{2}\right) \tag{A.7}$$

In terms of these variables, the Heisenberg equation becomes

$$i\hbar\frac{d\tilde{\rho}}{dt} = [\tilde{\rho},\, \widetilde{H}^{(\omega)}_{\text{Eff}}]. \tag{A.8}$$

with the effective hamiltonian

$$\widetilde{H}^{(\omega)}_{\text{Eff}} = \widetilde{H} - \hbar\omega\frac{\sigma_3}{2} = \widetilde{H}_1 + \hbar(\omega_0 - \omega)\frac{\sigma_3}{2} \tag{A.9}$$

For a frame rotating with frequency ω, the effective hamiltonian is[22]

$$\widetilde{H}^{(\omega)}_{\text{Eff}}(t) = \frac{1}{2}\begin{pmatrix} \hbar(\omega_0 - \omega) & \hbar\omega_1\exp(-i(\omega_{RF} - \omega)\,t) \\ \hbar\omega_1\exp(+i(\omega_{RF} - \omega)\,t) & -\hbar(\omega_0 - \omega) \end{pmatrix} \tag{A.13}$$

[22]To obtain this result, apply the Baker-Campbell-Haussdorf formula to get

$$\widetilde{H}_1(t) = \exp\left(i\omega_0\frac{\sigma_3}{2}t\right)H_1(t)\exp\left(-i\omega_0\frac{\sigma_3}{2}t\right) = \exp\left(i\omega_0 t\hat{\imath}_3\right)(H_1(t)) \tag{A.10}$$

with $\hat{\imath}_i(X) := [\frac{\sigma_i}{2}, X]$. Now note that

$$\hat{\imath}_3\begin{pmatrix} 0 & z \\ z^* & 0 \end{pmatrix} = \begin{pmatrix} 0 & z \\ -z^* & 0 \end{pmatrix}. \tag{A.11}$$

It follows that $\hat{\imath}_3^j H_1 = \hat{\imath}_3^{j+2}H_1$. Therefore

$$\begin{aligned}\widetilde{H}_1(t) &= \frac{\gamma|B_1|}{2}\left[\cos(\omega_0 t)\begin{pmatrix} 0 & \exp(-i\omega_{RF}t) \\ \exp(+i\omega_{RF}t) & 0 \end{pmatrix} + i\sin(\omega_0 t)\begin{pmatrix} 0 & \exp(-i\omega_{RF}t) \\ -\exp(+i\omega_{RF}t) & 0 \end{pmatrix}\right] \\ &= \frac{\gamma|B_1|}{2}\begin{pmatrix} 0 & \exp(-i(\omega_{RF} - \omega_0)t) \\ \exp(+i(\omega_{RF} - \omega_0)t) & 0 \end{pmatrix}\end{aligned} \tag{A.12}$$

Setting $\omega = \omega_{RF}$, we can remove the explicit time dependence from $\widetilde{H}_1$ to obtain.

$$\widetilde{H}_{\text{Eff}}^{(\omega_{\text{RF}})}(t) = \frac{\hbar}{2}\begin{pmatrix} \Delta & \omega_1 \\ \omega_1 & -\Delta \end{pmatrix} = \hbar\,\omega_1\frac{\sigma_1}{2} + \hbar\,\Delta\frac{\sigma_3}{2} \tag{A.14}$$

with $\Delta = \omega_0 - \omega_{RF}$. Having removed the time dependence from the effective Hamiltonian, the evolution operator in the rotating frame is then simply

$$\widetilde{U}(t) = \exp\left(\frac{i}{\hbar}\widetilde{H}_{\text{Eff}}^{(\omega_{\text{RF}})}t\right) \tag{A.15}$$

and the evolution of the density matrix (in the original non rotating frame) is

$$\rho(t) = \exp\left(-i\omega_{\text{RF}}t\frac{\sigma_3}{2}\right)\exp\left(\frac{i}{\hbar}\widetilde{H}_{\text{Eff}}^{(\omega_{\text{RF}})}t\right)\rho(0)\exp\left(-\frac{i}{\hbar}\widetilde{H}_{\text{Eff}}^{(\omega_{\text{RF}})}t\right)\exp\left(+i\omega_{\text{RF}}t\frac{\sigma_3}{2}\right) \tag{A.16}$$

While this formula may appear complicated, it has a simple geometric interpretation. The time evolution of the density matrix vector $\vec{\rho}$ is given by a rotation of the Bloch sphere about the vector $(\omega_1, 0, \Delta)$ by an angle of $\sqrt{\omega_1^2 + \Delta^2} \times t$ radians followed by a rotation about the z-axis $(0, 0, 1)$ by an angle of $\omega_{\text{RF}} \times t$ radians. In the on resonance case $\Delta = 0$, with ρ initially in its equilibrium position pointing along the z axis ($\vec{\rho}(0) = (0, 0, \rho_3(0))$, the result reduces to

$$\rho = \frac{1}{2}\mathbb{I} + \frac{1}{2}\Big[\cos(\omega_1 t)\sigma_3 + \sin(\omega_1 t)\big(\cos(\omega_0 t)\sigma_2 + \sin(\omega_0 t)\sigma_1\big)\Big]\rho_3(0). \tag{A.17}$$

From this formula, we see that for an RF pulse of duration $t_{90} = \frac{\pi}{2\omega_1}$, the magnetization vector will be completely transferred into the transverse plane. This is called a 90° pulse as it induces a change in the magnetization vector by an angle of 90°. Similarly, a 180° pulse of duration $t_{180} = \frac{\pi}{\omega_1}$ completely inverts the magnetization vector.

A.3 Derivation of the Bloch equations

The magnetization vector is given in terms of the density matrix by $M^i = \gamma \mathrm{Tr}[\frac{\sigma^i}{2}\rho]$. The time evolution is therefore

$$\begin{aligned}\frac{d}{dt}M^i = \gamma \mathrm{Tr}\left[\frac{\sigma^i}{2}\frac{d\rho}{dt}\right] &= \frac{\gamma}{(i\hbar)}\mathrm{Tr}\left[\frac{\sigma^i}{2}[\rho, H]\right] + \gamma \mathrm{Tr}\left[\frac{\sigma^i}{2}R(\rho)\right] \\ &= \frac{\hbar\gamma^2}{8(i\hbar)}\left(\sum_{j,k}\rho_j B_k \mathrm{Tr}\left[\sigma^i, [\sigma^j, \sigma^k]\right]\right) + \gamma\sum_j \lambda_j(\rho_j - \rho_j^{\mathrm{eq}})\mathrm{Tr}\left[\frac{\sigma^i}{2}\,\frac{\sigma^j}{2}\right]\end{aligned} \tag{A.18}$$

Using the identities $\mathrm{Tr}[\sigma^i\sigma^j] = 2\delta^{ij}$ and $[\sigma^j, \sigma^k] = 2i\epsilon^{ijk}\sigma_i$, we obtain the Bloch equations

$$\frac{dM_i}{dt} = \gamma\sum_{j,k}\varepsilon_{ijk}M^j B^k + \lambda_i(M_i - M_i^{\mathrm{eq}}) \tag{A.19}$$

which are fundamental to MRI.

The solution to the Bloch equations then works out to be

$$M_x(t) = M_\perp(0)\exp(-R_2 t)\cos(\omega_0 t + \theta) \tag{A.20}$$

$$M_y(t) = M_\perp(0)\exp(-R_2 t)\sin(\omega_0 t + \theta) \tag{A.21}$$

$$M_z(t) = (M_z(0) - M_z^{\mathrm{eq}})\exp(-R_1 t) + M_z^{\mathrm{eq}} \tag{A.22}$$

where θ, $M_z(0)$ and $M_\perp(0)$ are determined by the initial state of the system. As previously, $\omega_0 = \gamma|B_0|$ is the Larmor frequency.

Bibliography

Abbott, D. F., Pell, G. S., Pardoe, H. & Jackson, G. D. (2009), 'Voxel-based iterative sensitivity (vbis) analysis: methods and a validation of intensity scaling for t2-weighted imaging of hippocampal sclerosis', *Neuroimage* **44**(3), 812–819.

Aquino, D., Bizzi, A., Grisoli, M., Garavaglia, B., Bruzzone, M. G., Nardocci, N., Savoiardo, M. & Chiapparini, L. (2009), 'Age-related iron deposition in the basal ganglia: Quantitative analysis in healthy subjects 1', *Radiology* **252**(1), 165–172.

Ashburner, J. (2007), 'A fast diffeomorphic image registration algorithm', *Neuroimage* **38**(1), 95–113.

Ashburner, J. & Friston, K. J. (2005), 'Unified segmentation', *Neuroimage* **26**(3), 839–851.

Aubert-Broche, B., Fonov, V., Leppert, I., Pike, G. B. & Collins, D. L. (2008), Human brain myelination from birth to 4.5 years, *in* 'International Conference on Medical Image Computing and Computer-Assisted Intervention', Springer, pp. 180–187.

Avants, B. B., Epstein, C. L., Grossman, M. & Gee, J. C. (2008), 'Symmetric diffeomorphic image registration with cross-correlation: evaluating automated labeling of elderly and neurodegenerative brain', *Medical image analysis* **12**(1), 26–41.

Baas, D., Aleman, A. & Kahn, R. S. (2004), 'Lateralization of amygdala activation: a systematic review of functional neuroimaging studies', *Brain Research Reviews* **45**(2), 96–103.

Barnden, L., Kwiatek, R., Badger, D. & Mernone, A. (2008), 'Histogram-based global scaling of t1-and t2-weighted brain mr for voxel-based quantification', *Australasian Physical & Engineering Sciences in Medicine* **31**(4), 394.

Barnden, L. R. & Behin-Ain, S. (2004), Data based optimization of brain spect processing for voxel-based statistical analysis, *in* 'Nuclear Science Symposium Conference Record, 2004 IEEE', Vol. 6, IEEE, pp. 3708–3711.

Barnden, L. R., Crouch, B., Kwiatek, R., Burnet, R. & Del Fante, P. (2015), 'Evidence in chronic fatigue syndrome for severity-dependent upregulation of prefrontal myelination that is independent of anxiety and depression', *NMR in Biomedicine* **28**(3), 404–413.

Barnden, L. R., Crouch, B., Kwiatek, R., Burnet, R., Mernone, A., Chryssidis, S., Scroop, G. & Del Fante, P. (2011), 'A brain mri study of chronic fatigue syndrome: evidence of brainstem dysfunction and altered homeostasis', *NMR in Biomedicine* **24**(10), 1302–1312.

Barnden, L. R., Kwiatek, R., Crouch, B., Burnet, R. & Del Fante, P. (2016), 'Autonomic correlations with mri are abnormal in the brainstem vasomotor centre in chronic fatigue syndrome', *NeuroImage: Clinical* .

Bloembergen, N., Purcell, E. M. & Pound, R. V. (1948), 'Relaxation effects in nuclear magnetic resonance absorption', *Physical review* **73**(7), 679.

Brass, S. D., Chen, N.-k., Mulkern, R. V. & Bakshi, R. (2006), 'Magnetic resonance imaging of iron deposition in neurological disorders', *Topics in Magnetic Resonance Imaging* **17**(1), 31–40.

Bullmore, E. T., Suckling, J., Overmeyer, S., Rabe-Hesketh, S., Taylor, E. & Brammer, M. J. (1999), 'Global, voxel, and cluster tests, by theory and permutation, for a difference between two groups of structural mr images of the brain', *IEEE transactions on medical imaging* **18**(1), 32–42.

Burgetova, A., Seidl, Z., Krasensky, J., Horakova, D. & Vaneckova, M. (2010), 'Multiple sclerosis and the accumulation of iron in the basal ganglia: quantitative assessment of brain iron using mri t2 relaxometry', *European neurology* **63**(3), 136–143.

Cahill, L., Uncapher, M., Kilpatrick, L., Alkire, M. T. & Turner, J. (2004), 'Sex-related hemispheric lateralization of amygdala function in emotionally influenced memory: an fmri investigation', *Learning & Memory* **11**(3), 261–266.

Callaghan, M. F., Helms, G., Lutti, A., Mohammadi, S. & Weiskopf, N. (2015), 'A general linear relaxometry model of r1 using imaging data', *Magnetic Resonance in Medicine* **73**(3), 1309–1314.

Cao, J., Worsley, K. J. et al. (1999), 'The detection of local shape changes via the geometry of hotelling's t^2 fields', *The Annals of Statistics* **27**(3), 925–942.

Cass, W. A., Grondin, R., Andersen, A. H., Zhang, Z., Hardy, P. A., Hussey-Andersen, L. K., Rayens, W. S., Gerhardt, G. A. & Gash, D. M. (2007), 'Iron accumulation in the striatum predicts aging-related decline in motor function in rhesus monkeys', *Neurobiology of aging* **28**(2), 258–271.

Connor, J., Menzies, S., St Martin, S. & Mufson, E. (1990), 'Cellular distribution of transferrin, ferritin, and iron in normal and aged human brains', *Journal of neuroscience research* **27**(4), 595–611.

Connor, J. R. (2013), *Metals and oxidative damage in neurological disorders*, Springer Science & Business Media.

Connor, J., Snyder, B., Beard, J., Fine, R. & Mufson, E. (1992), 'Regional distribution of iron and iron-regulatory proteins in the brain in aging and alzheimer's disease', *Journal of neuroscience research* **31**(2), 327–335.

Cosgrove, K. P., Mazure, C. M. & Staley, J. K. (2007), 'Evolving knowledge of sex differences in brain structure, function, and chemistry', *Biological psychiatry* **62**(8), 847–855.

Cox, R. W., Ashburner, J., Breman, H., Fissell, K., Haselgrove, C., Holmes, C. J., Lancaster, J. L., Rex, D. E., Smith, S. M., Woodward, J. B. et al. (2004), 'A (sort of) new image data format standard: Nifti-1', *Human Brain Mapping* **25**, 33.

Craggs, L. J., Yamamoto, Y., Deramecourt, V. & Kalaria, R. N. (2014), 'Microvascular pathology and morphometrics of sporadic and hereditary small vessel diseases of the brain', *Brain Pathology* **24**(5), 495–509.

Cui, X., Li, J. & Song, X. (2016), 'xjview: a viewing program for spm', *Retreived from www.alivelearn.net/xjview* .

Daugherty, A. M. & Raz, N. (2015), 'Appraising the role of iron in brain aging and cognition: promises and limitations of mri methods', *Neuropsychology Review* **25**(3), 272–287.

Dini, L. I., Vedolin, L. M., Bertholdo, D., Grando, R. D., Mazzola, A., Dini, S. A., Isolan, G. R., da Costa, J. C. & Campero, A. (2013), 'Reproducibility of quantitative fiber tracking measurements in diffusion tensor imaging of frontal lobe tracts: A protocol based on the fiber dissection technique', *Surgical neurology international* **4**.

Drayer, B. P. (1988), 'Imaging of the aging brain. part i. normal findings.', *Radiology* **166**(3), 785–796.

Franceschi, C., Bonafè, M., Valensin, S., Olivieri, F., De Luca, M., Ottaviani, E. & De Benedictis, G. (2000), 'Inflamm-aging: an evolutionary perspective on immunosenescence', *Annals of the New York Academy of Sciences* **908**(1), 244–254.

Friston, K. J. (1994), 'Statistical parametric mapping.'.

Friston, K. J., Ashburner, J., Heather, J. et al. (2003), 'Statistical parametric mapping', *Neuroscience databases: a practical guide* **16**, 237–250.

Friston, K. J., Worsley, K. J., Frackowiak, R., Mazziotta, J. C. & Evans, A. C. (1994), 'Assessing the significance of focal activations using their spatial extent', *Human brain mapping* **1**(3), 210–220.

Ganzetti, M., Wenderoth, N. & Mantini, D. (2014), 'Whole brain myelin mapping using t1-and t2-weighted mr imaging data', *Frontiers in human neuroscience* **8**.

Gaser, C. & Dahnke, R. (2012), 'Cat a computational anatomy toolbox for spm'.

Ghadery, C., Pirpamer, L., Hofer, E., Langkammer, C., Petrovic, K., Loitfelder, M., Schwingenschuh, P., Seiler, S., Duering, M., Jouvent, E. et al. (2015), 'R2* mapping for brain iron: associations with cognition in normal aging', *Neurobiology of aging* **36**(2), 925–932.

Ghisleni, C., Bollmann, S., Biason-Lauber, A., Poil, S.-S., Brandeis, D., Martin, E., Michels, L., Hersberger, M., Suckling, J., Klaver, P. et al. (2015), 'Effects of steroid hormones on sex differences in cerebral perfusion', *PloS one* **10**(9), e0135827.

Gigandet, X., Hagmann, P., Kurant, M., Cammoun, L., Meuli, R. & Thiran, J.-P. (2008), 'Estimating the confidence level of white matter connections obtained with mri tractography', *PLoS One* **3**(12), e4006.

Goldman, M. (2001), 'Formal theory of spin–lattice relaxation', *Journal of Magnetic Resonance* **149**(2), 160–187.

Good, C. D., Johnsrude, I., Ashburner, J., Henson, R. N., Friston, K. J. & Frackowiak, R. S. (2001), 'Cerebral asymmetry and the effects of sex and handedness on brain structure: a voxel-based morphometric analysis of 465 normal adult human brains', *Neuroimage* **14**(3), 685–700.

Good, C. D., Johnsrude, I. S., Ashburner, J., Henson, R. N., Fristen, K. & Frackowiak, R. S. (2002), A voxel-based morphometric study of ageing in 465 normal adult human brains, *in* 'Biomedical Imaging, 2002. 5th IEEE EMBS International Summer School on', IEEE, pp. 16–pp.

Goto, M., Abe, O., Miyati, T., Aoki, S., Takao, H., Hayashi, N., Mori, H., Kunimatsu, A., Ino, K., Yano, K. et al. (2013), 'Association between iron content and gray matter missegmentation with voxel-based morphometry in basal ganglia', *Journal of Magnetic Resonance Imaging* **38**(4), 958–962.

Gray, H. (1918), *Anatomy of the human body*, Lea & Febiger.

Haacke, E. M., Miao, Y., Liu, M., Habib, C. A., Katkuri, Y., Liu, T., Yang, Z., Lang, Z., Hu, J. & Wu, J. (2010), 'Correlation of putative iron content as represented by changes in r2* and phase with age in deep gray matter of healthy adults', *Journal of Magnetic Resonance Imaging* **32**(3), 561–576.

Hallgren, B. & Sourander, P. (1958), 'The effect of age on the non-haemin iron in the human brain', *Journal of neurochemistry* **3**(1), 41–51.

Hargreaves, B. (2012), 'Rapid gradient-echo imaging', *Journal of Magnetic Resonance Imaging* **36**(6), 1300–1313.

Hayasaka, S., Phan, K. L., Liberzon, I., Worsley, K. J. & Nichols, T. E. (2004), 'Nonstationary cluster-size inference with random field and permutation methods', *Neuroimage* **22**(2), 676–687.

Hubel, D. H. & Wiesel, T. N. (1974), 'Sequence regularity and geometry of orientation columns in the monkey striate cortex', *Journal of Comparative Neurology* **158**(3), 267–293.

Janaway, B., Simpson, J., Hoggard, N., Highley, J., Forster, G., Drew, D., Gebril, O., Matthews, F., Brayne, C., Wharton, S. et al. (2014), 'Brain haemosiderin in older people: pathological evidence for an ischaemic origin of magnetic resonance imaging (mri) microbleeds', *Neuropathology and applied neurobiology* **40**(3), 258–269.

Klein, A., Andersson, J., Ardekani, B. A., Ashburner, J., Avants, B., Chiang, M.-C., Christensen, G. E., Collins, D. L., Gee, J., Hellier, P. et al. (2009), 'Evaluation of 14 nonlinear deformation algorithms applied to human brain mri registration', *Neuroimage* **46**(3), 786–802.

Koenig, S., Brown, R., Spiller, M. & Lundbom, N. (1990), 'Relaxometry of brain: why white matter appears bright in mri', *Magnetic resonance in medicine* **14**(3), 482–495.

Koenig, S. H. (1991), 'Cholesterol of myelin is the determinant of gray-white contrast in mri of brain', *Magnetic resonance in medicine* **20**(2), 285–291.

Koenig, S. H. (1995), 'Classes of hydration sites at protein-water interfaces: the source of contrast in magnetic resonance imaging.', *Biophysical journal* **69**(2), 593.

Lambert, C., Chowdhury, R., FitzGerald, T. H., Fleming, S. M., Lutti, A., Hutton, C., Draganski, B., Frackowiak, R. & Ashburner, J. (2013), 'Characterizing aging in the human brainstem using quantitative multimodal mri analysis', *Frontiers in human neuroscience* **7**.

Lancaster, J. L., Tordesillas-Gutiérrez, D., Martinez, M., Salinas, F., Evans, A., Zilles, K., Mazziotta, J. C. & Fox, P. T. (2007), 'Bias between mni and talairach coordinates analyzed using the icbm-152 brain template', *Human brain mapping* **28**(11), 1194–1205.

Lancaster, J. L., Woldorff, M. G., Parsons, L. M., Liotti, M., Freitas, C. S., Rainey, L., Kochunov, P. V., Nickerson, D., Mikiten, S. A. & Fox, P. T. (2000), 'Automated talairach atlas labels for functional brain mapping', *Human brain mapping* **10**(3), 120–131.

Moos, T. (2002), 'Brain iron homeostasis.', *Danish medical bulletin* **49**(4), 279–301.

Mori, S., Wakana, S., Van Zijl, P. C. & Nagae-Poetscher, L. (2005), *MRI atlas of human white matter*, Vol. 16, Am Soc Neuroradiology.

Mugler, J. P. (2014), 'Optimized three-dimensional fast-spin-echo mri', *Journal of Magnetic Resonance Imaging* **39**(4), 745–767.

Pakkenberg, B., Pelvig, D., Marner, L., Bundgaard, M. J., Gundersen, H. J. G., Nyengaard, J. R. & Regeur, L. (2003), 'Aging and the human neocortex', *Experimental gerontology* **38**(1), 95–99.

Peelle, J. E., Cusack, R. & Henson, R. N. (2012), 'Adjusting for global effects in voxel-based morphometry: gray matter decline in normal aging', *Neuroimage* **60**(2), 1503–1516.

Pell, G. S., Briellmann, R. S., Waites, A. B., Abbott, D. F. & Jackson, G. D. (2004), 'Voxel-based relaxometry: a new approach for analysis of t2 relaxometry changes in epilepsy', *Neuroimage* **21**(2), 707–713.

Priebe, N. J., Lisberger, S. G. & Movshon, J. A. (2006), 'Tuning for spatiotemporal frequency and speed in directionally selective neurons of macaque striate cortex', *The Journal of Neuroscience* **26**(11), 2941–2950.

Raz, N., Rodrigue, K. M., Kennedy, K. M., Head, D., Gunning-Dixon, F. & Acker, J. D. (2003), 'Differential aging of the human striatum: longitudinal evidence', *American Journal of Neuroradiology* **24**(9), 1849–1856.

Salgado, J. C., Olivera-Nappa, A., Gerdtzen, Z. P., Tapia, V., Theil, E. C., Conca, C. & Nuñez, M. T. (2010), 'Mathematical modeling of the dynamic storage of iron in ferritin', *BMC systems biology* **4**(1), 147.

Sato, W., Kubota, Y., Kochiyama, T., Uono, S., Yoshimura, S., Sawada, R., Sakihama, M. & Toichi, M. (2013), 'Increased putamen volume in adults with autism spectrum disorder.', *Frontiers in human neuroscience* **8**, 957–957.

Schenck, J. F. (2003), 'Magnetic resonance imaging of brain iron', *Journal of the neurological sciences* **207**(1), 99–102.

Shapley, R. & Lennie, P. (1985), 'Spatial frequency analysis in the visual system', *Annual review of neuroscience* **8**(1), 547–581.

Shihabuddin, L., Buchsbaum, M. S., Hazlett, E. A., Silverman, J., New, A., Brickman, A. M., Mitropoulou, V., Nunn, M., Fleischman, M. B., Tang, C. et al. (2001), 'Striatal size and relative glucose metabolic rate in schizotypal personality disorder and schizophrenia', *Archives of General Psychiatry* **58**(9), 877–884.

Smith, E. E., Schneider, J. A., Wardlaw, J. M. & Greenberg, S. M. (2012), 'Cerebral microinfarcts: the invisible lesions', *The Lancet Neurology* **11**(3), 272–282.

Smith, S. M. & Nichols, T. E. (2009), 'Threshold-free cluster enhancement: addressing problems of smoothing, threshold dependence and localisation in cluster inference', *Neuroimage* **44**(1), 83–98.

Smythies, J. (1999), 'The neurotoxicity of glutamate, dopamine, iron and reactive oxygen species: functional interrelationships in health and disease: a reviewdiscussion', *Neurotoxicity research* **1**(1), 27–39.

Steiger, T. K., Weiskopf, N. & Bunzeck, N. (2016), 'Iron level and myelin content in the ventral striatum predict memory performance in the aging brain', *Journal of Neuroscience* **36**(12), 3552–3558.

Studholme, C., Hill, D. L. & Hawkes, D. J. (1999), 'An overlap invariant entropy measure of 3d medical image alignment', *Pattern recognition* **32**(1), 71–86.

Stueber, C., Morawski, M., Schäfer, A., Labadie, C., Wähnert, M., Leuze, C., Streicher, M., Barapatre, N., Reimann, K., Geyer, S. et al. (2014), 'Myelin and iron concentration in the human brain: a quantitative study of mri contrast', *Neuroimage* **93**, 95–106.

Talairach, J. & Tournoux, P. (1988), 'Co-planar stereotaxic atlas of the human brain. 3-dimensional proportional system: an approach to cerebral imaging'.

The McConnell Brain Imaging Centre (2009), 'Icbm 152 nonlinear atlases version 2009'.

Tofts, P. (2005), *Quantitative MRI of the brain: measuring changes caused by disease*, John Wiley & Sons.

Tofts, P. & Du Boulay, E. (1990), 'Towards quantitative measurements of relaxation times and other parameters in the brain', *Neuroradiology* **32**(5), 407–415.

Tustison, N. J., Avants, B. B., Cook, P. A., Kim, J., Whyte, J., Gee, J. C. & Stone, J. R. (2014), 'Logical circularity in voxel-based analysis: Normalization strategy may induce statistical bias', *Human brain mapping* **35**(3), 745–759.

Tzourio-Mazoyer, N., Landeau, B., Papathanassiou, D., Crivello, F., Etard, O., Delcroix, N., Mazoyer, B. & Joliot, M. (2002), 'Automated anatomical labeling of activations in spm using a macroscopic anatomical parcellation of the mni mri single-subject brain', *Neuroimage* **15**(1), 273–289.

Vymazal, J., Brooks, R. A., Baumgarner, C., Tran, V., Katz, D., Bulte, J. W., Bauminger, E. R. & Chiro, G. D. (1996), 'The relation between brain iron and nmr relaxation times: an in vitro study', *Magnetic resonance in medicine* **35**(1), 56–61.

Weickert, J. (1998), *Anisotropic diffusion in image processing*, Vol. 1, Teubner Stuttgart.

Weiskopf, N., Suckling, J., Williams, G., Correia, M. M., Inkster, B., Tait, R., Ooi, C., Bullmore, E. T. & Lutti, A. (2013), 'Quantitative multi-parameter mapping of r1, pd*, mt, and r2* at 3t: a multi-center validation', *Frontiers in neuroscience* **7**.

Worsley, K. J., Taylor, J. E., Tomaiuolo, F. & Lerch, J. (2004), 'Unified univariate and multivariate random field theory', *Neuroimage* **23**, S189–S195.

Yoder, N. (2011), 'Peakfinder'.

Zahr, N. M., Mayer, D., Rohlfing, T., Chanraud, S., Gu, M., Sullivan, E. V. & Pfefferbaum, A. (2013), 'In vivo glutamate measured with magnetic resonance spectroscopy: behavioral correlates in aging', *Neurobiology of aging* **34**(4), 1265–1276.